EBM Experimental Biology and Medicine

Volume 249 | Issue 7

Experimental Biology and Medicine

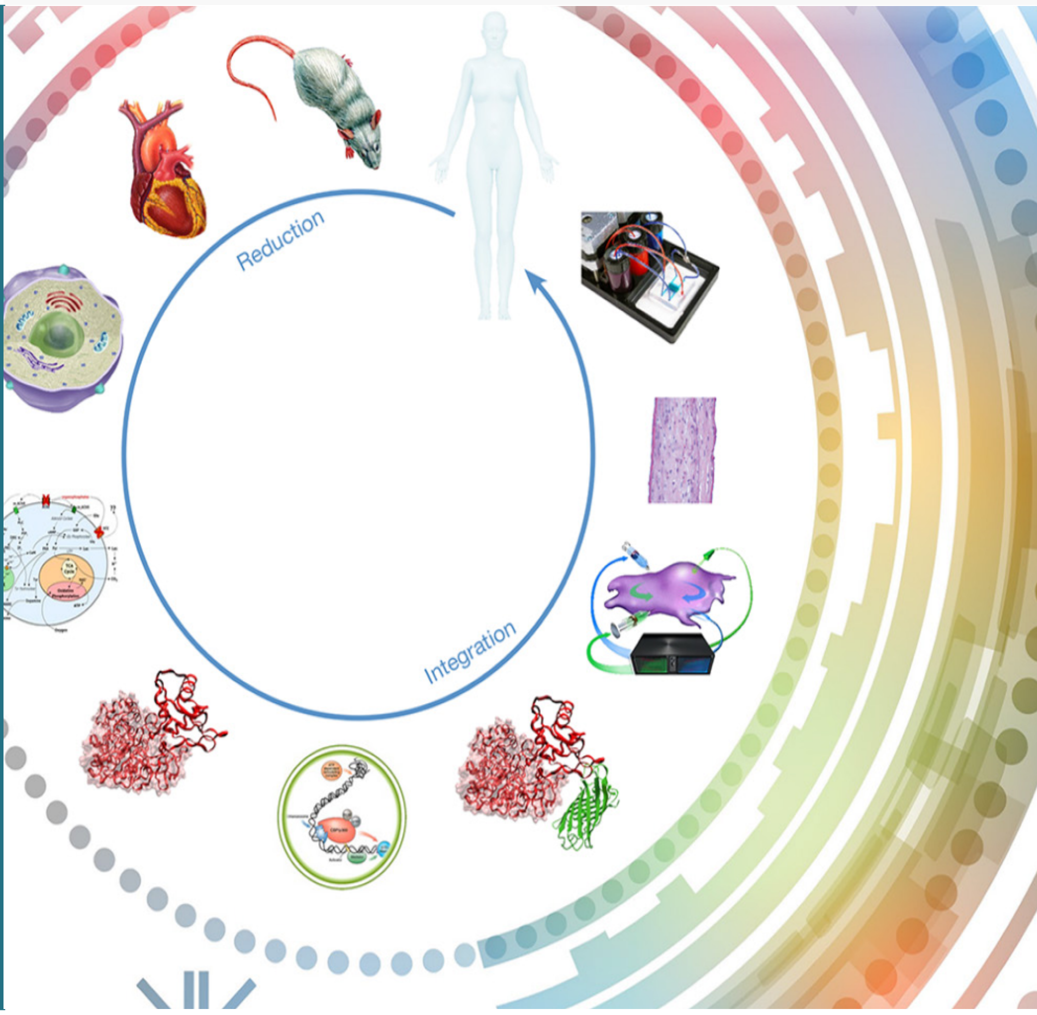

Interim Editor in Chief

Nicola Conran
University of Campinas,
Brazil

ISBN 978-2-8325-5879-9
DOI 10.3389/978-2-8325-5879-9

frontiers | Publishing Partnerships

SEBM Executive Council

Publication Committee

Society for Experimental Biology and Medicine
3220 N Street NW, #179
Washington DC 20007, USA
Executive Director – ed@sebm.org
Assistant to Editor-in-Chief – bzimmer@sebm.org

www.sebm.org

EBM Experimental Biology and Medicine

Editorial Board

INTERIM EDITOR IN CHIEF
Nicola Conran
University of Campinas

GLOBAL EDITORS

Africa
Gordon Awandare
University of Ghana

Asia
Shaw-Jenq Tsai
National Cheng Kung University

Europe
Farzin Farzaneh
King’s College London

Latin America
Nicola Conran
University of Campinas

Australia/Oceana
Sulev Kõks
Murdoch University

Anatomy/Pathology

Associate Editor

Ian Zagon
Penn State University College of Medicine

William Banks
Alexander V. Ljubimov
Patricia J. McLaughlin
Artur Pasternak

Artifical Intelligence/Machine Learning Applications to Biomedical Research

Associate Editor

Huixiao Hong
US Food and Drug Administration

Xiaohui Fan
Ping Gong
Ruili Huang
Jie Liu
Fred Prior
Paul Rogers
Tieliu Shi
Wei Shi
Wenming Xiao

Biochemistry and Molecular Biology

Associate Editor

Muriel A. Lambert
Rutgers New Jersey Medical School

Brian D Adams
Bin Guo
J. Patrick O’connor

Bioimaging

Associate Editor

Shuliang Jiao
Florida International University

Kamran Avanaki
Zygmunt Gryczynski
Xinmai Yang
Xincheng Yao
Baohong Yuan
Weizhao Zhao

Biomedical Engineering

Associate Editor

F. Kurtis Kasper
University of Texas Health Science Center at Houston

Angela Pannier

Bionanoscience

Associate Editor

Juan Melendez
University of Albany

Nathaniel Cady
Hassan A. Elfawal
Jonathan F Lovell
Ya-Ping Sun
Maria Tomassone
Siyang Zheng

Cell and Developmental Biology

David Dean
Leszek Kotula
Harold I Saavedra
Yigang Wang
Warren Zimmer

Clinical Trials

Giuseppe Pizzorno
Daniel Vaena

Endocrinology and Nutrition

Co Associate Editors

Clint Allred and Keith Erikson
University of North Carolina Greensboro

Demin Cai
Sam Dagogo-Jack
Weiqun Wang
Malcolm Watford
Chia-Shan Wu

Environmental Health/Biomarkers/Precision Medicine

Associate Editor

William Slikker, Jr.
Retired

Gary Steven Friedman
Donald Johann
Igor Pogribny

Genomics, Proteomics, and Bioinformatics

Associate Editor

Sulev Kõks
Murdoch University

Mark Geraci
Paul Potter
John P Quinn
Giovanni Stracquadanio

Immunology/Microbiolog/Virology

Associate Editor

Flávio Guimarães Da Fonseca
Federal University of Minas Gerais

Andrea Doria
Farzin Farzaneh
Kam Hui
Francois Villinger

Mechanisms of Aging

Associate Editor

Shigemi Matsuyama
Case Western Reserve University

Ricki Colman
Aolin Allen Hsu
Akihiro Ikeda
Masaru Miyagi
Vincent Monnier

Neuroscience

Associate Editor

Michael Neal Lehman
Kent State University

Lique M. Coolen
Terrence Deak
Max L Fletcher
Sandra Mooney
Gregg Stanwood
Richard M Xu

Pharmacology/Toxicology

Associate Editor

Santosh Kumar
University of Tennessee Health Science Center

Guzel Bikbova
Pawel Brzuzan
Laetitia Dou
Jianxiong Jiang
Youngmi Jung
Li-Fu Li
Jonathan Shannahan
Manish Tripathi
Chaowu Xiao
Wuxiang Xie
Qihe Xu

Physiology and Pathophysiology

Associate Editor

Robert T. Mallet
University of North Texas Health Science Center

Rong Ma
Gabor Tigyi
Shaw-Jenq Tsai
Samuel Verges
Lei Xi
Chunyu Zeng

Population Health

Associate Editor

Ashish Joshi
School of Public Health, University of Memphis

Stem Cell Biology

Associate Editor

Jian Feng
State University of New York at Buffalo

Vania Broccoli
Jose Cibelli
Guoping Fan
Antonis Hatzopoulos
Dan S. Kaufman
Chun-Li Zhang

Structural Biology

Associate Editor

Tom Thompson
University of Cincinnati

Andrew P. Hinck
James Horn
Rhett Kovall
Vincent Luca
Rick Page

Synthetic Biology

Tara Deans
Ahmad Khalil
Aditya M. Kunjapur
Kevin Solomon

Systems Biology and Microphysiological Systems

Salman Khetani
Deok-Ho Kim
Andre Levchenko

Translational Research

Associate Editor

Chia-Ching (Josh) Wu
National Cheng Kung University

Jing An
Pan Pan Chong
Hyacinth Idu Hyacinth
Monica M. Jablonski
Chulso Moon
Esther Obeng
Athena Starland-Davenport

EBM eBook Copyright Statement

The copyright in the text of individual articles in this eBook is the property of their respective authors or their respective institutions or funders. The copyright in graphics and images within each article may be subject to copyright of other parties. In both cases this is subject to a license granted to Frontiers.

The compilation of articles constituting this eBook is the property of Frontiers.

Each article within this eBook, and the eBook itself, are published under the most recent version of the Creative Commons CC-BY licence. The version current at the date of publication of this eBook is CC-BY 4.0. If the CC-BY licence is updated, the licence granted by Frontiers is automatically updated to the new version.

When exercising any right under the CC-BY licence, Frontiers must be attributed as the original publisher of the article or eBook, as applicable.

Authors have the responsibility of ensuring that any graphics or other materials which are the property of others may be included in the CC-BY licence, but this should be checked before relying on the CC-BY licence to reproduce those materials. Any copyright notices relating to those materials must be complied with.

Copyright and source acknowledgement notices may not be removed and must be displayed in any copy, derivative work or partial copy which includes the elements in question.

All copyright, and all rights therein, are protected by national and international copyright laws. The above represents a summary only. For further information please read Frontiers' Conditions for Website Use and Copyright Statement, and the applicable CC-BY licence.

ISSN 1535-3699
ISBN 978-2-8325-5879-9
DOI 10.3389/978-2-8325-5879-9

Table of contents

Biochemistry and Molecular Biology

Bioimaging

Highlight

Biomedical Engineering

Genomics, Proteomics, and Bioinfomatics

Feature

Immunology/Microbiology/Virology

EBM Experimental Biology and Medicine

TYPE Original Research
PUBLISHED 22 November 2024
DOI 10.3389/ebm.2024.10303

*CORRESPONDENCE
Nisrine Bissar,
n.bissar@bau.edu.lb

RECEIVED 26 June 2024
ACCEPTED 07 November 2024
PUBLISHED 22 November 2024

CITATION
Bissar N, Kassir R, Salami A and El Shamieh S (2024) Association of immunity-related gene SNPs with Alzheimer's disease.
Exp. Biol. Med. 249:10303.
doi: 10.3389/ebm.2024.10303

Association of immunity-related gene SNPs with Alzheimer's disease

Nisrine Bissar[1]*, Rayan Kassir[1], Ali Salami[2] and Said El Shamieh[3]

[1]Department of Medical Laboratory Technology, Faculty of Health Sciences, Beirut Arab University, Beirut, Lebanon, [2]Faculty of Sciences (V), Lebanese University, Nabatieh, Lebanon, [3]Molecular Testing Laboratory, Department of Medical Laboratory Technology, Faculty of Health Sciences, Beirut Arab University, Beirut, Lebanon

Abstract

Alzheimer's disease (AD) is a prevalent neurodegenerative disorder characterized by progressive cognitive decline. Genetic factors have been implicated in disease susceptibility as its etiology remains multifactorial. The *CD33* and the *HLA-DRB1* genes, involved in immune responses, have emerged as potential candidates influencing AD risk. In this study, 644 Lebanese individuals, including 127 AD patients and 250 controls, were genotyped, by KASP assay, for six SNPs selected from the largest GWAS study in 2021. Logistic regression analysis assessed the association between SNP genotypes and AD risk, adjusting for potential confounders. Among the six SNPs analyzed, rs1846190G>A in *HLA-DRB1* and rs1354106T>G in *CD33* showed significant associations with AD risk in the Lebanese population ($p < 0.05$). Carriers of the AG and AA genotypes of rs1846190 in *HLA-DRB1* exhibited a protective effect against AD (AG: OR = 0.042, p = 0.026; AA: OR = 0.052, p = 0.031). The GT genotype of rs1354106T>G in *CD33* was also associated with reduced risk (OR = 0.173, p = 0.005). Following Bonferroni correction, a significant correlation of rs1354106T > G with AD risk was established. Our results might highlight the complex interplay between genetic and immunological factors contributing to the development of the disease.

KEYWORDS

Alzheimer's disease, immunity genes, Lebanese population, CD33, rs1354106

Impact statement

Neuroinflammation and innate immunity have recently emerged as important contributors to AD pathology. GWAS studies pinpointed the association of immunity-related gene SNPs, including, rs1354106T>G in *CD33* rs1846190G>A in *HLA-DRB1*, with AD. However, these studies were limited in the applicability to non-European populations. Our study reports a significant association of rs1354106T>G with AD in a Middle Eastern population, the Lebanese population, for the first time. This further confirms association results and improves the equity of the previously generated genetic information. On the other hand, the importance of our findings lies in providing

further genetic support for the role of immunity-related genes and SNPs in AD. Our study establishes the protective role of rs1354106T>G SNP, in *CD33*, against AD, previously reported in Sherva et al., 2014 [1] and highlights a potential protective effect of rs1846190G>A in *HLA-DRB1* against AD. These protective variants could enhance AD risk assessment in asymptomatic individuals and offer potential drug targets.

Introduction

Alzheimer's disease (AD) is the most common neurodegenerative disorder, leading to memory loss and multiple cognitive impairments, and is the fourth leading cause of death worldwide among the elderly population [2]. There are two main forms of AD: familial and sporadic [3]. Familial AD typically presents as autosomal dominant and early onset (EOAD), in individuals under 65 years of age, accounting for 1–5% of all cases. EOAD has been linked to mutations in three genes, the *presenilin 1* gene (*PSEN1*), which is identified in up to 70% of cases with familial AD cases; the *presenilin 2* gene (*PSEN2*) and the *Amyloid precursor protein* gene (*APP*) [4]. Sporadic AD, or late-onset AD (LOAD) occurs in individuals older than 65 years, with age being the primary risk factor [5]. LOAD is a complex disorder with several identified risk factors including female sex, traumatic brain injury, depression, environmental pollution, physical inactivity, social isolation, low academic level, and metabolic syndrome [6]. Genetic susceptibility also plays a significant role, particularly the ε4 allele of apolipoprotein E (APOE) [7]. The heritability of LOAD is estimated to be between 60–80% [8]. AD is associated with the presence of β-amyloid (Aβ)-containing extracellular plaques and tau-containing intracellular neurofibrillary tangles in the brains of patients [9]. However, the utility of Aβ as a biomarker for AD has faced challenges, with its detection in about 30% of cognitively normal elderly individuals and with the absence of significant clinical improvements after removing Aβ from the brains of AD patients [10–12]. Neuroinflammation, triggered by pathological damage in the central and peripheral nervous system, is recognized as a significant contributor to AD pathogenesis [13]. This leads to the release of proinflammatory cytokines, chemokines, complement cytokines, and small molecule messengers like prostaglandins, nitric oxide (NO), and reactive oxygen species (ROS) [14]. In addition, persistently activated microglia produce high levels of proinflammatory cytokines and chemokines, leading to neuronal dysfunction [15]. Furthermore, microglia are implicated in synaptic loss, tau phosphorylation, and cognitive decline [16]. Genome-wide association studies (GWAS) indicate that a large percentage of AD risk genes are associated with innate immunity and inflammation, highlighting the critical role the immune system plays in AD pathology [17–19].

The cluster of differentiation 33 gene, *CD33*, on chromosome 19p13.3, is one of the top-ranked AD risk genes identified by genome-wide association studies (GWAS) and has been replicated in numerous genetic analyses [20, 21]. *CD33* belongs to the sialic acid-binding immunoglobulin (Ig)-like family and is a myeloid cell receptor, exclusively expressed by myeloid cells and microglia. It has several functions in cell adhesion, anti-inflammatory signaling, and endocytosis [22]. Clinical and biochemical evidence implicates *CD33* in Aβ-associated pathology by affecting microglia-mediated Aβ clearance [23–25].

CD33 has been implicated in modulating AD susceptibility and the pathology of late-onset Alzheimer's Disease (LOAD) [25–27]. Higher *CD33* expression in the parietal lobe is shown to be associated with more advanced cognitive decline or disease status [24]. Other studies show that reduced expression of *CD33* allows more efficient phagocytic clearance of pathogenic Aβ by microglia and thus protects against AD [25].

HLA, located within the major histocompatibility complex (MHC) on chromosome 6p21, consists of several highly polymorphic and tightly linked genes [28]. Numerous association studies have confirmed significant associations between certain *HLA* gene variants within MHC class I and II regions and AD [29]. The upregulation of HLA class II antigens is widely accepted as a definitive marker of activated microglia, which are implicated in the formation of lesions characteristic of AD [30].

The mechanism by which HLA may contribute to Alzheimer's disease (AD) involves the recognition and processing of pathological protein deposits, such as Aβ peptides, by microglia. Once engulfed by microglia, these proteins are broken down and presented to T lymphocytes in conjunction with specific HLA class I or II molecules. This process triggers B lymphocytes to produce antibodies against Aβ peptides, while activated T lymphocytes target cells producing excessive Aβ for elimination [31]. While this immune cascade is a natural defense mechanism against harmful protein accumulation, excessive reactions may lead to detrimental effects [32, 33]. Consequently, an immune response's severity, scope, and duration can vary depending on the expression of HLA molecules. Individuals carrying certain pathogenic HLA alleles are at a higher risk of developing specific immune-mediated diseases compared to those lacking these alleles [34].

A large GWAS study, including 1,126,563 individuals 90,338 (46,613 proxy) cases and 1,036,225 (318,246 proxy) controls, identified 38 AD risk loci including *CD33* and *HLA-DRB1* with SNP variants (RS1354106T>G) and (RS1846190G>A) consecutively [20]. In this report, we aimed to investigate the correlation between these SNPs and AD in a sample of 644 Lebanese individuals, including 127 AD patients and 250 controls.

Materials and methods

Study subjects

Blood samples were obtained from 644 Lebanese individuals, out of whom, 127 participants were diagnosed with Alzheimer's disease (AD) by neurologists after memory and cognitive tests, functional assessment, physical and neurological exams, diagnostic tests, and brain imaging. Subjects with no Alzheimer's disease were 58 years or older, selected based on the absence of personal or familial psychiatric or cognitive impairment history, and with a Mini-Mental State Examination (MMSE) score above 26 (Table 2). Participants were recruited in accordance with the latest version of the Declaration of Helsinki for Ethical Principles for Medical Research Involving Human Subjects. Ethical approval was obtained from the local IRB Clinical Research Ethics Committee at Beirut Arab University. Each participant underwent a thorough consent process, which included a consent form and questionnaire.

SNP selection

Six SNPs were selected for inclusion in this study based on findings from the largest GWAS study to date conducted by Wightman et al. (2021). This GWAS involved a total of 1,126,563 individuals, comprising 90,338 cases (46,613 proxy) and 1,036,225 controls (318,246 proxy), and identified a total of 38 risk loci, including seven previously unidentified loci.

The SNPs were chosen according to the function and role of their genes in AD pathology. Since this study aims to focus on the role of the immune system in AD, the three SNPs, rs1846190G>A, rs1354106T>G, and rs1582763G>A, were selected based on their respective immunity related genes *HLA-DRB1*, *CD33 and MS4A4A* with well documented association with AD [20, 21, 29, 35]. The remaining three SNPs were selected according to a variety of other functions of their respective genes. These are rs2154482G>T in *APP* gene, a major player of the amyloidogenic pathway of AD pathogenesis [36], rs3935067G>C in *EPHA1*AS 1 long noncoding RNA gene with significant association with AD [37], rs7912495A>G in *ECHDC3*, which is responsible for type 2 diabetes Mellitus-related episodic memory impairment [38].

Genotyping

Genomic DNA was extracted from peripheral blood leukocytes using FlexiGene® DNA kit (QIAGEN) according to the manufacturer's instructions. Genotyping was performed at LGC group (Berlin, Germany) using KASP genotyping assay. KASP is a homogeneous, fluorescence (fluorescence resonance energy transfer) based assay that enables accurate biallelic discrimination of known genetic variations such as SNPs and insertions/deletions as describe previously [39].

Statistical analysis

All analysis was conducted using SPSS software version 24 (SPSS, Inc, Chicago, Illinois). All continuous variables were expressed as mean ± standard deviation. Normality was tested using Shapiro-Wilk test.

Association analysis of the six SNPs with Alzheimer's disease

A binary multiple logistic regression model was employed to investigate the association between the presence of AD (dependent variable, N = 377) and the genotypes of the six SNPs, while adjusting for potential confounders. Covariates, including age, gender, body mass index, educational level, smoking status, and marital status, were selected based on their established connections with AD and their potential to introduce confounding effects into the SNP-disease association analysis.

Results

The characteristics of all study participants are described in Table 1. The average age is 61, with 37.4% being females. Of 612 participants, 28.1% had normal weight, 32.4% were overweight, and 242 (39.5%) were obese. Education levels varied also as 25.9% had no formal education, 59.0% attended some school, 3.3% completed high school, and 12.0% attended university. Additionally, 38.1% of the participants were smokers. Blood pressure and lipid measurements were also recorded.

The characteristics of AD patients and controls are described in Table 2. The mean age of AD patients (80.99 ± 7.94) was significantly greater than the mean age of controls (70.06 ± 8.82) ($p < 0.001$). Moreover, there were significant differences between AD subjects and controls in terms of marital status, number of smokers.

The SNP allele frequencies detected in our study showed minimal variation from the allele frequencies in the Middle Eastern populations (GnomAD) (Table 3). The minor allele frequencies ranged from 0.23 to 0.49, suggesting that these alleles were relatively common in the studied population. The observed genotype frequencies of rs1846190G>A and rs1354106T>G did not show significant deviations from the Hardy-Weinberg equilibrium (HWE). AG and AA carriers of the rs1846190G>A SNP had a decreased risk of AD (OR = 0.042,

TABLE 1 Characteristics of all study participants.

		Participants (n = 644)	
		Mean[a]	SD[b]
n = 638	Age (years) (n = 638)	60.834	18.715
n = 639	Gender n (female %)	239 (37.4)	
n = 612	Body mass index (kg/m^b)	28.971	6.313
	Normal weight (<25) n (%)	172 (28.1)	
	Overweight (25-29.9) n (%)	198 (32.4)	
	Obesity (≥30) n (%)	242 (39.5)	
n = 429	Educational level		
	None n (%)	111 (25.9)	
	School n (%)	253 (59.0)	
	High School n (%)	14 (3.3)	
	University n (%)	51 (11.9)	
n = 544	Smoking n (%)	207 (38.1)	
N = 377	Alzheimer n (%)	127 (33.7%)	
n = 326	SBP (mmHg)	12.379	6.093
n = 323	DBP (mmHg)	7.885	10.050
n = 291	Hypertension n (%)	118 (40.5)	
n = 182	Triglyceride (mg/dL)	147.577	78.687
	High triglycerides levels n (%) (≥150)	65 (35.7)	
n = 184	Total cholesterol (mg/dL)	173.087	45.739
	High total cholesterol levels n (%) (≥190)	64 (34.8)	
n = 180	HDL-C (mg/dL)	44.982	23.489
n = 179	Low HDL-C levels n (%) (≤50 F, ≤40 M)	105 (58.7)	
n = 177	LDL-C (mg/dL)	108.992	83.662
	High LDL-C levels n (%) (≥115)	67 (37.9)	

[a] Mean value for continuous variables and a percentage for categorical variables.

[b] SD, standard deviation (only for continuous variables).

LDL-C, low-density lipoprotein cholesterol; HDL-C, high-density lipoprotein cholesterol; SBP, systolic blood pressure; DBP, diastolic blood pressure.

p = 0.026 and OR = 0.052, p = 0.031 respectively), indicating a much lower likelihood of developing Alzheimer's disease. Likewise, the rs1354106GT genotype had a lower risk (OR = 0.173, p = 0.005) compared to the TT genotype, indicating a significantly lower risk of Alzheimer's disease in the studied population.

Assessment of the association between the six SNPs and the likelihood of developing AD, while adjusting for age, gender, BMI, educational status and smoking showed a significant association with AD for rs1846190G>A (AG; OR = 0.042, P = 0.026 and AA; OR = 0.052, P = 0.031) in *HLA-DRB1* and rs1354106T>G (GT; OR = 0.173, P = 0.005) in *CD33* (Table 4). When applying Bonferroni correction, only rs1354106T>G in *CD33* remained significant thus showing a robust association with AD.

Discussion

In our study, among the six SNPs analyzed, only rs1846190G>A, a regulatory region variant in *HLA-DRB1,* and rs1354106T>G, an intron variant in *CD33,* showed a significant association with AD in the Lebanese population. Following Bonferroni correction, only rs1354106T>G in *CD33* remained

TABLE 2 Characteristics of AD patients and controls.

		Control		Alzheimer		P-value
		N	mean ± SD	N	mean ± SD	
Age (y)		250	70.06 ± 8.82	127	80.99 ± 7.94	<0.001
Sex	female male	N 98 150	% 71.5 63.0	N 39 88	% 28.5 37.0	0.094
Educational level	none School High school university	43 85 5 12	29.7 58.6 3.4 8.3	46 61 0 15	37.7 50.0 0 12.3	0.056
Marital status	single Married Divorced widowed	1 72 43 30	0.7 49.3 29.5 20.5	29 58 6 30	23.6 47.2 4.9 24.4	<0.001
Smoker	no Yes	131 77	63.0 37.0	87 28	75.7 24.3	0.025

significant, which highlights the potential importance of this gene in the pathogenesis of AD.

SNPs have the potential to alter *CD33's* expression level, structure, and function, altering how microglia clear amyloid β [25, 40, 41]. Two previously reported SNPs in *CD33*, rs3865444 and rs12459419, have shown a protective effect against AD [42]. The protective allele of the rs3865444, located in the promotor region, plays a role in the reduction of both *CD33* expression and insoluble Aβ42 levels in AD brain, especially in the microglial cells [25]. Similarly, rs12459419, located in exon 2, and in linkage disequilibrium with rs3865444, exhibits a protective effect by enhancing exon skipping and promoting the production of a short isoform of *CD33*, known as human *CD33m* [43]. Recent studies using cell and animal models have highlighted the functional significance of human *CD33m*, as a gain-of-function variant that enhances Aβ1–42 phagocytosis in microglia [41].

Conversely, a recent computational analysis investigating the 3D structures of *CD33* with rs2455069 A>G SNP suggests a potential increase in the risk of Alzheimer's disease. The study proposes that over time, the CD33-R69G variant, which binds to sialic acid, could boost *CD33's* ability to inhibit the breakdown of amyloid plaques [44].

Our study further explored the association of rs1354106 T>G with AD, revealing a protective effect in Lebanese patients (GT; O. R = 0.173 CI = 0.058–0.586, P = 0.005). This finding notably aligns with the findings from a previous study which utilized a Bayesian longitudinal low-rank regression (L2R2) model to explore the impact of single nucleotide polymorphisms (SNPs). Their results revealed that rs1354106 was associated with a reduced rate of decline in the AD assessment scale cognitive score [1]. Moreover, in the same study, the effect of this SNP on the longitudinal trajectories of the hippocampi was investigated. Results revealed that the minor allele significantly slowed hippocampal atrophy compared to the major allele. This suggests a potential protective effect associated with the minor allele of rs1354106 in patients with Alzheimer's disease and mild cognitive impairment [45]. This is validated by our findings, which indicated a protective role of the rs1354106 T>G in Lebanese AD patients (GT; O. R = 0.173 CI = 0.051–0.586, P = 0.005).

The association between *HLA* gene variants and Alzheimer's disease (AD) risk has been extensively explored across diverse populations. Our study on the Lebanese population, first revealed a protective effect of rs1846190G>A, of *HLA-DRB1* but the association did not stand after Bonferroni correction. *HLA-DRB1* 13:02 protects against age-related neural network deterioration and mitigates the deleterious effects of apoE4 on neural network functioning [46]. Furthermore, a recent study, conducted on the Japanese population, identified a significant association between the *HLA-DRB109:01-DQB1*03:03* haplotype and LOAD risk in APOE ε4–negative individuals [47]. Moreover, studies have emphasized the protective function of *HLA-DRB1*04* against AD, as its presence is correlated with lower CSF tau levels and fewer neurofibrillary tangles in AD subjects [48]. Conversely, *HLA-DRB1*03* was identified as a risk factor for late-onset AD (LOAD) in the German population [31]. Additionally, the SNP rs9271192 in *HLA-DRB5–DRB1* region has been found to influence AD risk through large meta-analyses of genome-wide association studies (GWAS) in Caucasian populations [48]. These findings have been replicated successfully in two large-scale studies conducted on the Chinese population [49, 50].

TABLE 3 The loci, allele frequencies, and genetic effects of the six SNPs in this study.

SNP	Position (GRCh38.p14)	MAF	Population Frequency	Gene	Consequence
rs1846190G>A	6:32616036	0.24	0.2279	*HLA-DRB1*	Intron variant
rs3935067G>C	7:143407238	0.37	0.3844	*EPHA1-AS1*	2KB Upstream Variant
rs7912495A>G	10:11,676,714	0.47	0.4728	*ECHDC3*	Non Coding Transcript Variant
rs1582763G>A	11:60254475	0.42	0.4252	*MS4A4A*	Intron variant
rs1354106T>G	19:51234736	0.23	0.3129	*CD33*	Intron variant
rs2154482G>T	21:26148613	0.49	0.4863	*APP*	Intron variant

SNP, single nucleotide polymorphism; MAF, minor allele frequency.

TABLE 4 Multiple Logistic Regression analysis of risk factors with Alzheimer's disease.

Alzheimer's diseases (N = 377)			
		Or (95% C.I.)	p
Age	65–69	1	0.435
	70–74	2.245 (0.294–17.130)	
	75–79	2.233(0.388–12.836)	0.368
	>80	4.341(0.792–23.803)	0.091
Gender	Male	1	
	Female	0.629(0.203–1.956)	0.424
BMI	<25	1	
	25–29.9	1.962(0.577–6.673)	0.281
	≥30	0.245(0.040–1.532)	0.133
Educational level	None	1	
	School	0.729(0.231–2.298)	0.589
	High School	5.418(0.652–45.040)	0.118
	University	-	-
Smoking	No	1	
	Yes	0.388(0.103–1.454)	0.161
rs1846190 in *HLA-DRB1*	GG	1	
	AG	0.042(0.003–0.681)	0.026
	AA	0.052(0.004–0.763)	0.031
rs3935067 in *EPHA1-AS1*	GG	1	
	GC	0.536(0.153–1.876)	0.329
	CC	2.959(0.497–17.625)	0.234
rs7912495 in *ECHDC3*	AA		
	AG	0.498(0.136–1.829)	0.293
	GG	0.581(0.101–3.331)	0.543
rs1582763 in *MS4A4A*	GG		
	AG	1.855(0.534–6.441)	0.331
	AA	3.332(0.640–17.349)	0.153
rs1354106 in *CD33*	TT	1	
	GT	0.173(0.051–0.586)	0.005
	GG	0.233(0.024–2.270)	0.210
rs2154482 in *APP*	TT		
	GT	3.658(0.796–16.817)	0.096
	GG	1.740(0.300–10.074)	0.537

A recent study examined global cortical amyloid PET burden, incorporating the 38 gene variants, from the GWAS study, using PRSice-2, to assess overall phenotypic variance in two cohorts [20]. The analysis revealed a strong association between AD risk variants (such as *APOE*, *PICALM*, *CR1*, and *CLU*) and amyloid PET levels in both cohorts. Importantly, neither *CD33* rs1354106T>A nor *HLA-DRB1* rs1846190G>A demonstrated an association with amyloid PET levels in this study [51]. This underscores the alignment of our findings with existing evidence concerning the protective effect of both variants against Alzheimer's disease risk.

In conclusion, understanding protective variants could refine AD risk assessment in asymptomatic individuals, aiding AD prevention. Furthermore, identifying genetic variants that confer protection *via* a loss-of-function or gain-of-function offers potential drug targets. Most drug candidates never reach the clinic, but those with the same mechanism as protective variants have a higher success rate. Our current study has provided convincing statistical support for an association between *CD33* polymorphisms and LOAD. Specifically, the carriage of GT alleles rs1354106 T>G in *CD33* is linked to a protective effect against LOAD in the Lebanese Population. The main limitation of this study is the sample size used, probably affecting the statistical significance of rs1846190 SNP and *HLA-DRB1* association with AD after Bonferroni correction. Further investigations involving larger sample sizes and diverse ethnic groups are needed to validate the role of rs1354106 and examine the potential role of rs1846190 in LOAD.

Author contributions

NB designed the study and supervised sample collection, genotyping procedure, statistical analysis and manuscript writing. AS contributed to statistical analysis. SES contributed to genotyping procedure, statistical analysis and reviewed the manuscript. RK contributed to sample collection, statistical analysis and wrote the manuscript. All authors contributed to the article and approved the submitted version.

Data availability

The original contributions presented in the study are included in the article, further inquiries can be directed to the corresponding author.

Ethics statement

The studies involving humans were approved by Beirut Arab University institutional review board. The studies were conducted in accordance with the local legislation and institutional requirements. The participants provided their written informed consent to participate in this study.

Funding

The author(s) declare that no financial support was received for the research, authorship, and/or publication of this article.

Acknowledgments

We would like to express sincere gratitude to the study participants and their families for their time and effort to help create the present study. Gratitude is also extended to Dar-Al Ajaza Al-Islamia Hospital in Beirut, the Social Services Association in North Lebanon, Bayt Al Shaikhookha in Tripoli, Bayt Al Raha Ozanam in Batroun, and Dar Al Inaya in Jbeil for their invaluable assistance in sample collection. We would also like to thank the field investigators for the recruitment and examination of the population involved in this study, namely N. Mohsen, N. Naja and N. Ramadan.

Conflict of interest

The author(s) declared no potential conflicts of interest with respect to the research, authorship, and/or publication of this article.

References

1. Sherva R, Tripodis Y, Bennett DA, Chibnik LB, Crane PK, de Jager PL, et al. Genome-wide association study of the rate of cognitive decline in Alzheimer's disease. *Alzheimer's and Dementia* (2014) **10**(1):45–52. doi:10.1016/j.jalz.2013.01.008

2. DeTure MA, Dickson DW. The neuropathological diagnosis of Alzheimer's disease. *Mol neurodegeneration* (2019) **14**(1):32. doi:10.1186/s13024-019-0333-5

3. Long JM, Holtzman DM. Alzheimer disease: an update on pathobiology and treatment strategies. *Cell* (2019) **179**(2):312–39. doi:10.1016/j.cell.2019.09.001

4. Andrade-Guerrero J, Santiago-Balmaseda A, Jeronimo-Aguilar P, Vargas-Rodríguez I, Cadena-Suárez AR, Sánchez-Garibay C, et al. Alzheimer's disease: an updated overview of its genetics. *Int J Mol Sci* (2023) **24**(4):3754. doi:10.3390/ijms24043754

5. Silva MV, Loures CD, Alves LC, De Souza LC, Borges KB, Carvalho MD. Alzheimer's disease: risk factors and potentially protective measures. *J Biomed Sci* (2019) **26**:33–1. doi:10.1186/s12929-019-0524-y

6. Livingston G, Sommerlad A, Orgeta V, Costafreda SG, Huntley J, Ames D, et al. Dementia prevention, intervention, and care. *The Lancet* (2017) **390**(10113):2673–734. doi:10.1016/s0140-6736(17)31363-6

7. Bezprozvanny I. Alzheimer's disease–Where do we go from here? *Biochem Biophysical Res Commun* (2022) **633**:72–6. doi:10.1016/j.bbrc.2022.08.075

8. Bellenguez C, Küçükali F, Jansen IE, Kleineidam L, Moreno-Grau S, Amin N, et al. New insights into the genetic etiology of Alzheimer's disease and related dementias. *Nat Genet* (2022) **54**(4):412–36. doi:10.1038/s41588-022-01024-z

9. Knopman DS, Amieva H, Petersen RC, Chételat G, Holtzman DM, Hyman BT, et al. Alzheimer disease. *Nat Rev Dis primers* (2021) **7**(1):33. doi:10.1038/s41572-021-00269-y

10. Kruse N, Persson S, Alcolea D, Bahl JM, Baldeiras I, Capello E, et al. Validation of a quantitative cerebrospinal fluid alpha-synuclein assay in a European-wide interlaboratory study. *Neurobiol Aging* (2015) **36**(9):2587–96. doi:10.1016/j.neurobiolaging.2015.05.003

11. Herrup K. The case for rejecting the amyloid cascade hypothesis. *Nat Neurosci* (2015) **18**(6):794–9. doi:10.1038/nn.4017

12. Villemagne VL, Pike KE, Chételat G, Ellis KA, Mulligan RS, Bourgeat P, et al. Longitudinal assessment of Aβ and cognition in aging and Alzheimer disease. *Ann Neurol* (2011) **69**(1):181–92. doi:10.1002/ana.22248

13. Wang C, Zong S, Cui X, Wang X, Wu S, Wang L, et al. The effects of microglia-associated neuroinflammation on Alzheimer's disease. *Front Immunol* (2023) **14**:1117172. doi:10.3389/fimmu.2023.1117172

14. Leng F, Edison P. Neuroinflammation and microglial activation in Alzheimer disease: where do we go from here? *Nat Rev Neurol* (2021) **17**(3):157–72. doi:10.1038/s41582-020-00435-y

15. Mrak RE, Griffin WST, Griffin WS. Microglia and neuroinflammation: a pathological perspective. *J neuroinflammation* (2004) **1**:1–4. doi:10.1186/1742-2094-1-1

16. Mander BA, Dave A, Lui KK, Sprecher KE, Berisha D, Chappel-Farley MG, et al. Inflammation, tau pathology, and synaptic integrity associated with sleep spindles and memory prior to β-amyloid positivity. *Sleep* (2022) **45**(9):zsac135. doi:10.1093/sleep/zsac135

17. Shigemizu D, Mori T, Akiyama S, Higaki S, Watanabe H, Sakurai T, et al. Identification of potential blood biomarkers for early diagnosis of Alzheimer's disease through RNA sequencing analysis. *Alzheimer's Res and Ther* (2020) **12**:87–2. doi:10.1186/s13195-020-00654-x

18. Pimenova AA, Raj T, Goate AM. Untangling genetic risk for Alzheimer's disease. *Biol Psychiatry* (2018) **83**(4):300–10. doi:10.1016/j.biopsych.2017.05.014

19. Wes PD, Sayed FA, Bard F, Gan L. Targeting microglia for the treatment of Alzheimer's Disease. *Glia* (2016) **64**(10):1710–32. doi:10.1002/glia.22988

20. Wightman DP, Jansen IE, Savage JE, Shadrin AA, Bahrami S, Holland D, et al. A genome-wide association study with 1,126,563 individuals identifies new risk loci for Alzheimer's disease. *Nat Genet* (2021) **53**(9):1276–82. doi:10.1038/s41588-021-00921-z

21. Zhao L. CD33 in Alzheimer's disease–biology, pathogenesis, and therapeutics: a mini-review. *Gerontology* (2019) **65**(4):323–31. doi:10.1159/000492596

22. Wang WY, Liu Y, Wang HF, Tan L, Sun FR, Tan MS, et al. Impacts of CD33 genetic variations on the atrophy rates of Hippocampus and parahippocampal gyrus in normal aging and mild cognitive impairment. *Mol Neurobiol* (2017) **54**:1111–8. doi:10.1007/s12035-016-9718-4

23. Karch CM, Goate AM. Alzheimer's disease risk genes and mechanisms of disease pathogenesis. *Biol Psychiatry* (2015) **77**(1):43–51. doi:10.1016/j.biopsych.2014.05.006

24. Bradshaw EM, Chibnik LB, Keenan BT, Ottoboni L, Raj T, Tang A, et al. CD33 Alzheimer's disease locus: altered monocyte function and amyloid biology. *Nat Neurosci* (2013) **16**(7):848–50. doi:10.1038/nn.3435

25. Griciuc A, Serrano-Pozo A, Parrado AR, Lesinski AN, Asselin CN, Mullin K, et al. Alzheimer's disease risk gene CD33 inhibits microglial uptake of amyloid beta. *Neuron* (2013) **78**(4):631–43. doi:10.1016/j.neuron.2013.04.014

26. Hollingworth P, Harold D, Sims R, Gerrish A, Lambert JC, Carrasquillo MM, et al. Common variants at ABCA7, MS4A6A/MS4A4E, EPHA1, CD33 and CD2AP are associated with Alzheimer's disease. *Nat Genet* (2011) **43**(5):429–35. doi:10.1038/ng.803

27. Carrasquillo MM, Belbin O, Hunter TA, Ma L, Bisceglio GD, Zou F, et al. Replication of EPHA1 and CD33 associations with late-onset Alzheimer's disease: a multi-centre case-control study. *Mol neurodegeneration* (2011) **6**:54–9. doi:10.1186/1750-1326-6-54

28. Horton R, Wilming L, Rand V, Lovering RC, Bruford EA, Khodiyar VK, et al. Gene map of the extended human MHC. *Nat Rev Genet* (2004) **5**(12):889–99. doi:10.1038/nrg1489

29. Aliseychik MP, Andreeva TV, Rogaev EI. Immunogenetic factors of neurodegenerative diseases: the role of HLA class II. *Biochemistry (Moscow)* (2018) **83**:1104–16. doi:10.1134/s0006297918090122

30. McGeer PL, McGeer EG, Yasojima K. *Alzheimer disease and neuroinflammation*. Vienna: Springer (2000).

31. Wang ZX, Wan Q, Xing A. HLA in Alzheimer's disease: genetic association and possible pathogenic roles. *NeuroMolecular Med* (2020) **22**(4):464–73. doi:10.1007/s12017-020-08612-4

32. Kusdra L, Rempel H, Yaffe K, Pulliam L. Elevation of CD69+ monocyte/macrophages in patients with Alzheimer's disease. *Immunobiology* (2000) **202**(1):26–33. doi:10.1016/s0171-2985(00)80049-2

33. Malm TM, Magga J, Kuh GF, Vatanen T, Koistinaho M, Koistinaho J. Minocycline reduces engraftment and activation of bone marrow-derived cells but sustains their phagocytic activity in a mouse model of Alzheimer's disease. *Glia* (2008) **56**(16):1767–79. doi:10.1002/glia.20726

34. Zota V, Nemirovsky A, Baron R, Fisher Y, Selkoe DJ, Altmann DM, et al. HLA-DR alleles in amyloid β-peptide autoimmunity: a highly immunogenic role for the DRB1*1501 allele. *The J Immunol* (2009) **183**(5):3522–30. doi:10.4049/jimmunol.0900620

35. Sanyal R, Polyak MJ, Zuccolo J, Puri M, Deng L, Roberts L, et al. MS4A4A: a novel cell surface marker for M2 macrophages and plasma cells. *Immunol and Cell Biol* (2017) **95**(7):611–9. doi:10.1038/icb.2017.18

36. Thinakaran G, Koo EH. Amyloid precursor protein trafficking, processing, and function. *J Biol Chem* (2008) **283**(44):29615–9. doi:10.1074/jbc.r800019200

37. De Rojas I, Moreno-Grau S, Tesi N, Grenier-Boley B, Andrade V, Jansen IE, et al. Common variants in Alzheimer's disease and risk stratification by polygenic risk scores. *Nat Commun* (2021) **12**(1):3417. doi:10.1038/s41467-021-22491-8

38. Zhao Q, Du X, Liu F, Zhang Y, Qin W, Zhang Q. ECHDC3 variant regulates the right hippocampal microstructural integrity and verbal memory in type 2 diabetes Mellitus. *Neuroscience* (2024) **538**:30–9. doi:10.1016/j.neuroscience.2023.12.003

39. Masri I, Salami A, El Shamieh S, Bissar-Tadmouri N. rs3851179G> A in PICALM is protective against Alzheimer's disease in five different countries surrounding the Mediterranean. *Curr Aging Sci* (2020) **13**(2):162–8. doi:10.2174/1874609812666191019143237

40. Efthymiou AG, Goate AM. Late onset Alzheimer's disease genetics implicates microglial pathways in disease risk. *Mol neurodegeneration* (2017) **12**:43–2. doi:10.1186/s13024-017-0184-x

41. Bhattacherjee A, Jung J, Zia S, Ho M, Eskandari-Sedighi G, St. Laurent CD, et al. The CD33 short isoform is a gain-of-function variant that enhances Aβ1–42 phagocytosis in microglia. *Mol Neurodegeneration* (2021) **16**:19–22. doi:10.1186/s13024-021-00443-6

42. Jiang YT, Li HY, Cao XP, Tan L. Meta-analysis of the association between CD33 and Alzheimer's disease. *Ann translational Med* (2018) **6**(10):169. doi:10.21037/atm.2018.04.21

43. Malik M, Simpson JF, Parikh I, Wilfred BR, Fardo DW, Nelson PT, et al. CD33 Alzheimer's risk-altering polymorphism, CD33 expression, and exon 2 splicing. *The J Neurosci* (2013) **33**(33):13320–5. doi:10.1523/jneurosci.1224-13.2013

44. Tortora F, Rendina A, Angiolillo A, Di Costanzo A, Aniello F, Donizetti A, et al. CD33 rs2455069 SNP: correlation with Alzheimer's disease and hypothesis of functional role. *Int J Mol Sci* (2022) **23**(7):3629. doi:10.3390/ijms23073629

45. Apostolova LG, Green AE, Babakchanian S, Hwang KS, Chou YY, Toga AW, et al. Hippocampal atrophy and ventricular enlargement in normal aging, mild cognitive impairment (MCI), and Alzheimer Disease. *Alzheimer Dis and Associated Disord* (2012) **26**(1):17–27. doi:10.1097/wad.0b013e3182163b62

46. James LM, Georgopoulos AP. Human leukocyte antigen as a key factor in preventing dementia and associated apolipoprotein E4 risk. *Front Aging Neurosci* (2019) **11**:82. doi:10.3389/fnagi.2019.00082

47. Shigemizu D, Fukunaga K, Yamakawa A, Suganuma M, Fujita K, Kimura T, et al. The HLA-DRB1*09:01-DQB1*03:03 haplotype is associated with the risk for late-onset Alzheimer's disease in APOE $${{\varepsilon }}$$4–negative Japanese adults. *npj Aging.* (2024) **10**(1):3. doi:10.1038/s41514-023-00131-3

48. Lambert JC, Ibrahim-Verbaas CA, Harold D, Naj AC, Sims R, Bellenguez C, et al. Meta-analysis of 74,046 individuals identifies 11 new susceptibility loci for Alzheimer's disease. *Nat Genet* (2013) **45**(12):1452–8. doi:10.1038/ng.2802

49. Jiao B, Liu X, Zhou L, Wang MH, Zhou Y, Xiao T, et al. Polygenic analysis of late-onset Alzheimer's disease from mainland China. *PloS one* (2015) **10**(12):e0144898. doi:10.1371/journal.pone.0144898

50. Lu RC, Yang W, Tan L, Sun FR, Tan MS, Zhang W, et al. Association of HLA-DRB1 polymorphism with Alzheimer's disease: a replication and meta-analysis. *Oncotarget* (2017) **8**(54):93219–26. doi:10.18632/oncotarget.21479

51. Ramanan VK, Heckman MG, Przybelski SA, Lesnick TG, Lowe VJ, Graff-Radford J, et al. Polygenic scores of Alzheimer's disease risk genes add only modestly to APOE in explaining variation in amyloid PET burden. *J Alzheimer's Dis* (2022) **88**(4):1615–25. doi:10.3233/jad-220164

EBM Experimental Biology and Medicine

TYPE Original Research
PUBLISHED 23 October 2024
DOI 10.3389/ebm.2024.10333

*CORRESPONDENCE
Minhaj Nur Alam,
malam8@charlotte.edu

RECEIVED 02 August 2024
ACCEPTED 07 October 2024
PUBLISHED 23 October 2024

CITATION
Badhon RH, Thompson AC, Lim JI, Leng T and Alam MN (2024) Quantitative characterization of retinal features in translated OCTA. *Exp. Biol. Med.* 249:10333. doi: 10.3389/ebm.2024.10333

Quantitative characterization of retinal features in translated OCTA

Rashadul Hasan Badhon[1], Atalie Carina Thompson[2], Jennifer I. Lim[3], Theodore Leng[4] and Minhaj Nur Alam[1]*

[1]Department of Electrical and Computer Engineering, University of North Carolina at Charlotte, Charlotte, NC, United States, [2]Department of Surgical Ophthalmology, Atrium-Health Wake Forest Baptist, Winston-Salem, NC, United States, [3]Department of Ophthalmology and Visual Science, University of Illinois at Chicago, Chicago, IL, United States, [4]Department of Ophthalmology, Stanford University School of Medicine, Stanford, CA, United States

Abstract

This study explores the feasibility of quantitative Optical Coherence Tomography Angiography (OCTA) features translated from OCT using generative machine learning (ML) for characterizing vascular changes in retina. A generative adversarial network framework was employed alongside a 2D vascular segmentation and a 2D OCTA image translation model, trained on the OCT-500 public dataset and validated with data from the University of Illinois at Chicago (UIC) retina clinic. Datasets are categorized by scanning range (Field of view) and disease status. Validation involved quality and quantitative metrics, comparing translated OCTA (TR-OCTA) with ground truth OCTAs (GT-OCTA) to assess the feasibility for objective disease diagnosis. In our study, TR-OCTAs showed high image quality in both 3 and 6 mm datasets (high-resolution and contrast quality, moderate structural similarity compared to GT-OCTAs). Vascular features like tortuosity and vessel perimeter index exhibits more consistent trends compared to density features which are affected by local vascular distortions. For the validation dataset (UIC), the metrics show similar trend with a slightly decreased performance since the model training was blind on UIC data, to evaluate inference performance. Overall, this study presents a promising solution to the limitations of OCTA adoption in clinical practice by using vascular features from TR-OCTA for disease detection. By making detailed vascular imaging more widely accessible and reducing reliance on expensive OCTA equipment, this research has the potential to significantly enhance the diagnostic process for retinal diseases.

KEYWORDS

GAN, generative AI, OCT, OCTA, OCTA features

Impact statement

This study represents a significant advancement in retinal imaging by demonstrating the feasibility of using generative machine learning to translate OCT features into OCTA features, addressing a critical gap in clinical practice. By employing a generative adversarial network framework trained on diverse datasets, the research establishes quantitative features in Translated OCTA. This innovation enhances the ability to objectively diagnose retinal diseases by providing reliable vascular imaging without the need for costly OCTA equipment. The findings reveal that vascular features from TR-OCTA, such as tortuosity and vessel perimeter index, offer more consistent diagnostic trends compared to traditional density features. This new information has the potential to transform retinal disease diagnostics, making detailed vascular imaging more accessible and cost-effective, thereby improving patient outcomes and broadening the adoption of advanced imaging techniques in routine clinical settings.

Introduction

Optical Coherence Tomography (OCT) is a cutting-edge medical imaging technology that has revolutionized our ability to observe and comprehend the complex structures of biological tissues. It is non-invasive and capable of providing highly detailed in-depth retinal pathologies. It generates high-resolution cross-sectional images of tissues using low-coherence light, therefore has been widely adopted in ophthalmic clinical care [1]. As a result, OCT has been demonstrated for early identification and monitoring of various retinal illnesses including diabetic retinopathy (DR), age-related macular degeneration (AMD) and glaucoma that cannot be obtained by any other non-invasive diagnostic technique [2–8].

The rapid development of OCT, growing interest in this field, and its increasing impact in clinical medicine has contributed to its widespread availability. However, due to its non-dynamic imaging technology, conventional OCT cannot visualize blood flow information such as blood vessel caliber or density and remains only limited to capturing structural information [2, 9]. As a result of this information gap, OCT angiography (OCTA) was developed which can produce volumetric data from choroidal and retinal layers and provide both structural and blood flow information [10, 11]. OCTA provides a high-resolution image of the retinal vasculature at the capillary level, allowing for reliable detection of microvascular anomalies in diabetic eyes and vascular occlusions. It helps to quantify vascular impairment based on the severity of retinal diseases. In recent years, OCTA has been demonstrated to identify, detect, and predict DR [12–19], AMD [20–22], Glaucoma [23] and several other retinal diseases [24–31]. Despite the advantages, widespread deployment of OCTA has been limited due to the high device cost [32, 33]. The additional requirements of hardware and software for an OCTA device pose a financial burden for clinics as well as patients This is one of the major reasons that only a limited number of hospitals and retinal clinics use OCTA for in-depth retinal vascular analysis. Another limitation of OCTA is the process of generating an OCTA scan, which takes longer time and involves repetitive scanning of the retina making the data acquisition harder due to involuntary eye movements and motion artifacts, reducing the quality of OCTA images [33]. Due to the limitation of OCTA data, most studies involving OCTA based imaging biomarkers and involving the use of artificial intelligence (AI) are difficult to validate extensively for future clinical deployment.

From literature, a potential solution to this problem can be the utilization of AI and machine learning (ML) to produce OCTA images from the already available OCT data which has been showing promising outcomes [34–39]. Incorporating ML for OCTA translation from OCT offers significant advances in ophthalmic diagnostics by increasing angiographic and functional information in existing OCT data. This transition harnesses ML's capability to autonomously analyse OCT scans and generate detailed vascular images, traditionally obtained through OCTA, aligned with OCT information. By doing so, it substantially lowers the barriers to accessing high-resolution vascular imaging, which is crucial for diagnosing and monitoring retinal diseases and provides a robust detection system. Furthermore, ML dependent approaches alleviate some of OCTA's limitations, including its high cost, susceptibility to artifacts from patient movement and the extensive time required for image acquisition.

Different studies have been reported [40–42] attempting to leverage ML algorithms for generative-adversarial learning, typically utilizing a UNet for image translation in recent years. However the quality of the translated OCTA (TR-OCTA) is usually sub-optimal and the retinal vascular areas are not refined enough. The first application of this approach was reported by Lee et al., 2019 [34] to train an algorithm to generate retinal flow maps from OCT images avoiding the needs for labelling but it was limited to capture higher density of deep capillary networks. According to some recent studies [35–37], incorporating textual information or surrounding pixels, it is possible to improve the OCTA image quality. Le et. Al [39] proposed another approach incorporating spatial speckle variance and generative AI, however, it requires OCT/OCTA data from custom devices. In this paper, we adopt and implement a generative-adversarial learning framework-based algorithm demonstrated by Li et al [36] for translating OCT data into OCTA. The focus of this study is to demonstrate the feasibility of using such TR-OCTA image generated vascular features (Blood Vessel Density (BVD), Blood Vessel Caliber (BVC), Blood Vessel Tortuosity (BVT), Vessel Perimeter Index (VPI)) for disease detection. We compare these OCTA features with ground truth (GT) – OCTAs. The quality of the TR-OCTAs were compared with features such as Structural Similarity Index Measure (SSIM), Fréchet Inception Distance (FID) and patch-based contrast quality index (PCQI). From our observation and statistical analysis, we found that overall, the SSIM values indicate a moderate level of structural similarity between TR-OCTA and GT-OCTA images, with some variability across different patient categories and scan range however PCQI scores are quite close for both dataset and some deviation in FID scores is noticeable. It was observed that the model generally achieved a slightly better performance in depicting normal and pathological retinal features for the 3 mm scans compared to the 6 mm. However, across both field of view (FoV), there were slight discrepancies in quantitative vascular metrics such as BVD, BVC and VPI, highlighting areas where the translation model could be further refined. This analysis underscores the potential of using AI-driven translation models for OCTA image analysis, while also pointing to the need for improvements to enhance the accuracy of vascular feature representation, particularly at varying FoV.

Materials and methods

The overall methodology of our feature extraction pipeline is demonstrated in Figure 1. We first translate OCT data into OCTA (using algorithm demonstrated by Li et. al [36]) and quantify the retinal features in both GT and TR-OCTAs for validation.

Translation algorithm

We adopted and implemented the OCT to OCTA translation algorithm from Li et al [36]. We describe the process here briefly. The process of OCTA translation from OCT images is carried out in 3 steps (Figure 1): (a) generating 3D OCTA volumes from paired 3D OCT volumes using conditional generative adversarial network (GAN), (b) improving image quality by focusing only the vascular regions, utilizing the 2DVSeg model, thorough vascular segmentation, (c) preserving contextual information for better quality translated images through a 2D translation model (2DTR) generating 2D paired OCTA maps. The baseline architecture of the translation model is built upon pix2pix, an image translation model [41]. The aim of the model is primarily to translate OCT volumes to its paired OCTA volume as closely as possible to the original clinical images. [4] The framework includes a 3D GAN where the 3D generator takes a 3D OCT volume as its input and outputs a corresponding TR-OCTA volume. a 3D discriminator is used to effectively distinguish between the original (ground-truth) OCTA volumes and the generated ones. An adversarial loss is used to train both the generator and discriminator. Furthermore, to calculate for each pixel difference between TR-OCTA and GT-OCTA, a distance loss is considered. The framework also uses a 2D vascular segmentation model (Figure 2A) to help with the improved quality of the vascular regions by utilizing OCTA reflected vascular data by focusing on the vascular areas during the 3D volume translation process.

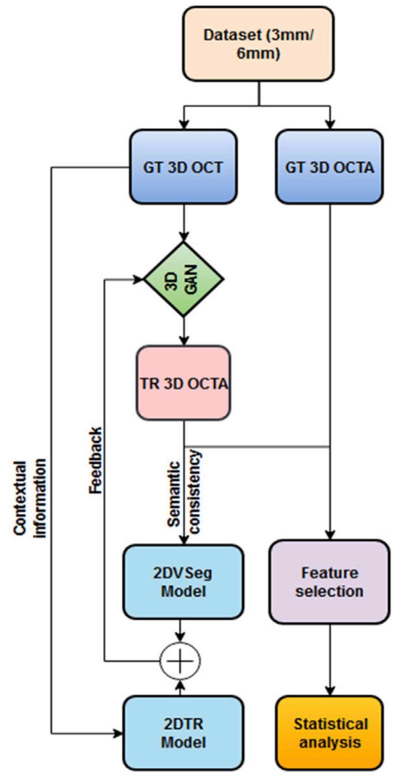

FIGURE 1
Framework of OCT to OCTA translation and characterization of quantitative features.

This model also utilizes a 2D generative translation model (Figure 2B) to build heuristic (suboptimal) 2D OCTA projection maps from their corresponding OCT that can provide heuristic contextual information where output values are affected by the surrounding pixels resulting in outputs with additional contextual information.

Comparative feature analysis

The generated TR-OCTA maps were compared on several quantitative features to the GT projection maps for comparison: BVD, BVC, BVT, and VPI. Also, for qualitative comparison: SSIM, FID and PCQI metrics were used to quantify the translated image quality and similarity to GT OCTA maps. All the metrics evaluation were performed using MATLAB and Python. Feature values were calculated separately for 3 mm and 6 mm across different patient groups and compared between the OCT500 and UIC datasets. A two-tail t-test was carried out for each feature to compare if there is a significant difference between the TR-OCTA and GT-OCTA values with a p value <0.05.

Metrics and features

Similarity metrics

We used three metrics to compare GT and TR-OCTAs, as described below:

SSIM: SSIM or Structural Similarity Index Measure, is a method for measuring the similarity between two images. SSIM is based on the perception of the human visual system and it considers changes in structural information, luminance and contrast. The idea is that pixels have strong inter-dependencies, especially when they are spatially close. These dependencies carry important information about the structure of the objects in the visual scene.

FID: FID score is a metric used to evaluate the quality of images generated by models, such as those produced by GANs. It measures the similarity between two sets of images, typically between a set of generated images and a set of real images, by comparing the statistics of their features extracted by a pre-trained Inception model [43]. The FID score calculates the distance between the feature vectors of the real and generated images, using the Fréchet distance (also known as the Wasserstein-2 distance). A lower FID score indicates that the distribution of the generated images is closer to the distribution of the real images, suggesting higher quality and more realistic images.

PCQI: PCQI is another metric designed to assess the quality of images by focusing on local contrast changes, which are crucial for visual perception, especially in textured regions [44]. Unlike many traditional image quality metrics that evaluate images globally, PCQI operates on small, localized patches of an image, making it particularly effective at capturing and evaluating detailed contrast differences between a reference image and a test image. PCQI calculates the quality score based on three main aspects: patch similarity, contrast distortion, and mean luminance change, within these localized regions. The final score is a weighted sum of these aspects, providing a single quality metric that reflects how perceptually close the test image is to the reference image in terms of local contrast and brightness. A higher PCQI score indicates a better match between the test and reference images, suggesting less contrast distortion and more accurate reproduction of the original image's visual quality.

Quantitative OCTA features

We characterized three vessel and one density based features (Equations 1–4), as described below:

BVD: BVD or vessel area density (VD) [45], is the ratio of the blood vessels to the total area measured and can be utilized for identifying early detection of retinal pathologies including DR [46, 47], AMD [48, 49] etc.

$$BVD = \frac{vascular\ area}{total\ area} \tag{1}$$

BVC: BVC, also named as vessel diameter index [50], is calculated as the ratio of vessel area to the vessel length [12]. BVC distortion can be used to quantify retinal vascular shrinkage and is typically observed in different retinopathies such as diabetic retinopathy (DR) [51].

$$BVC = \frac{vascular\ area}{vascular\ length} \tag{2}$$

BVT: BVT is defined as a measure of degree of vessel distortion [26, 52]. During any retinal pathologies, distorted vessel structures can affect the blood flow efficiency and can be measured as:

$$BVT = \frac{1}{n}\sum \frac{geodesic\ distance\ between\ end\ points\ for\ a\ vessel\ branch}{euclidean\ distance\ between\ end\ points\ for\ a\ vessel\ branch} \tag{3}$$

here, n = total number of vessel branches.

VPI: VPI [52] is measured as the ratio of the contour length of the vessel boundaries or vessel perimeter to the total vessel area and has been used for detection of DR and sickle cell retinopathy (SCR) from.

OCTA images:

$$VPI = \frac{overall\ contour\ length\ of\ blood\ vessel\ boundaries}{total\ blood\ vessel\ area} \tag{4}$$

Statistical Analysis: We performed statistical analysis based on the selected features to quantify the TR-OCTA and measure the quality of the translation. This analysis will help us improve the accuracy and efficiency of the TR-OCTA translated from GT-OCT and GT-OCTA.

Results

Dataset

We used 2 datasets for our study, a public dataset of 500 patients containing paired 3D OCT and OCTA volumes, OCTA-500 [53] and a dataset of DR patients collected from UIC with 445 scans containing OCT volumes and OCTA projections.

OCT500 dataset is divided into 2 subsets according to their FoV (Field of view), 3 mm and 6 mm. The translation algorithm is applied separately to the two subsets for comparison. The datasets are further divided into different diseased patients and normal patients for quantitative feature comparison. The 3 mm dataset contains 6 AMD patients, 5 Choroidal neovascularization

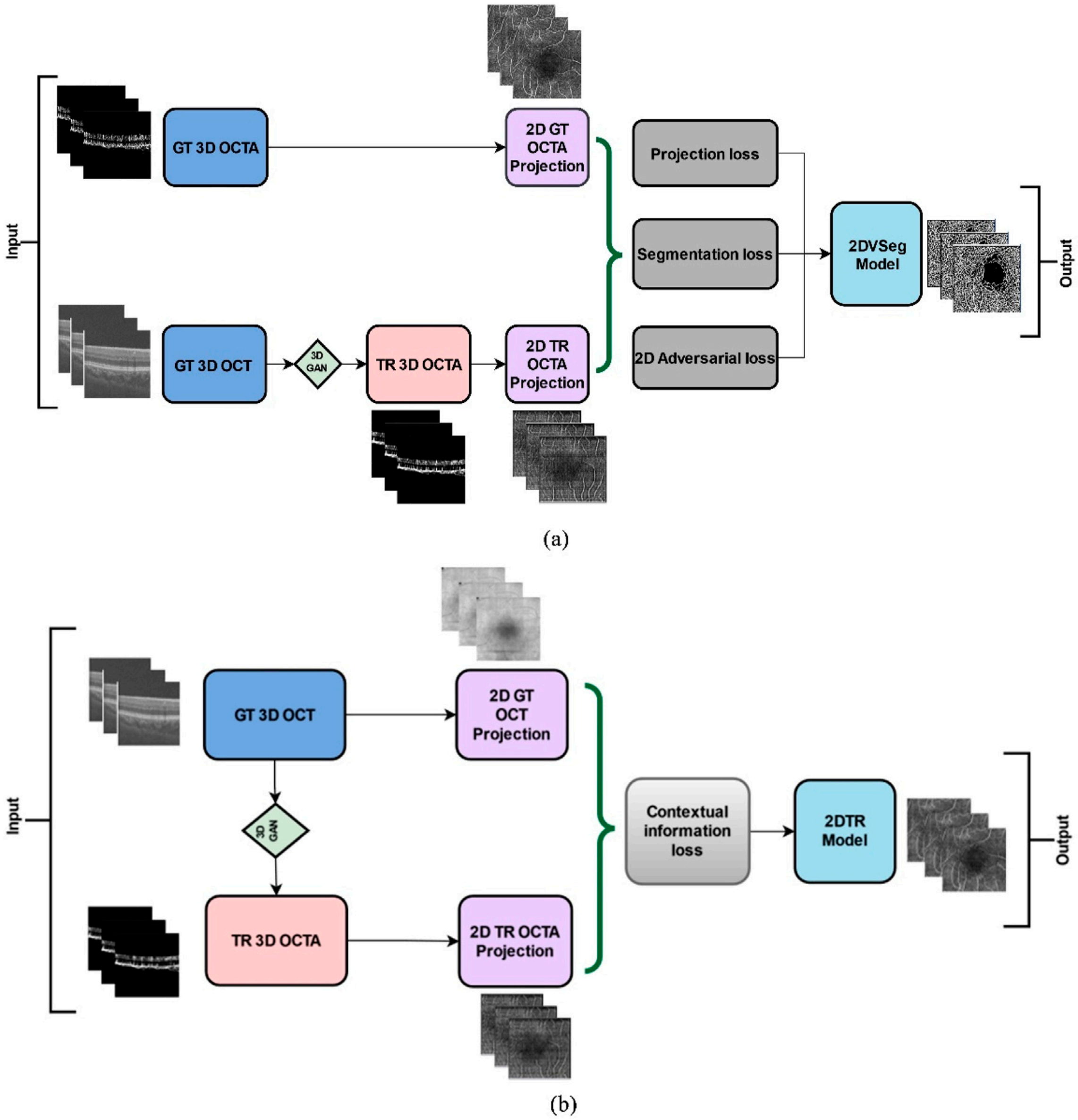

FIGURE 2
(A) 2D vascular segmentation model, **(B)** 2D Translation model.

(CNV) patients, 29 DR and 160 Normal patients who are compared statistically after evaluating the feature values. The 3 mm set contains paired OCT and OCTA volumes from 200 patients with a field of view (FOV) 3 mm × 2 mm × 3 mm. Each volume has 304 slices with a size of 640px × 304px. The generated projection map is of 256px × 256px size. The whole dataset is divided into a 70-25-5% split: 140, 10, and 50 volumes for training, validation and test sets respectively. Similarly, the 6 mm set contains paired OCT and OCTA volumes from 300 patients with FOV of 6 mm × 2 mm × 6 mm. Each volume is of size 640px × 400px, containing 400 slices and generated projection maps are of size 256px × 256px. Similar to 3 mm set: 180, 20, and 100 volumes are split as training, validation and test sets. The 6 mm dataset contains 43 AMD, 11 CNV, 14 Central serous chorioretinopathy (CSC), 35 DR, 10 Retinal vein occlusion (RVO), 91 Normal and 96 other retinal pathology-affected patients for which a similar statistical evaluation is carried out and feature values are calculated.

UIC data and image acquisition

The UIC study was approved by the institutional review board of the University of Illinois at Chicago and was in

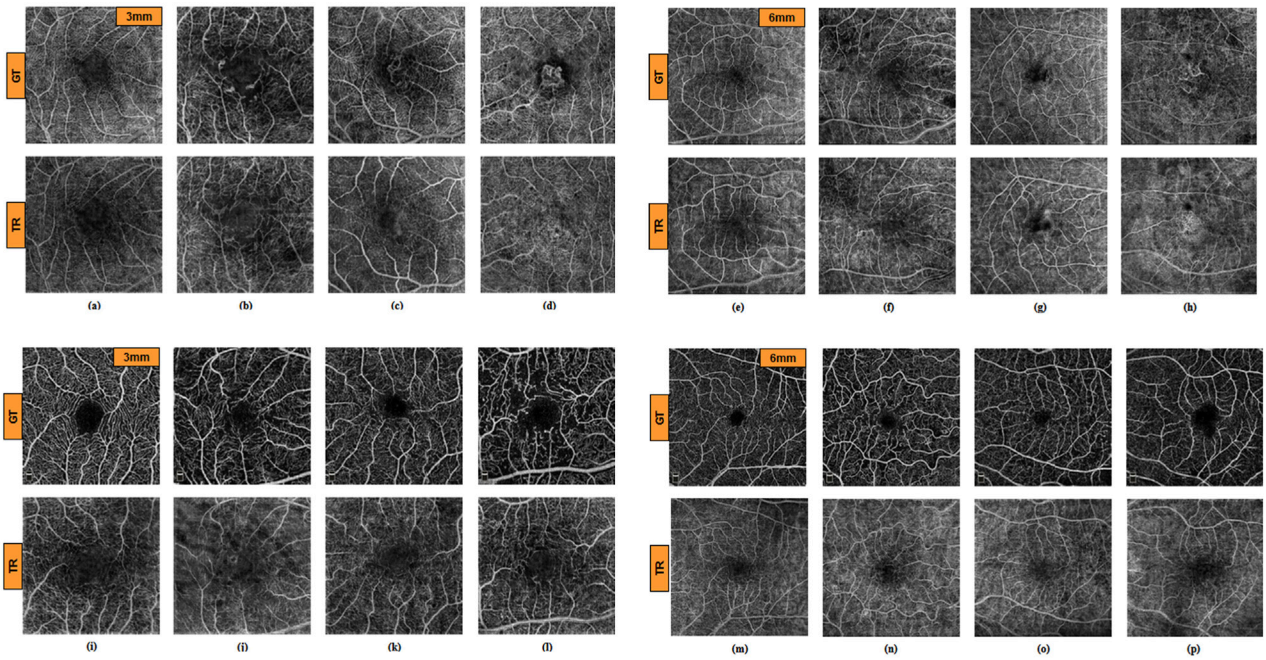

FIGURE 3
GT and TR-OCTA images for NORMAL **(A, E)**, DR **(B, F)**, CNV **(C, G)** and AMD **(D, H)** patients from OCT500. **(A–D)** images are of 3 mm and **(E–H)** are of 6 mm. Similarly **(I–P)** are OCTA images from UIC dataset. **(I, M)** from Control, **(J, N)** from Mild, **(K, O)** from Moderate and **(L, P)** from Severe group for 3 mm and 6 mm respectively.

compliance with the ethical standards stated in the Declaration of Helsinki. The patients with DR were recruited from UIC Retinal Clinic. We performed a retrospective study of consecutive diabetic patients (Type II) who underwent OCTA and OCT imaging. The patients are thus representative of a university population of diabetic patients who require imaging for management of diabetic macular edema and DR. OCT/OCTA images of both eyes of every patient were collected. We excluded subjects with macular edema, previous vitreous surgery, and history of other eye diseases. All patients had undergone a complete anterior and dilated posterior segment examination (J.I.L.). The patients were classified by severity of DR (mild, moderate, and severe) according to the Early Treatment Diabetic Retinopathy Study staging system. The grading was done by retina specialist who used a slit-lamp fundus lens for the diagnosis. OCT/OCTA data were acquired using an ANGIOVUE spectral domain OCTA system (Optovue, Fremont, CA), with a 70-kHz A-scan rate, an axial an axial resolution of 5 μm, and a lateral resolution of 15 μm. All the OCTA images were macular scans and had field of view of 6 mm. We exported the OCTA images from the software ReVue (Optovue) and used custom-developed software in Python OpenCV for further image analysis, feature extraction, and image classification.

The UIC dataset contains 445 OCT scans from 41 patients with different DR conditions: control, mild, moderate and severe. The scans were selected based on signal strength Q ≥ 5 for this study. Similar to OCT500, this dataset has both 3 mm (187 scans) and 6 mm (258 scans) scans for different stages of DR: Control, Mild, Moderate and Severe. For 3 mm FOV, we used 35 scans for Control group, 118 for Mild, 37 for Moderate and 97 for Severe. On the other hand, for 6 mm, the set included 59 for Control, 143 Mild, 69 Moderate and 123 Severe scans for comparison. 3 mm slices are of size 640px × 304px and 6 mm slices are mostly of 640px × 400px with some mixed 640px × 304px scans which are used to generate 256px × 256px OCTA slices. Some patients were listed in multiple categories therefore, scans of those patients were included in multiple categories before feature evaluation.

Comparative analysis of similarity and OCTA features

The algorithm for TR-OCTA generation was exclusively trained only on OCT500 and tested on the UIC dataset for feature quantification and comparison. Figures 3A–H depicts GT-OCTA and generated TR-OCTA images at 3 mm and 6 mm scan range from diseased as well as normal patients for

TABLE 1 Two-tail t-test between GT-OCTA and TR-OCTA for OCT500 and UIC datasets.

Quantitative Features	OCT500 3 mm ($p < .05$)	OCT500 6 mm ($p < .05$)	UIC 3 mm ($p < .05$)	UIC 6 mm ($p < .05$)
BVD	0.48	0.58	$1.7\ e^{-31}$	$4.91\ e^{-15}$
BVC	0.45	$1.35\ e^{-52}$	$7.14\ e^{-115}$	$1.5\ e^{-106}$
BVT	$1.1\ e^{-7}$	0.006	$1.54\ e^{-41}$	$6.76\ e^{-14}$
VPI	$1.36\ e^{-22}$	$8.26\ e^{-31}$	$3.89\ e^{-5}$	.040

TABLE 2 SSIM values for 3 mm and 6 mm from both OCT500 and UIC.

SSIM (OCT500)	Complete	AMD	CNV	DR	NORMAL	CSC	RVO	Others
3 mm	0.4835 (0.29–0.60)	0.4513 (0.29–0.55)	0.4754 (0.44–0.52)	0.4923 (0.29–0.59)	0.4834 (0.34–.60)	-	-	-
6 mm	0.4175 (0.16–0.52)	0.4102 (0.30–0.50)	0.4224 (0.38–0.45)	0.4329 (0.35–0.52)	0.4212 (0.25–0.49)	0.4140 (0.32–0.45)	0.3664 (0.26–0.43)	0.4169 (0.16–0.51)

SSIM (UIC)	Complete	Control	Mild	Moderate	Severe
3 mm	0.2808 (0.13–0.39)	0.3188 (0.21–0.38)	0.2961 (0.14–0.35)	0.2914 (0.13–0.39)	0.2647 (0.13–0.39)
6 mm	0.2952 (0.12–0.38)	0.2820 (0.12–0.36)	0.2966 (0.19–0.37)	0.2920 (0.12–0.38)	0.2679 (0.12–0.37)

TABLE 3 FID and PCQI scores for the complete datasets of OCT500 and UIC.

OCTA dataset (OCT500)	FID	PCQI (mean, SD)
3 mm	35.88	0.99795 (0.000457)
6 mm	49.06	0.99778 (0.000539)
OCTA Dataset (UIC)	**FID**	**PCQI (Mean, SD)**
3 mm	150.34	0.99546 (0.000737)
6 mm	107.74	0.99555 (0.000606)

OCT500 while Figures 3I–P represent the images for UIC dataset across various patient categories.

OCT500 3 mm dataset has AMD (6), CNV (5), DR (29) and NORMAL (160) patients totalling 200 patients, while 6 mm dataset includes AMD (43), CNV (11), CSC (14), DR (35), RVO (10), OTHER retinopathies (96) and NORMAL (91) patients totalling 300. Two-tail T-tests were carried out ($p < 0.05$) between GT and TR-OCTAs for BVD, BVC, BVT and VPI (3 mm complete dataset). The results indicate that BVD and BVC have p-values close to 0.5, suggesting that there is no significant difference between these features in the GT and TR-OCTA values (Table 1). This means that these features can be used for effective disease classification. Upon evaluating quality metrics for the datasets (Tables 2, 3), mean SSIM for 3 mm was found to be slightly higher (0.48) than 6 mm dataset showing SSIM ranging from 0.16–0.52 with a mean of 0.42. SSIM values were also calculated for different patient statuses in both datasets. For the 3 mm dataset: AMD patients show a slightly lower mean SSIM, DR dataset on the other hand reveals a higher mean SSIM compared to other patient groups. However, for 6 mm: AMD, CNV, CSC, patients with other retinopathies and Normal group showed a close SSIM mean value except for DR patients with a slightly higher mean SSIM (0.43) and RVO patients, a lower mean SSIM of 0.36 (Table 2). Furthermore, The FID score for the 3 mm dataset was lower (35.88) compared to the 6 mm dataset, which had a higher FID score of 49.06. On the other hand, PCQI scores were comparably high for both datasets with the 3 mm set slightly outperforming the 6 mm (Table 3). All these feature values were also calculated for the complete dataset and separately for different diseased and normal patients for comparative analysis (Table 4). BVD and BVT values from 3 mm show some trend among Normal and AMD, CNV, DR groups which is mimicked by the TR-OCTA (Figures 4A–D). Overall, TR-BVC, TR-VPI, TR-BVT, and TR-BVD values (Figure 5) are concentrated within a specific range and closer to the GT values for each feature respectively. For BVD, some outliers are further away from the lowest value of the BVD range which is consistent with the findings from the categorized distribution of feature values (Supplementary Figures S1A–D).

Similarly, for the complete 6 mm dataset we performed T-tests ($p < .05$) for BVD, BVC, VPI and BVT but only BVD was found to have statistically similar values for both TR-OCTA and GT-OCTA images (Table 1). The 6 mm dataset contained

TABLE 4 Statistical analysis of TR-OCTA compared to GT-OCTA for 3 mm dataset from OCT500.

OCTA Dataset	Dataset (no. Of patients)	BVD (mean, SD)	BVC (mean, SD)	BVT (mean, SD)	VPI (mean, SD)
TR-OCTA	Complete (200)	212.31 (29.93)	22.80 (0.81)	1.086 (0.006)	26.91 (5.47)
GT-OCTA		210.22 (29.04)	22.75 (0.41)	1.089 (0.006)	31.43 (2.35)
TR-OCTA	AMD (6)	213.73 (20.05)	22.45 (1.03)	1.087 (0.009)	29.24 (1.91)
GT-OCTA		205.46 (26.45)	22.91 (0.39)	1.09 (0.003)	29.69 (1.63)
TR-OCTA	CNV (5)	228.53 (22.36)	22.34 (1.04)	1.087 (0.003)	26.36 (3.7)
GT-OCTA		224.22 (16.47)	22.90 (0.53)	1.089 (0.005)	30.26 (2.55)
TR-OCTA	DR (29)	209.07 (27.51)	23.12 (0.71)	1.080 (0.007)	26.92 (4.32)
GT-OCTA		210.80 (34.82)	23.14 (0.42)	1.087 (0.005)	28.25 (3.55)
TR-OCTA	NORMAL (160)	212.34 (30.86)	22.77 (0.81)	1.086 (0.006)	26.84 (5.79)
GT-OCTA		209.86 (28.39)	22.67 (0.37)	1.089 (0.006)	32.11 (1.41)

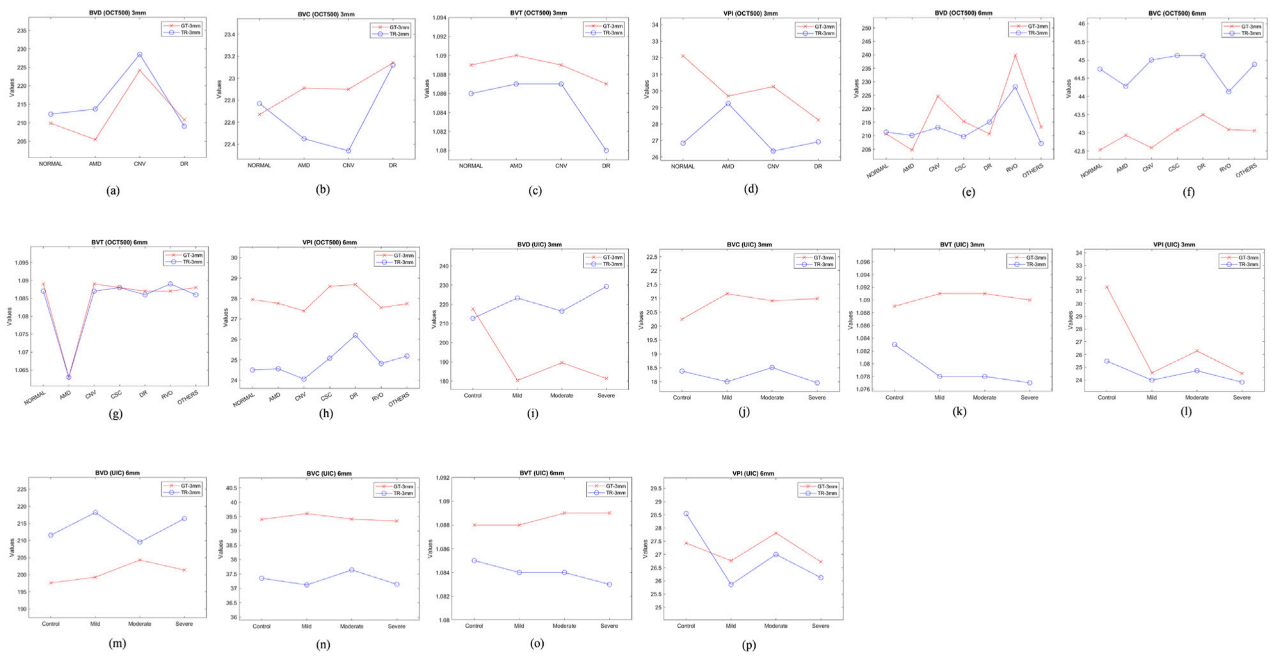

FIGURE 4
Feature values for different patient groups from both OCT500 and UIC. **(A–D)** show feature trend of 3 mm for OCT500, **(E–H)** for OCT500 6 mm, **(I–L)** UIC 3 mm and **(M–P)** UIC 6 mm dataset.

central serous chorioretinopathy (CSC), retinal vein occlusion (RVO) and other retinal pathologies that were absent in the 3 mm dataset (Figures 4E–H). In a comparative analysis (Table 5), BVD for RVO and BVT for AMD patients shows a larger deviation compared to other cases when calculated. Also, BVD and BVT values for translated image follow the trend set by the GT-OCTA. However, BVC, BVT, and VPI were measured having closer values in all cases. When plotted, the distribution of the feature values for TR-OCTA and GT-OCTA, similar to the 3 mm dataset, BVC, VPI and BVD show more outliers compared to BVT and the distribution is similar to the 3 mm dataset. Supplementary Figures S1E–K exhibits feature value distribution for AMD, CNV, CSC, DR, RVO, other retinal pathologies and normal patients and a similar

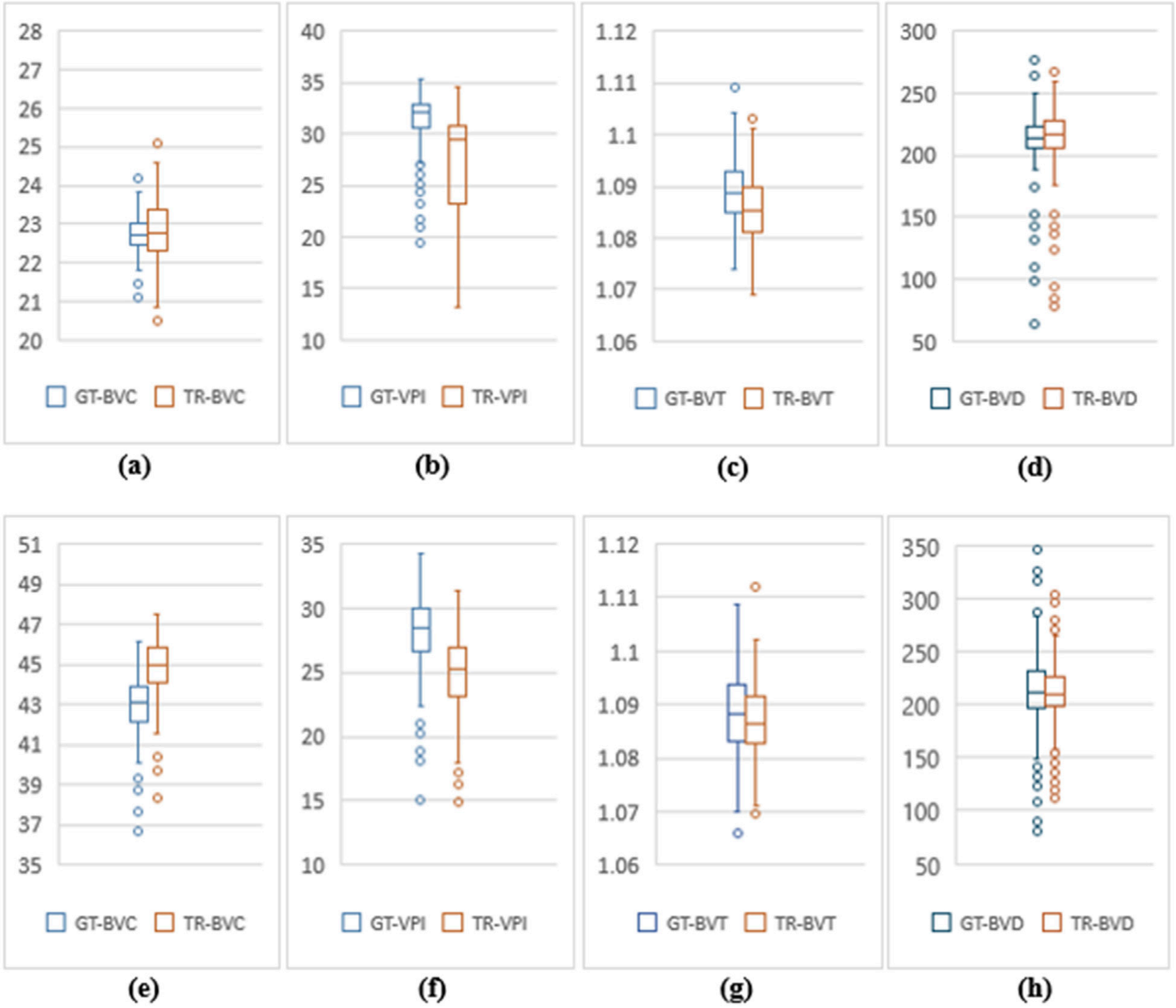

FIGURE 5
Feature value distribution of 3 mm and 6 mm scans for OCT500. **(A–D)** are BVC, VPI, BVT and BVD values for 3 mm. Similarly, **(E–H)** show values for 6 mm.

trend of BVD feature having more outliers is observed for diseased as well as normal patients in comparison to other features except RVO.

For UIC dataset Table 2, 3 summarize the qualitative metrics and Tables 6, 7 summarize quantitative feature values for both 3 mm and 6 mm presenting the validity of implementation of automated image-to-image translation. The whole 3 mm dataset show a mean SSIM value of 0.2808 however Control group as well as other DR stages show slight deviation in terms of mean SSIM although their value range stays similar. For the complete 6 mm, SSIM was slightly higher (0.2952) and contrary to the 3 mm set, Control, Mild and Moderate groups show closer values to each other except for Severe with a slight decrease in value: 0.2679. As a quality metrics, FID scores show higher value than OCT500 for both 3 mm and 6 mm: 150.34 and 107.74 respectively however PCQI scores were closer to the ideal value for both 3 mm and 6 mm.

From two-tail T-tests ($p < .05$) BVD, BVC, BVT and VPI values for TR-OCTA were found to be statistically different from GT-OCTA for 3 mm and 6 mm which is expected due to the fact that UIC data was excluded from the training (Table 1). These feature values were calculated (3 mm and 6 mm) for the complete dataset as well as separately for different patient groups. For 3 mm (Table 6), BVD (Figures 4I–L) shows more deviation from the GT values compared to BVC and VPI except BVT which shows better comparative values. From Figure 6 we can observe the difference between TR and GT images and concentrated values with some outliers for BVC, BVT, and BVD.

TABLE 5 Statistical analysis of TR-OCTA compared to GT-OCTA for 6 mm dataset from OCT500.

OCTA dataset	Dataset (no. Of patients)	BVD (Mean ± St.d)	BVC (Mean ± St.d)	BVT (Mean ± St.d)	VPI (Mean ± St.d)
TR-OCTA	Complete (300)	210.80 ± 30.45	44.78 ± 1.37	1.087 ± 0.006	24.95 ± 2.97
GT-OCTA		212.34 ± 37	42.91 ± 1.33	1.088 ± 0.007	27.94 ± 3.02
TR-OCTA	AMD (43)	210.13 ± 32.07	44.28 ± 1.28	1.063 ± 0.005	24.56 ± 3.32
GT-OCTA		204.72 ± 35.76	42.93 ± 1.44	1.063 ± 0.007	27.76 ± 3.65
TR-OCTA	CNV (11)	213.11 ± 27.01	45.00 ± 1.03	1.087 ± 0.003	24.06 ± 1.63
GT-OCTA		224.63 ± 46.59	42.59 ± 1.03	1.089 ± 0.007	27.39 ± 3.36
TR-OCTA	CSC (14)	209.66 ± 22.43	45.12 ± 0.96	1.088 ± 0.0064	25.08 ± 1.86
GT-OCTA		215.35 ± 45.51	43.08 ± 0.98	1.088 ± 0.0063	28.59 ± 2.24
TR-OCTA	DR (35)	215.09 ± 28.04	45.12 ± 1.30	1.086 ± 0.0065	26.2 ± 2.95
GT-OCTA		210.66 ± 37.54	43.50 ± 1.18	1.087 ± 0.0068	28.68 ± 3.2
TR-OCTA	RVO (10)	228.13 ± 60.63	44.13 ± 1.15	1.089 ± 0.0079	24.82 ± 1.76
GT-OCTA		239.79 ± 26.76	43.09 ± 0.91	1.087 ± 0.009	27.55 ± 2.89
TR-OCTA	Others (96)	207.14 ± 30.19	44.88 ± 1.34	1.086 ± 0.0062	25.19 ± 3.06
GT-OCTA		213.22 ± 32.52	43.06 ± 1.19	1.088 ± 0.0073	27.74 ± 2.61
TR-OCTA	Normal (91)	211.34 ± 27.64	44.75 ± 1.50	1.087 ± 0.0072	24.5 ± 2.97
GT-OCTA		210.71 ± 39.42	42.53 ± 1.51	1.089 ± 0.0073	27.95 ± 3.13

TABLE 6 Statistical analysis of TR-OCTA compared to GT-OCTA for 3 mm dataset from UIC.

OCTA Dataset	Dataset (no. Of scans)	BVD (Mean ± St.d)	BVC (Mean ± St.d)	BVT (Mean ± St.d)	VPI (Mean ± St.d)
TR-OCTA	Complete (187)	220.91 ± 21.73	18.21 ± 0.86	1.078 ± 0.0066	24.52 ± 2.70
GT-OCTA		189.29 ± 25.59	20.95 ± 0.65	1.090 ± 0.0086	26.11 ± 4.45
TR-OCTA	Control (35)	212.69 ± 17.66	18.38 ± 0.80	1.083 ± 0.0082	25.48 ± 1.90
GT-OCTA		217.57 ± 27.82	20.25 ± 0.48	1.089 ± 0.0073	31.30 ± 4.53
TR-OCTA	Mild (118)	223.29 ± 22.97	18.00 ± 0.86	1.078 ± 0.0056	23.99 ± 2.76
GT-OCTA		180.42 ± 19.80	21.17 ± 0.58	1.091 ± 0.0088	24.56 ± 3.47
TR-OCTA	Moderate (37)	216.40 ± 24.49	18.51 ± 0.97	1.078 ± 0.0065	24.73 ± 2.45
GT-OCTA		189.60 ± 20.77	20.91 ± 0.47	1.091 ± 0.0102	26.29 ± 3.25
TR-OCTA	Severe (97)	229.30 ± 18.85	17.96 ± 0.95	1.077 ± 0.0061	23.83 ± 2.76
GT-OCTA		181.44 ± 20.79	20.99 ± 0.50	1.090 ± 0.0087	24.51 ± 3.57

Supplementary Figures S2A–D shows the range of values for all the features observed in different DR groups and the mean values for TR-OCTA lies below the GT-OCTA most of the cases except for BVD which lies above GT values for Mild, Moderate and Severe group.

A similar pattern is recognized from the 6 mm analysis (Table 7) having BVD a higher deviation from the GT compared to BVC, BVT, and VPI. BVD shows more outliers for TR-OCTA than other features contributing to the larger difference (Figure 6). All these feature values are calculated separately for Control, Mild, Moderate and Severe groups and in general BVD shows higher difference between TR-OCTA and GT-OCTA among all the features for different patient groups (Figures 4M–P). Supplementary Figures S2E–H represents

TABLE 7 Statistical analysis of TR-OCTA compared to GT-OCTA for 6 mm dataset from UIC.

OCTA Dataset	Dataset (no. Of scans)	BVD (Mean ± St.d)	BVC (Mean ± St.d)	BVT (Mean ± St.d)	VPI (Mean ± St.d)
TR-OCTA	Complete (258)	214.75 ± 25.5	37.30 ± 0.93	1.084 ± 0.0059	25.66 ± 2.86
GT-OCTA		199.76 ± 15.05	39.54 ± 0.87	1.089 ± 0.0069	27.14 ± 2.46
TR-OCTA	Control (59)	211.57 ± 21.79	37.35 ± 0.72	1.085 ± 0.0064	28.55 ± 2.19
GT-OCTA		197.61 ± 12.83	39.40 ± 0.74	1.088 ± 0.0062	27.43 ± 2.027
TR-OCTA	Mild (143)	218.19 ± 22.93	37.12 ± 1.067	1.084 ± 0.0056	25.86 ± 2.74
GT-OCTA		199.29 ± 14.16	39.60 ± 0.80	1.088 ± 0.0070	26.76 ± 2.30
TR-OCTA	Moderate (69)	209.54 ± 29.57	37.64 ± 0.83	1.084 ± 0.0060	27.00 ± 2.42
GT-OCTA		204.29 ± 14.62	39.41 ± 0.93	1.089 ± 0.0072	27.81 ± 2.31
TR-OCTA	Severe (123)	216.41 ± 25.25	37.14 ± 0.81	1.083 ± 0.0057	26.12 ± 2.44
GT-OCTA		201.34 ± 14.96	39.34 ± 0.84	1.089 ± 0.0072	26.72 ± 2.52

feature value distribution with outliers for different DR groups. Similar to 3 mm, TR-OCTA BVD feature value distribution shows a mean higher than the GT-OCTA for Control, Mild, Moderate and Severe groups.

Discussion

In this paper, we implemented a recently demonstrated algorithm [36] for OCT-OCTA translation and validated the translated OCTA images to show their utility in quantitatively characterizing retinal features using two datasets OCT500 and UIC. We present a comprehensive analysis comparing the performance of GT- OCTA images with those generated by a TR-OCTA across different patient groups, including those with complete data sets, for both 3 mm and 6 mm FoV. Several qualitative (SSIM, FID, PCQI) and quantitative metrics (BVD, BVC, BVT, and VPI) were considered to validate the comparative performance analysis on a clinical dataset from UIC. We found FID and PCQI scores to be the most reliable qualitative metrics and a combination of BVT, VPI could be considered best for distinguishing diseases specially DR patients in TR-OCTA.

SSIM was utilized as a quality metric to assess the similarity between TR-OCTA and GT-OCTA images, providing insight into the translation model's ability to replicate key structural features of the retinal vasculature. For OCT500, between 3 mm and 6 mm, mean SSIM from the complete dataset of 3 mm was higher than 6 mm despite both values were far from the ideal value. The reason behind is how the translation algorithm works that focuses on the vasculature rather than the entire image while SSIM considers pixel difference between the reference and the target image for its entirety. This becomes more prominent from the UIC dataset. Both 3 mm and 6 mm sets form UIC shows lower mean SSIM than OCT500 since the algorithm was exclusively trained on OCT500 and as a result the generated TR-OCTAs show less structural similarity overall to the GT-OCTA. SSIM for different patient groups was also considered to measure the response of the TR-OCTAs for different pathologies. UIC dataset mostly show consistent mean SSIM across different pathologies except for RVO (6 mm) indicating the algorithm couldn't capture the vascular structure from the RVO patient equally as other pathologies which could also be contributed to the lower number of sample available for training (3.34%). Similar observations can be made from UIC 3 mm and 6 mm however the model fails to capture the key structural features of severe stage DR patients. Therefore, from our observations, SSIM is not an ideal metric for GAN generated OCTA images.

Two more quality metrics, FID and PCQI scores were considered as these are more suitable for GAN generated image quality comparison against reference (GT) images. OCT500 3 mm set, having lower FID score, indicate higher similarity to the reference data, suggesting that the 3 mm scans exhibit better image quality compared to the 6 mm scans within this dataset. This trend is consistent with expectations, as higher resolution (smaller scanning area) typically results in finer detail and less distortion. The UIC dataset shows comparatively higher FID scores for both 3 mm and 6 mm scans, indicating lower fidelity compared to the OCT500 dataset which can be explained as the effect of implementing the model to a dataset excluded from the training. Interestingly, the 6 mm scans have a lower FID score than the 3 mm scans, suggesting better relative performance at a larger scanning area for this dataset. This inverse trend can be attributed to variations in image quality for 6 mm image acquisition (image collected after a certain date is of higher quality than the previous scans). Another quality metric, PCQI values for the OCT500 dataset are found to be exceptionally high for both 3 mm and 6 mm. These results

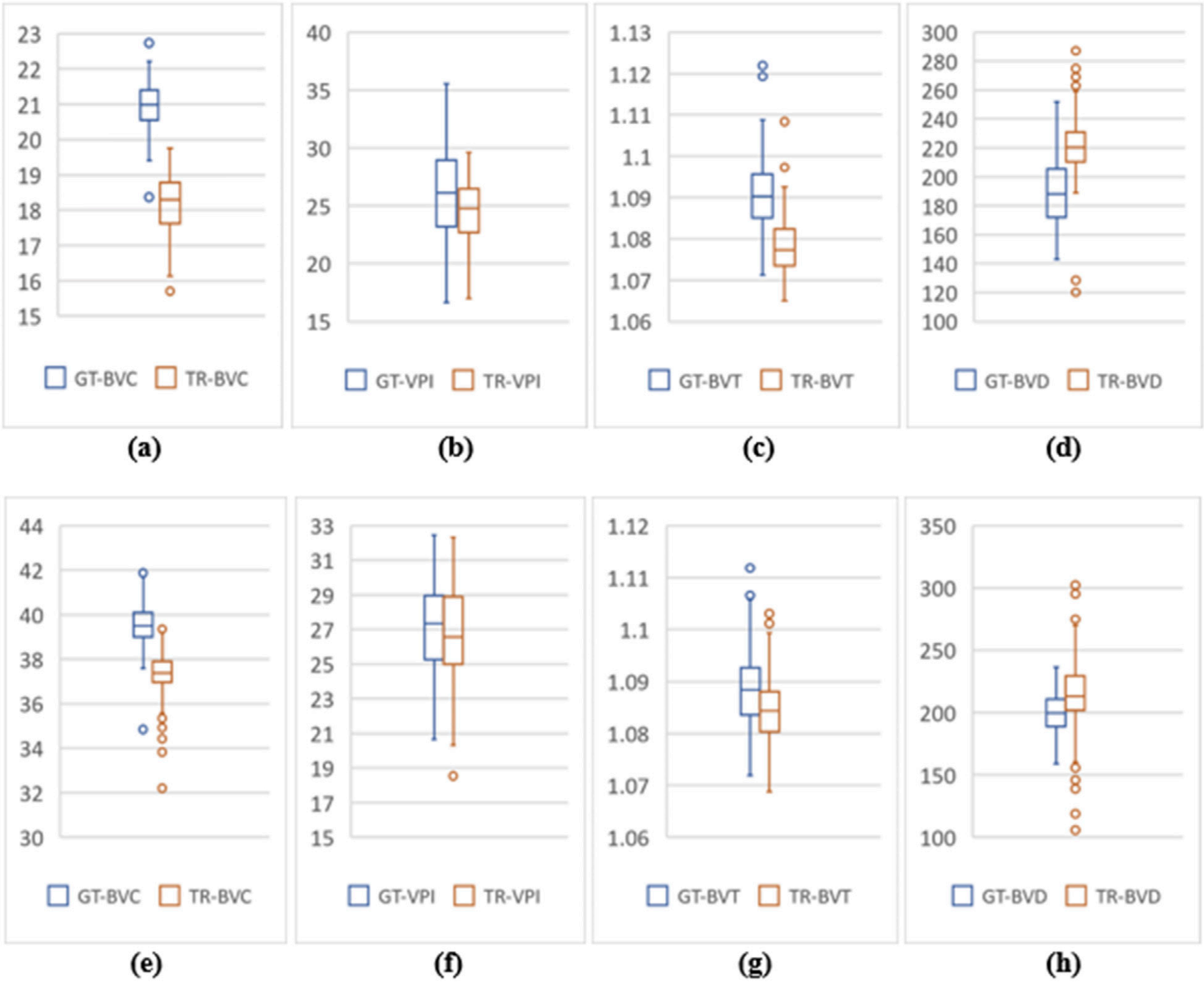

FIGURE 6
Feature value distribution of 3mm and 6 mm scans for the UIC dataset. **(A–D)** are BVC, VPI, BVT, and BVD values for 3 mm. Similarly, **(E–H)** show values for 6 mm scans.

indicate minimal variation and high consistency in image quality across different scans. The slight decrease in PCQI for the 6 mm scans is consistent with the increased FID score, further confirming that the 3 mm scans offer superior quality. The PCQI scores for the UIC dataset, while slightly lower than those of the OCT500 dataset, still demonstrate high image quality, for 3 mm and 6 mm sets. The minimal difference in PCQI between 3 mm and 6 mm scans suggests that the image quality is relatively stable across different FoVs, despite the higher FID scores.

To compare the quantitative feature values between TR-OCTA and GT-OCTA, we focus on the performance across different categories since neither OCT500 nor UIC has equal distribution of data across different pathologies and normal or control group. In a comparative analysis from OCT500, BVD shows more deviation from the GT-OCTA, specially for 6 mm, supporting the better FID and PCQI scores for 3 mm, indicating the model can capture the superficial layer vasculature better than the deep layer hence vessel density shows bigger difference between TR-OCTA and GT-OCTA (Tables 4, 5). This feature also has the greatest number of outliers (Figure 5) among all features contributing to larger difference. Similar observations can be made from UIC dataset, showing the models limitation in capturing vasculature from all layers equally. When plotted, the trend set by the GT-OCTA for BVD show higher deviation for CNV in OCT500 3 mm. TR-OCTA also follows the same trend, however, for OCT500 6mm, BVD feature values tend to follow the GT-OCTA apart from RVO patients. On the other hand, for UIC 3 mm and 6 mm, BVD fails to properly exhibit the trend shown by GT-OCTA indicating inclusion of the data in the training process provides better result for BVD (Tables 6, 7). However, for UIC 6mm, BVD shows clear distinction between control and early stage DR as well as severe stage DR, similar to what has been reported in other studies [12]. Overall, when trained, BVD could be considered as a potential biomarker for CNV and RVO patients as evident from the analysis (Figure 4).

BVC, another quantitative feature, unlike BVD, doesn't show that large of a deviation from the GT values across different pathologies indicating it could be used as a measure of performance even on a dataset not seen before. OCT500 3 mm TR-OCTA tend to show some variations for CNV and RVO patient similar to BVD however the trend goes beyond what is observed from GT-OCTA. From UIC dataset, however, BVC feature values across different pathologies stay in close range across different stages of DR patients without showing any large deviation. However, the TR-OCTA values follow GT-OCTA trend.

BVT feature values show least deviation for all datasets across different patient categories. For OCT500 3 mm, TR-OCTA values follow the trend set by GT-OCTA specially showing a clear distinction among DR and other pathologies as well as normal state (Figure 4C). In consistent with this scenario, UIC BVT feature values stay in close range for (TR-OCTA and GT-OCTA) 3 mm and show a better trend line for 6 mm. From OCT500 6 mm, BVT feature values, while closely following GT-OCTA values, show clear distinction for AMD patients indicating a potential choice for AMD classification at lower FoV.

Finally, VPI feature values for OCT500 3 mm TR-OCTA show an opposite trend compared to GT-OCTA. GT-OCTA show clear distinction among AMD, CNV and DR pathologies however TR-OCTA fails to identify the distinction. However, OCT500 6 mm TR-OCTA shows a much better performance showing the clear deviation of values for CNV, CSC and DR patients indicating the model's ability to distinguish between normal and AMD, CNV, DR patients in general. A similar picture is depicted by the performance analysis on UIC dataset, specially 3 mm, clearly identifying different DR stages from control groups indicating VPI as a better choice of potential biomarker for DR patients.

Overall, in light of the comparative analysis performed on both datasets, SSIM values were higher for OCT500 rather than UIC indicating the inclusion of the prior dataset affecting the quality of the generated images. Similar scenarios can be observed from FID scores, OCT500 having lower value hence better resemblance to the GT-OCTA images. However, PCQI scores for both datasets (OCT500 and UIC) indicates the TR-OCTA images are almost the same as the GT-OCTAs in terms of contrast and sharpness which is supported by our analysis that some features (BVT, VPI) show better performance across both FoV. Although, feature values for BVC and VPI showed slight variation, they were still in close proximity for both OCT500 and UIC. BVT, however, is found having almost consistent values for both dataset in all cases. BVD, on the other hand, shows bigger variation between TR-OCTA and GT-OCTA for UIC compared to OCT500, an expected outcome similar to SSIM, as density features tend to be affected by local vasculature more than the vessel features.

Despite a better performance from the TR-OCTA across the datasets, our study has some inherent limitations. One limitation being the scarcity of the publicly available data, restricting the ability to perform extensive and varied analyses. Additionally, the dataset used in this research is relatively small, particularly when considering cross-pathological studies. This limited sample size can hinder the generalizability of the findings. Furthermore, our data distribution is unequal across different patient categories and pathologies, potentially introducing bias and affecting the robustness of our conclusions. Another significant challenge is the inconsistency in image quality and signal strength. Not all OCTA images have the same signal strength or quality, which can adversely impact the performance of translated OCTA in both quantitative and qualitative assessments. These limitations highlight the need for more comprehensive datasets and improved image acquisition standards to enhance the reliability and applicability of OCTA feature studies. Although similar studies have been conducted [12, 14] on OCTA features, to our knowledge, this is the first study conducted on quantitative characterization and extensive comparative analysis of retinal features for TR-OCTA images. We tried to establish the idea that while the translation model holds promise in reproducing retinal vasculature across various conditions, there exist minor variations in the accuracy of vascular metrics between TR-OCTA and GT-OCTA images. These discrepancies underscore the necessity for ongoing enhancements to the translation model to achieve higher precision in vascular representation, particularly for pathological conditions where accurate vascular depiction is critical for clinical diagnosis and monitoring.

This study showcases the potential of AI to bridge the gap between OCT's inability to visualize blood flow information and leveraging generative-adversarial learning frameworks for image translation to capture that information. Our findings suggest that AI-driven translation models can generate high-quality OCTA images from OCT data (demonstrated using SSIM, FID and PCQI metrics) and the quantitative features generated in TR-OCTA follow a similar trend as in GT-OCTA. This has the potential to significantly improve the accuracy and efficiency of diagnosing and monitoring retinal diseases through OCTA imaging, emphasizing the need for further research and development in this area.

In summary, this study demonstrates the potential of generative AI in enhancing OCT imaging for ophthalmic diagnostics. By validating quantitative features to check the viability of TR-OCTA, this research addresses significant limitations in widespread adoption of OCTA in clinical settings. Despite facing challenges such as generalization for different retinal diseases and difficulty in capturing detailed vascular networks, our study lays a solid foundation for future advancements in multi-modal OCT based retinal disease diagnosis and monitoring. The incorporation of AI not only promises to reduce the dependence on costly OCTA devices but also opens new avenues for accessible and accurate retinal healthcare solutions. Moving forward, it is imperative to refine these AI models to improve the resolution and accuracy of translated OCTA images, ensuring they can reliably support clinical decision-making and contribute to the broader understanding of retinal pathologies.

Author contributions

All authors participated in the interpretation of the studies, analysis of the data and review of the manuscript; RB: conceptualization, data curation, formal analysis, investigation, methodology, project administration, resources, software, supervision, validation, visualization, writing–original draft, and writing–review and editing, AT, JL, and TL: resources, result interpretation, and writing–review and editing, MA: conceptualization, data curation, formal analysis, funding acquisition, investigation, methodology, project administration, resources, software, supervision, validation, visualization, writing–original draft, and writing–review and editing. All authors contributed to the article and approved the submitted version.

Data availability

Publicly available datasets were analyzed in this study. The OCT500 dataset can be found here: https://ieee-dataport.org/open-access/octa-500. UIC data can be requested to the corresponding author.

Funding

The author(s) declare that financial support was received for the research, authorship, and/or publication of this article. Supported by NEI R21EY035271 (MA), R15EY035804 (MA); and UNC Charlotte Faculty Research Grant (MA).

Conflict of interest

The author(s) declared no potential conflicts of interest with respect to the research, authorship, and/or publication of this article.

Supplementary material

The Supplementary Material for this article can be found online at: https://www.ebm-journal.org/articles/10.3389/ebm.2024.10333/full#supplementary-material

SUPPLEMENTARY FIGURE S1
(A–D) show BVC, VPI, BVT, and BVD feature values for the 3 mm dataset (OCT500) with different patient conditions. a(i-iv) are AMD patients, b(i-iv) are CNV patients, c(i-iv) are DR patients. d(i-iv) are Normal patients. **(E–K)** show feature values for the 6 mm dataset (OCT500) with different patient conditions. e(i-iv) are AMD patients, f(i-iv) are CNV patients, g(i-iv) are CSC patients, h(i-iv) are DR patients, i(i-iv) are RVO patients, j(i-iv) are patients with other retinal pathologies, k(i-iv) are Normal patients.

SUPPLEMENTARY FIGURE S2
(A–D) show BVC, VPI, BVT and BVD for the UIC 3 mm scans with different patient conditions. a(i-iv) shows Control group, b(i-iv) Mild, c(i-iv) Moderate, d(i-iv) Severe patient scans. Similarly, **(E–H)** show BVC, VPI, BVT and BVD for the UIC 6 mm scans with different patient conditions. e(i-iv) for Control group, f(i-iv) for Mild, g(i-iv) for Moderate, h(i-iv) for Severe patient scans.

References

1. Bowd C, Zangwill LM, Berry CC, Blumenthal EZ, Vasile C, Sanchez-Galeana C, et al. Detecting early glaucoma by assessment of retinal nerve fiber layer thickness and visual function. *Invest Ophthalmol Vis Sci* (2001) **42**(9):1993–2003.

2. Fujimoto J, Swanson E. The development, commercialization, and impact of optical coherence tomography. *Invest Ophthalmol Vis Sci* (2016) **57**(9): OCT1–OCT13. doi:10.1167/iovs.16-19963

3. Spaide RF, Fujimoto JG, Waheed NK, Sadda SR, Staurenghi G. Optical coherence tomography angiography. *Prog Retin Eye Res* (2018) **64**:1–55. doi:10.1016/j.preteyeres.2017.11.003

4. Yang D, Ran AR, Nguyen TX, Lin TPH, Chen H, Lai TYY, et al. Deep learning in optical coherence tomography angiography: current progress, challenges, and future directions. *Diagnostics* (2023) **13**(2):326. doi:10.3390/diagnostics13020326

5. Huang D, Swanson EA, Lin CP, Schuman JS, Stinson WG, Chang W, et al. Optical coherence tomography. *Science* (1991) **254**(5035):1178–81. doi:10.1126/science.1957169

6. Adhi M, Duker JS. Optical coherence tomography – current and future applications. *Curr Opin Ophthalmol* (2013) **24**(3):213–21. doi:10.1097/ICU.0b013e32835f8bf8

7. Sakata LM, DeLeon-Ortega J, Sakata V, Girkin CA. Optical coherence tomography of the retina and optic nerve – a review. *Clin & Exp Ophthalmol* (2009) **37**(1):90–9. doi:10.1111/j.1442-9071.2009.02015.x

8. Drexler W, Fujimoto J. State-of-the-art retinal optical coherence tomography. *Prog Retin Eye Res* (2008) **27**(1):45–88. doi:10.1016/j.preteyeres.2007.07.005

9. Li X, Chen H, Qi X, Dou Q, Fu CW, Heng PA. H-DenseUNet: hybrid densely connected UNet for liver and tumor segmentation from CT volumes. *IEEE Trans Med Imaging* (2018) **37**(12):2663–74. doi:10.1109/TMI.2018.2845918

10. Chalam K, Sambhav K. Optical coherence tomography angiography in retinal diseases. *J Ophthalmic Vis Res* (2016) **11**(1):84. doi:10.4103/2008-322X.180709

11. Kim G, Kim J, Choi WJ, Kim C, Lee S. Integrated deep learning framework for accelerated optical coherence tomography angiography. *Sci Rep* (2022) **12**(1):1289. doi:10.1038/s41598-022-05281-0

12. Alam M, Zhang Y, Lim JI, Chan RVP, Yang M, Yao X. Quantitative optical coherence tomography angiography features for objective classification and staging of diabetic retinopathy. *Retina* (2020) **40**(2):322–32. doi:10.1097/IAE.0000000000002373

13. Le D, Alam M, Yao CK, Lim JI, Hsieh YT, Chan RVP, et al. Transfer learning for automated OCTA detection of diabetic retinopathy. *Translational Vis Sci & Technology* (2020) **9**(2):35. doi:10.1167/tvst.9.2.35

14. Le D, Alam M, Miao BA, Lim JI, Yao X. Fully automated geometric feature analysis in optical coherence tomography angiography for objective classification of diabetic retinopathy. *Biomed Opt Express* (2019) **10**(5): 2493. doi:10.1364/BOE.10.002493

15. Alam M, Le D, Lim JI, Yao X. Vascular complexity analysis in optical coherence tomography angiography of diabetic retinopathy. *Retina* (2021) **41**(3): 538–45. doi:10.1097/IAE.0000000000002874

16. Le D, Alam MN, Lim JI, Chan RVP, Yao X. Deep learning for objective OCTA detection of diabetic retinopathy. In: Manns F, Söderberg PG, Ho A, editors. *Ophthalmic technologies XXX*. SPIE (2020). 60. doi:10.1117/12.2546586

17. Alam MN, Son T, Toslak D, Lim JI, Yao X. Quantitative artery-vein analysis in optical coherence tomography angiography of diabetic retinopathy. In: Manns F, Söderberg PG, Ho A, editors. *Ophthalmic technologies XXIX*. SPIE (2019). 1. doi:10.1117/12.2510213

18. Alam MN, Zhang Y, Lim JI, Chan RVP, Yang M, Yao X. Quantitative OCT angiography for computer-aided classification of diabetic retinopathy. *Invest Ophthalmol Vis Sci* (2018) **59**(9):1224.

19. Alam M, Toslak D, Lim JI, Yao X. Color fundus image guided artery-vein differentiation in optical coherence tomography angiography. *Invest Opthalmology & Vis Sci* (2018) **59**(12):4953. doi:10.1167/iovs.18-24831

20. Palejwala NV, Jia Y, Gao SS, Liu L, Flaxel CJ, Hwang TS, et al. Detection of nonexudative choroidal neovascularization in age-related macular degeneration with optical coherence tomography angiography. *Retina* (2015) **35**(11):2204–11. doi:10.1097/IAE.0000000000000867

21. Burlina PM, Joshi N, Pekala M, Pacheco KD, Freund DE, Bressler NM. Automated grading of age-related macular degeneration from color fundus images using deep convolutional neural networks. *JAMA Ophthalmol* (2017) **135**(11):1170. doi:10.1001/jamaophthalmol.2017.3782

22. Gholami S, Lim JI, Leng T, Ong SSY, Thompson AC, Alam MN. Federated learning for diagnosis of age-related macular degeneration. *Front Med* (2023) **10**: 1259017. doi:10.3389/fmed.2023.1259017

23. Holló G. Vessel density calculated from OCT angiography in 3 peripapillary sectors in normal, ocular hypertensive, and glaucoma eyes. *Eur J Ophthalmol* (2016) **26**(3):e42–e45. doi:10.5301/ejo.5000717

24. Hsieh YT, Alam MN, Le D, Hsiao CC, Yang CH, Chao DL, et al. OCT angiography biomarkers for predicting visual outcomes after ranibizumab treatment for diabetic macular edema. *Ophthalmol Retina* (2019) **3**(10):826–34. doi:10.1016/j.oret.2019.04.027

25. Alam M, Thapa D, Lim JI, Cao D, Yao X. Quantitative characteristics of sickle cell retinopathy in optical coherence tomography angiography. *Biomed Opt Express* (2017) **8**(3):1741. doi:10.1364/BOE.8.001741

26. Alam M, Thapa D, Lim JI, Cao D, Yao X. Computer-aided classification of sickle cell retinopathy using quantitative features in optical coherence tomography angiography. *Biomed Opt Express* (2017) **8**(9):4206. doi:10.1364/BOE.8.004206

27. Alam M, Lim JI, Toslak D, Yao X. Differential artery–vein analysis improves the performance of OCTA staging of sickle cell retinopathy. *Translational Vis Sci & Technology* (2019) **8**(2):3. doi:10.1167/tvst.8.2.3

28. Zahid S, Alam MN, Yao X, Lim JI. Quantitative optical coherence tomography angiography parameters in central retinal vein occlusion. *Invest Ophthalmol Vis Sci* (2018) **59**(9):5427.

29. Chen JL, Zahid S, Alam MN, Yao X, Lim JI. Assessment of quantitative optical coherence tomography angiography parameters in branch retinal vein occlusion and monitoring response to treatment. *Invest Ophthalmol Vis Sci* (2018) **59**(9):5458.

30. Alam MN, Thapa D, Lim JI, Cao D, Yao X Automatic classification of sickle cell retinopathy using quantitative features in optical coherence tomography angiography. *Invest Ophthalmol Vis Sci* (2017) **58**(8):1679.

31. Wang J, Hormel TT, Tsuboi K, Wang X, Ding X, Peng X, et al. Deep learning for diagnosing and segmenting choroidal neovascularization in OCT angiography in a large real-world data set. *Translational Vis Sci & Technology* (2023) **12**(4):15. doi:10.1167/tvst.12.4.15

32. Lin L, Wang Z, Wu J, Huang Y, Lyu J, Cheng P, et al. "BSDA-Net: a boundary shape and distance aware joint learning framework for segmenting and classifying OCTA images," in Computing and computer assisted intervention – MICCAI 2021: 24th international conference, proceedings, part VIII, Strasbourg, France, September 27–October 1, 2021 (2021). 65–75. (Boundary shape and distance, FAZ, segmentation, classification, OCTA, joint learning). doi:10.1007/978-3-030-87237-3_7

33. Anvari P, Ashrafkhorasani M, Habibi A, Falavarjani KG. Artifacts in optical coherence tomography angiography. *J Ophthalmic & Vis Res* (2021) **16**:271–86. doi:10.18502/jovr.v16i2.9091

34. Lee CS, Tyring AJ, Wu Y, Xiao S, Rokem AS, DeRuyter NP, et al. Generating retinal flow maps from structural optical coherence tomography with artificial intelligence. *Sci Rep* (2019) **9**(1):5694. doi:10.1038/s41598-019-42042-y

35. Zhang Z, Ji Z, Chen Q, Yuan S, Fan W. Texture-guided U-net for OCT-to-OCTA generation. In: Ma H, Wang L, Zhang C, editors. Pattern Recognition and computer vision. *Vol 13022. Lecture notes in computer science*. Springer International Publishing (2021). 42–52. doi:10.1007/978-3-030-88013-2_4

36. Li S, Zhang D, Li X, Ou C, An L, Xu Y, et al. Vessel-promoted OCT to OCTA image translation by heuristic contextual constraints. *Med Image Anal* (2024) **98**: 103311. doi:10.1016/j.media.2024

37. Li PL, O'Neil C, Saberi S, Sinder K, Wang K, Tan B, et al. Deep learning algorithm for generating optical coherence tomography angiography (OCTA) maps of the retinal vasculature. In: Zelinski ME, Taha TM, Howe J, Awwal AA, Iftekharuddin KM, editors. *Applications of machine learning 2020*. SPIE (2020). **11511**: 8. doi:10.1117/12.2568629

38. Valizadegan H, Nguyen Q, Hauskrecht M. Learning classification models from multiple experts. *J Biomed Inform* (2013) **46**(6):1125–35. doi:10.1016/j.jbi.2013.08.007

39. Le D, Son T, Kim TH, Adejumo T, Abtahi M, Ahmed S, et al. Deep learning-based optical coherence tomography angiography image construction using spatial vascular connectivity network. *Commun Eng* (2024) **3**(1):28. doi:10.1038/s44172-024-00173-9

40. Ronneberger O, Fischer P, Brox T. U-net: convolutional networks for biomedical image segmentation. In: Navab N, Hornegger J, Wells WM, Frangi AF, editors. Medical image Computing and computer-assisted intervention – MICCAI 2015. *Vol 9351. Lecture notes in computer science*. Springer International Publishing (2015). 234–41. doi:10.1007/978-3-319-24574-4_28

41. Isola P, Zhu JY, Zhou T, Efros AA. Image-to-Image translation with conditional adversarial networks (2024). Available from: http://arxiv.org/abs/1611.07004 (Accessed February 20, 2024).

42. Zhu JY, Park T, Isola P, Efros AA. Unpaired image-to-image translation using cycle-consistent adversarial networks (2024). Available from: http://arxiv.org/abs/1703.10593 (Accessed February 20, 2024).

43. Heusel M, Ramsauer H, Unterthiner T, Nessler B, Hochreiter S. *GANs trained by a two time-scale update rule converge to a local nash equilibrium* (2024). doi:10.48550/ARXIV.1706.08500

44. Wang S, Ma K, Yeganeh H, Wang Z, Lin W. A patch-structure representation method for quality assessment of contrast changed images. *IEEE Signal Process Lett* (2015) **22**(12):2387–90. doi:10.1109/LSP.2015.2487369

45. Chao SC, Yang SJ, Chen HC, Sun CC, Liu CH, Lee CY. Early macular angiography among patients with glaucoma, ocular hypertension, and normal subjects. *J Ophthalmol* (2019) **2019**:1–7. doi:10.1155/2019/7419470

46. Pedinielli A, Bonnin S, Sanharawi ME, Mané V, Erginay A, Couturier A, et al. Three different optical coherence tomography angiography measurement methods for assessing capillary density changes in diabetic retinopathy. *Ophthalmic Surg Lasers Imaging Retina* (2017) **48**(5):378–84. doi:10.3928/23258160-20170428-03

47. Mastropasqua R, Toto L, Mastropasqua A, Aloia R, De Nicola C, Mattei PA, et al. Foveal avascular zone area and parafoveal vessel density measurements in different stages of diabetic retinopathy by optical coherence tomography angiography. *Int J Ophthalmol* (2017) **10**(10):1545–1551. doi:10.18240/ijo.2017.10.11

48. Jhaj G, Glazman S, Shrier EM, Bodis-Wollner I. Non-exudative age-related macular degeneration foveal avascular zone area, foveal vessel density, and ganglion cell complex thickness. *Invest Ophthalmol Vis Sci* (2017) **58**(8):36.

49. Al-Sheikh M, Iafe NA, Phasukkijwatana N, Sadda SR, Sarraf D. Biomarkers of neovascular activity in age-related macular degeneration using optical coherence tomography angiography. *Retina* (2018) **38**(2):220–30. doi:10.1097/IAE.0000000000001628

50. Akagi T, Uji A, Huang AS, Weinreb RN, Yamada T, Miyata M, et al. Conjunctival and intrascleral vasculatures assessed using anterior segment optical coherence tomography angiography in normal eyes. *Am J Ophthalmol* (2018) **196**:1–9. doi:10.1016/j.ajo.2018.08.009

51. Ye H, Zheng C, Lan X, Zhao L, Qiao T, Li X, et al. Evaluation of retinal vasculature before and after treatment of children with obstructive sleep apnea-hypopnea syndrome by optical coherence tomography angiography. *Graefes Arch Clin Exp Ophthalmol* (2019) **257**(3):543–8. doi:10.1007/s00417-018-04207-9

52. Chu Z, Lin J, Gao C, Xin C, Zhang Q, Chen CL, et al. Quantitative assessment of the retinal microvasculature using optical coherence tomography angiography. *J Biomed Opt* (2016) **21**(6):066008. doi:10.1117/1.JBO.21.6.066008

53. Li M, Huang K, Xu Q, Yang J, Zhang Y, Ji Z, et al. A retinal dataset for optical coherence tomography angiography study. *Med. Image Anal.* (2024) **93**:103092. doi:10.1016/j.media.2024.103092

EBM Experimental Biology and Medicine

TYPE Original Research
PUBLISHED 20 November 2024
DOI 10.3389/ebm.2024.10295

OPEN ACCESS

*CORRESPONDENCE
Jian Pan,
✉ jianpancn@scu.edu.cn

RECEIVED 19 June 2024
ACCEPTED 07 November 2024
PUBLISHED 20 November 2024

CITATION
Hu L, Zhang N, Zhao C and Pan J (2024) Engineering ADSCs by manipulating YAP for lymphedema treatment in a mouse tail model.
Exp. Biol. Med. 249:10295.
doi: 10.3389/ebm.2024.10295

Engineering ADSCs by manipulating YAP for lymphedema treatment in a mouse tail model

Liru Hu, Nian Zhang, Chengzhi Zhao and Jian Pan*

State Key Laboratory of Oral Diseases, National Center for Stomatology, National Clinical Research Center for Oral Diseases, Department of Oral and Maxillofacial Surgery, West China Hospital of Stomatology, Sichuan University, Chengdu, Sichuan, China

Abstract

Secondary lymphedema is a chronic disease associated with deformity of limbs and dysfunction; however, conventional therapies are not curative. Adipose-derived stem cells (ADSCs) based therapy is a promising way, but a single transplantation of ADSCs has limited efficacy. In this study, ADSCs were engineered *in vitro* and then transplanted into the site of lymphedema. Yes-associated protein (YAP), a crucial regulator of Hippo pathway, plays an important role in regulating stem cell functions. We examined the YAP expression in a mouse tail lymphedema model, and found that transplanted ADSCs exhibited high expression level of YAP and a large number of YAP positive cells existed in lymphedema environment. *In vitro*, the downregulation of YAP in ADSCs resulted in higher expression levels of genes related to lymphangiogenesis such as Lyve-1, VEGFR-3 and Prox-1. *In vivo*, YAP-engineered ADSCs generated abundant VEGFR-3-positive lymphatic vessels and significantly improved subcutaneous fibrosis. These results indicated that the transplantation of pre-engineered ADSCs by manipulating YAP is a promising strategy for lymphatic reconstruction.

KEYWORDS

YAP, verteporfin, ADSCs, lymphedema, lymphangiogenesis

Impact statement

Millions of patients suffer from secondary lymphedema; however, conventional therapies are not curative. Promoting the growth of lymphatic vessels and reconstructing the lymphatic system are the key to ameliorate lymphedema. This study aimed to explore the role of Hippo pathway in regulating adipose-derived stem cell (ADSC) fate during the process of lymphangiogenesis and investigated the efficacy of engineered ADSC based therapy in lymphedema. The study showed that lymphedema-associated ADSCs exhibited high expression level of YAP and a large number of YAP positive cells existed in lymphedema environment. *In vitro*, the downregulation of YAP in ADSCs resulted in higher expression levels of genes related to lymphangiogenesis such as

Lyve-1, VEGFR-3 and Prox-1. *In vivo*, YAP-engineered ADSCs generated abundant VEGFR-3-positive lymphatic vessels and significantly improved subcutaneous fibrosis. This work provided new scientific evidences for revealing the mechanism of promoting lymphangiogenesis and YAP-engineered ADSC based therapy for patients suffering from lymphedema.

Introduction

Lymphedema, a prevalent progressive ailment, arises from impaired lymphatic vessel functionality, leading to the swelling of local tissue and subsequent discomfort and dysfunction. This condition significantly compromises the quality of life for patients [1, 2]. The goal of treatment is to alleviate symptoms, impede the advancement, and mitigate the potential hazard of lymphedema. By far, medical and surgical treatments of lymphedema are ineffective in restoring the normal functions of the lymphatic system, thereby exposing patients to the potential of experiencing recurring symptoms [3, 4]. Thus, it is urgent to find a novel method targeting in promoting reconstruction of lymphatic systems for lymphedema.

Mesenchymal stem cells (MSCs) have demonstrated great therapeutic benefits both in clinical trials and fundamental assays [5, 6]. MSCs can help tissue regeneration by secreting cytokines, chemokines, and growth factors [7]. The use of MSCs in skin wound healing and other soft tissue repairing has achieved significant progress in recent years [8, 9]. Adipose-derived stem cells (ADSCs) were first isolated and identified in 2002, and obtaining ADSCs is less invasive than other types of MSCs which makes them a good candidate for regenerative medicine [10–12]. Promoting the growth of lymphatic vessels is the key to ameliorate lymphedema. With the development of stem cell therapy, transplantation of MSCs has achieved the purpose of repairing and rebuilding the lymphatic network, thus regarded as an ideal therapy for lymphedema [13–15]. In previous studies, the use of ADSCs in the treatment of lymphedema significantly led to volume reduction and subjective improvement both in animals and humans, and no adverse reactions were reported [16–19]. Further research on the mechanism of how ADSCs promote lymphangiogenesis will help to optimize and maximize the efficacy of ADSC-assisted therapy. Therefore, we focused on the possible signaling pathway in lymphangiogenesis to find the targets for engineering ADSCs for stem cell therapy.

The Hippo pathway is crucial in regulating cell proliferation apoptosis, differentiation and development by affecting target genes through the key transcription factor TEAD, together with its coactivator Yes-associated protein (YAP) [20–23]. Hyperactivation of YAP promoted stem cell proliferation but inhibited terminal differentiation in many tissues including intestine, lung and skin [24–26]. And YAP activation promoted tissue fibrosis by regulating the activation of myofibroblasts. The inhibition of YAP expression is associated with poor fibrogenesis in livers and kidneys, conversely, fibroblasts with YAP overexpression caused accumulation of extracellular matrix components and lung fibrosis [27, 28]. Fibrosis, an irreversible pathological change, is one of the most important pathological characteristics in the process of lymphedema. Therefore, improving fibrosis is of great significance in alleviating lymphedema [1, 2]. Thus, we speculated that manipulating the expression of YAP in ADSCs facilitated cell differentiation and improved fibrosis, helping make a recovery from lymphedema.

Based on the above results, it can be speculated that the downregulation of YAP expression could promote the differentiation of ADSCs toward lymphatic endothelial cells (LECs). This study aimed to investigate the efficacy of manipulating YAP in ADSCs based therapy in a mouse lymphedema model, so as to provide new ideas for the clinical treatment of lymphedema.

Materials and methods

Cell culture

White adipose tissue in the inguinal was collected from postnatal 7-day C57BL/6 mice (purchased from Dashuo Experimental Animal Limited Company, Chengdu, China). Harvested tissue was digested in collagenase I (C2-BIOC, Sigma, St. Louis, MO, United States) for 1 h and centrifuged at 1,500 rpm for 5 min to obtain the cell-debris pellet. The pellet was resuspended in αMEM medium (12561056, Gibco, Grand Island, NY, United States) supplemented with 10% FBS (A5669701, Gibco) and 1% penicillin/streptomycin (15140122, Gibco) in an incubator. The medium was changed every other day. Cells were passaged when reaching 80% confluence and the third passages of ADSCs were used in follow-up experiments. Then 1×10^6 ADSCs were seeded in each well of the 6-well plate. For the lymphatic transdifferentiation of ADSCs, VEGFC (100 ng/mL, HY-P77864, MedChem Express, Monmouth Junction, NJ, United States) was used for 7 days. For YAP engineering, verteporfin (20μM, HY-B0146, MedChem Express) was used for 48 h.

Animal model establishment

All procedures were registered and approved by the Ethics Committees of the State Key Laboratory of Oral Diseases, West China School of Stomatology, Sichuan University (WCHSIRB-D-2022-277). Six-week-old female adult C57BL/6 mice weighing an average of 20 g (purchased from Dashuo Experimental Animal Limited Company, Chengdu, China) were used in this study. All animals were maintained with free access to laboratory food and water.

To establish the lymphedema tail model, the mice were anesthetized by inhalation of 5% isoflurane. Throughout the surgical interventions, anesthesia was sustained with 2% isoflurane to ensure the animals remained unconscious. A 2-mm wide full-thickness circumferential skin piece was dissected at 20 mm distal from the tail base, removing superficial lymphatic vessels in the process. Following the subcutaneous injection of 0.1% Evans blue dye into the tip of the tail, the deep lymphatic vessels were cut carefully without damaging accompanied veins. To maintain a moist and infection-free environment, the surgical site was covered with sterile gauze and treated with erythromycin ointment for 24 h.

Isolation of lymphedema-associated ADSCs

CM-Dil dye stock was prepared as recommended by the manufacturer (V22888, Thermo Fisher Scientific, Waltham, MA, United States) to label ADSCs for 5 min at 37°C, and then for an additional 15 min at 4°C. Next, the cell suspension was centrifuged and then the cells were washed twice in sterile PBS. Subsequently, local subcutaneous transplantation of 2×10^6 CM-Dil-labeled ADSCs along with 30 μL PBS was performed at lymphedema site in the lymphedema tail 1 week after surgery. Then mice were euthanized after 48 h, and soft tissue of the entire tail was digested to obtain single-cell suspension for flow cytometric cell sorting of CM-Dil-labeled ADSCs.

Quantitative real-time PCR

At the designated times, cells were collected to test the relative mRNA expression of LEC-related markers and TAP. The reverse transcription of the total RNA was completed by using the HiScript II Q RT SuperMix for qPCR kit (Vazyme Biotech, China). The synthesized cDNA templates were used to do quantitative real-time PCR by using SYBR Green PCR reagents (Bio-Rad, United States). The ΔΔCt (the threshold cycle) values were calculated and the results were expressed as the ratio of the mRNA copies of target genes to that of GAPDH gene (reference gene). The primers involved in our study were showed as follows: 5′- CAG CAC ACT AGC CTG GTG TTA -3′ (forward) and 5′- CGC CCA TGA TTC TGC ATG TAG A-3′ (reverse) for Lyve-1; 5′- ACA GAA GCT AGG CCC TAC TG -3′ (forward) and 5′-ACC CAC ATC GAG TCC TTC CT -3′ (reverse) for VEGFR-3; 5′- AGA AGG GTT GAC ATT GGA GTG A-3′ (forward) and 5′- TGC GTG TTG CAC CAC AGA ATA -3′ (reverse) for Prox-1; 5′- TGT TTA TGG GAC AGT CCG GG -3′ (forward) and 5′- CGA GGA CGG ATT CAT CTT TCT GG -3′ (reverse) for YAP; 5′- TGG ATT TGG ACG CAT TGG TC -3′ (forward) and 5′- TTT GCA CTG GTA CGT GTT GAT -3′ (reverse) for GAPDH.

Immunofluorescence staining

After removing the medium, the cells were washed with PBS three times before being fixed for half an hour with 4% paraformaldehyde. Subsequently, the cells were permeabilized using 0.5% Triton X-100 (T8200, Solarbio, Beijing, China) and blocked for 30 min at room temperature using 2% FBS. Following an overnight incubating at 4°C with primary antibodies, the cells were then treated for 1 h at room temperature with secondary antibodies and 10 min at room temperature with 4′,6-diamidino-2-phenylindole dihydrochloride (DAPI, C0065, Solarbio). An Olympus inverted fluorescence microscope was used to capture the images. Paraffin tissue sections were deparaffinized in xylene and rehydrated through graded ethanol solutions. After being repaired by EDTA (C1034, Solarbio), the sections were blocked by 5% BSA for 30 min at room temperature and incubated with primary antibodies overnight at 4°C. Following steps were the same as cellular immunofluorescence described above. A confocal microscope (N-STORM & A1, Nikon) was used to capture the images.

The primary and secondary antibodies used in this study were as follows: anti-VEGFR-3 (1: 200 dilution, Hunan Biotechnology), anti-YAP (1: 200 dilution, Proteintech), goat anti-rabbit 488 (1:200 dilution, Hunan Biotechnology).

Western blot

At the designated times, nuclear and cytosolic extracts from ADSCs were prepared with a Nuclear Protein Extraction Kit (P0027, Beyotime, Shanghai, China). And total proteins were collected by using RIPA (V900854, Sigma) for ADSC lysis. Subsequently, the proteins run on 10% gels (PG112, Epizyme Biotech, Shanghai, China) and were transferred to poly-(vinylidene fluoride) (PVDF) membranes. Following an overnight incubating at 4°C with primary antibodies, the membranes were treated for 1 h at room temperature with secondary antibodies. Chemiluminescence images were taken by a chemiluminescence machine (Bio-Rad, Hercules, CA, United States). The primary antibodies used in this study were as follows: anti-GAPDH (1: 5,000 dilution, ET1601-4, Hunan Biotechnology, Hangzhou, China), anti-H3 (1: 5,000 dilution, M1309-1, Hunan Biotechnology), anti-VEGFR-3 (1: 1,000 dilution, ER65750, Hunan Biotechnology) and anti-YAP (1: 2,000 dilution, 13584-1-AP, Proteintech).

Tube formation assay

The 24-well plate was coated with Matrigel (356234, Corning Incorporated, Corning, NY, United States), then the gel was allowed to polymerize at 37°C for 30 min. The ADSCs were seeded on the gel (1×10^5 cells/well) and images were taken 12 h after seeding.

The transplantation of ADSCs

After surgery, the mice of tail lymphedema model were randomly divided into three groups to and received weekly local subcutaneous injections around the incision gap.

The control group was administered 30 μL PBS. The ADSC group was administered 2×10^6 ADSCs along with 30 μL PBS [29–31]. The ADSC-verteporfin group received the same amount of Yap-engineered ADSCs along with 30 μL PBS.

Quantitative evaluation of lymphedema

The degree of lymphedema was assessed by the circumference of the tail at two specific sites (5 mm and 10 mm distal from the incision) weekly. The measurements were conducted three times, and the averages were computed.

Histological and immunohistochemical staining

The lymphedema tails were obtained at the second and fourth weeks after surgery. The tissues were preserved in a 4% paraformaldehyde solution for 48 h and then placed in paraffin following decalcification. The samples were divided into sections at intervals of 5 μm, starting from a distance of 10 mm away from the surgical site. To evaluate the degree of subcutaneous fibrosis, the paraffin-embedded tissue sections were stained with Masson's trichrome stain following conventional methods. And Picro-Sirius red staining was performed to analyze the collagen type I and III by using the commercial Kit (MM1036, Maokang bio, Shanghai, China) according to the manufacturer's instructions.

For immunohistochemical staining, after being repaired by EDTA (C1034, Solarbio), the slides were rinsed with water and incubated with the primary antibodies overnight at 4°C. Then the slides were rinsed and incubated with the corresponding secondary antibody for 30 min followed by 3,3′-diaminobenzidine and hematoxylin staining, respectively. The primary antibodies used in this study were as follows: anti-YAP (1: 50 dilution, ET1611-69, Hunan Biotechnology) and anti-VEGFR-3 (1: 200 dilution, ER65750, Hunan Biotechnology).

Statistical analysis

On the basis of the assessment of the normal distribution of the data, all experiments were performed at least in triplicate. Data were presented as mean ± SD. When parametric test assumptions were met, the statistical significance was determined by one-way analysis of variance (ANOVA using the SPSS 21.0 software). Statistical significance was set at $p < 0.05$.

Results

YAP expression increased in lymphedema-associated ADSCs

The passage 3 ADSCs exhibited the characteristic spindle-like shape, and their ability to differentiate into adipogenic and osteogenic lineages was validated by using oil red staining and alizarin red staining (Figure 1A). The lymphedema tail model was established by the surgical removal of the lymphatic vessels that accompanied the lateral veins (Figures 1B, C). After the transplantation of CM-Dil-labeled ADSCs, the presence of ADSCs were tracked by the IVIS Spectrum *in vivo* optical imaging system within the tail (Figure 1D).

To assess the effect of lymphedema environment on YAP expression in ADSCs, we isolated ADSCs from the lymphedema tail to evaluate the YAP expression in lymphedema-associated ADSCs. Immunofluorescence staining detected significantly higher expression of YAP in lymphedema-associated ADSCs compared to normal ADSCs (Figures 1E, G). As YAP activity is regulated by its nuclear translocation, western blot was used to investigate the nuclear and cytosolic expression of YAP. The results of western blot showed that the nuclear expression of YAP increased in lymphedema-associated ADSCs while the cytosolic expression decreased compared to normal ADSCs (Figures 1F, H, I). Meanwhile, we evaluated YAP expression in the lymphedema tail by immunohistochemical staining. Cells in the lymphedema tail had low expression level of VEGFR-3 and high expression level of YAP compared to the normal tail (Figure 1J). Based on these data, we proposed that YAP expression was positively correlated with the development of lymphedema.

YAP expression decreased after the lymphatic endothelial transdifferentiation of ADSCs

We conducted the lymphatic endothelial transdifferentiation of ADSCs by using VEGFC at a concentration of 100 ng/mL. We observed the upregulation of LEC-related markers including Lyve-1, Prox-1, and VEGFR-3 at mRNA level after 7-day induction (Figures 2A–C). The confirmation of this was further supported by the immunofluorescence staining and western blot of VEGFR-3, as seen in Figures 2D–F, H. Additionally, the tube formation assay was conducted after 7-day induction of VEGFC to measure the ability of ADSCs to form tubes and promote the growth of LECs. This evaluation is

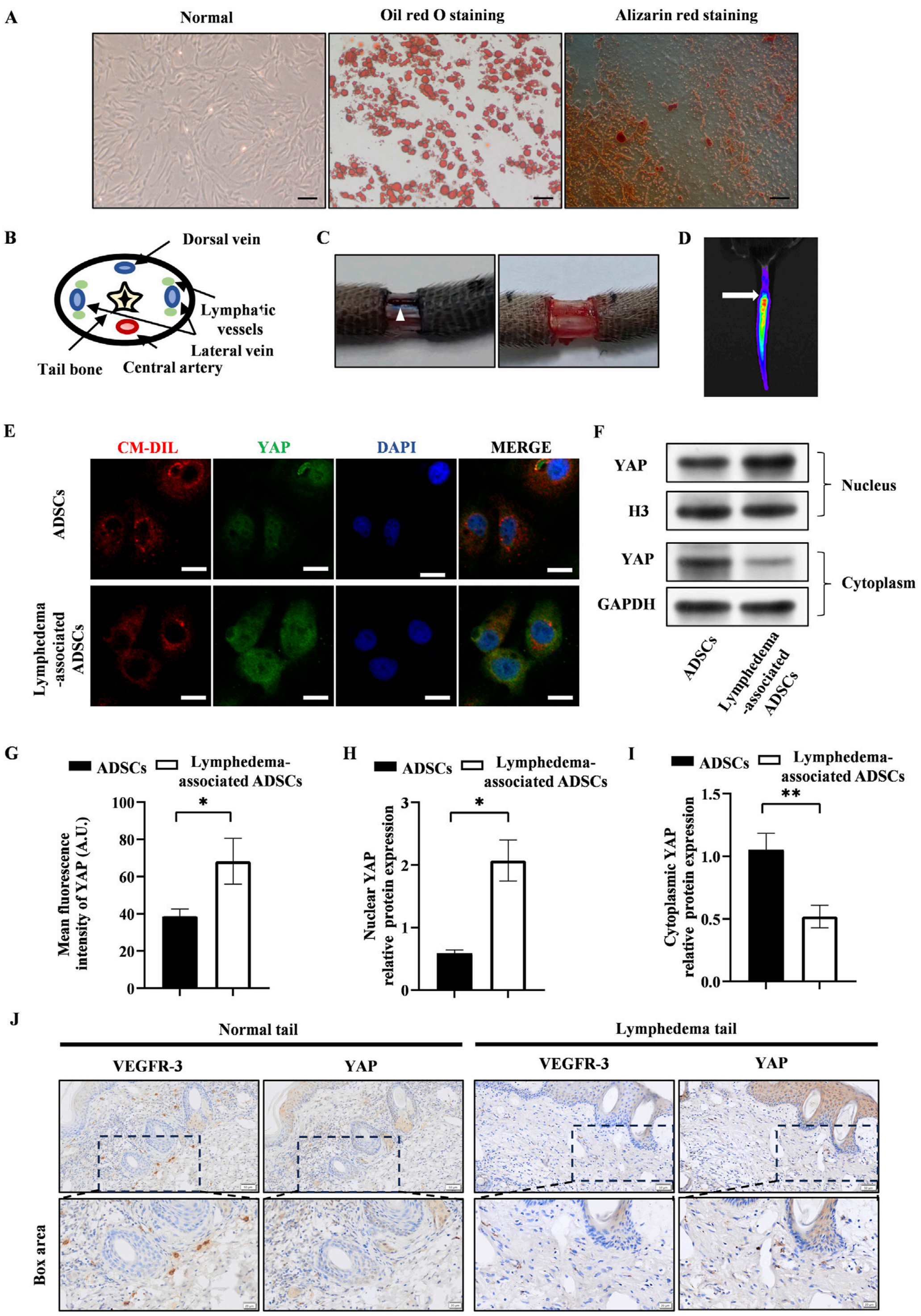

FIGURE 1
YAP expression increased in lymphedema-associated ADSCs. **(A)** Passage 3 ADSCs exhibited the characteristic spindle-like shape. Oil red staining and alizarin red staining showed the osteogenic and adipogenic potential of ADSCs, respectively. Scale bar = 200 μm. **(B)** The anatomical diagram of tail cross section. **(C)** Representative images of the surgical site before and after removing the lymphatic vessels during surgery, and the white triangle indicates the lymphatic vessels. **(D)** Representative image of *in vivo* fluorescence observed in tail transplanted with CM-Dil labeled ADSCs (the arrow points to the surgical incision). **(E)** Representative micrographs of YAP immunostaining in lymphedema-associated ADSCs compared with ADSCs from normal adipose tissue. Scale bar = 20 μm. **(F, H, I)** Western blot showed the increased nuclear YAP expression and decreased cytosolic YAP expression in lymphedema-associated ADSCs compared with ADSCs from normal adipose tissue. **(G)** Immunofluorescence

(*Continued*)

FIGURE 1 (Continued)
intensity analysis of YAP. **(J)** The immunohistochemical staining of the lymphedema tail and normal tail. Cells in lymphedema tail had low expression level of VEGFR-3 and high expression level of YAP. Scale bar = 20 μm and 50 μm. Bars: means ± standard deviation. n = 3 in each group, **P* < 0.05, ***P* < 0.01.

considered the gold standard for determining the impact of VEGFC on lymphangiogenesis. Figure 2G showed that the VEGFC group exhibited tubulogenesis while the control group did not demonstrate the formation of tube-like structures.

Next, we investigated the alteration of YAP after the lymphatic endothelial transdifferentiation. To do this, we conducted immunofluorescence staining to evaluate the YAP expression and found that the expression of YAP exhibited a significant drop in the VEGFC group compared to the control group (Figures 3A, B). The results of western blot showed lower nuclear YAP expression and higher cytosolic expression in the VEGFC group compared to the control group (Figures 3C–E). Based on these data, we speculated that there was a decrease in YAP phosphorylation, leading to a reduction in its nuclear translocation.

The changes in YAP phosphorylation status might be associated with the transdifferentiation process of ADSCs and could potentially influence lymphangiogenesis.

The downregulation of YAP enhanced the lymphatic endothelial transdifferentiation of ADSCs

Verteporfin as a widely recognized YAP inhibitor, was employed to manipulate YAP expression in this investigation. The results of PCR showed that verteporfin suppressed the YAP expression in ADSCs at the concentration of 20 μM (Figure 3F). Meanwhile, we performed western blot to determine the duration of inhibitory effect on YAP after a 48-hour treatment of 20 μM verteporfin (Figures 3G, H). The results showed that the YAP expression was significantly lower in the 48h + D7 group and 48h + D14 group compared to the control group. The inhibitory effect of verteporfin on YAP could last for at least 2 weeks after the 48-hour treatment of verteporfin.

To investigate the effect of YAP downregulation on the lymphatic endothelial transdifferentiation, ADSCs were induced by VEGFC following a 48-hour pretreatment of verteporfin. The expression level of VEGFR-3 increased significantly in the VEGFC (+) verteporfin (+) group compared to the VEGFC (+) verteporfin (−) group, which was improved by immunofluorescence staining (Figures 4A, B) and western blot (Figures 4C, D). In the tube formation assay, the VEGFC (+) verteporfin (+) group generated a greater number of tubes compared to the VEGFC (+) verteporfin (−) group. Interestingly, tubes were observed in the VEGFC (−) verteporfin (+) group (Figures 4E, F). These data indicated that YAP downregulation could enhance the lymphatic endothelium differentiation of ADSCs.

Changes in mouse tail edema after surgery

Following the surgical removal of the lymphatic vessels, a noticeable accumulation of fluid was noted in the mouse tail caused by the obstruction of lymphatic drainage. Figure 5A displayed representative photographs of the mouse tail at 1, 2, 3, and 4 weeks after surgery.

The diameter of the mouse tail gradually increased over time after surgery, reaching a peak at 3 weeks (Figures 5B, C). The tail diameter of the ADSC -verteporfin group increased the least compared to the other groups. The distinction became more apparent when considering the physiological growth of the tail during the experimental period. These data suggested that local transplantation of YAP-downregulation ADSCs could alleviate lymphedema.

YAP-downregulation ADSCs reduced fibrosis in lymphedema

Fibrosis is one of the important pathological characteristics in the process of lymphedema.

Therefore, Masson staining was conducted to visualize the presence of collagen in the subcutaneous tissue at 2 and 4 weeks after surgery. An accumulation of densely packed collagen fibers, stained blue, was observed in the subcutaneous tissue while muscle fibers were stained red (Figure 5D). The control group had higher subcutaneous fibrosis ratio at 2 and 4 weeks after surgery compared to the ADSC group and ADSC-verteporfin group (Figure 5E). It demonstrated that the local transplantation of ADSCs could reduce the degree of fibrosis in lymphedema. And the ADSC-verteporfin group had lower subcutaneous fibrosis ratio at 4 weeks compared to the ADSC group which indicated a more pronounced benefit of YAP-downregulation ADSCs in improving fibrosis. In Picro-Sirius red staining, red-yellow fibers represented collagen type I and green fibers with weak birefringence represented collagen type III (Figure 5F). At 4 weeks, significantly higher collagen type I/III ratio was found in the control group compared to the ADSC group and ADSC-verteporfin group. And the ADSC-verteporfin group showed the lowest collagen type I/III ratio (Figure 5G).

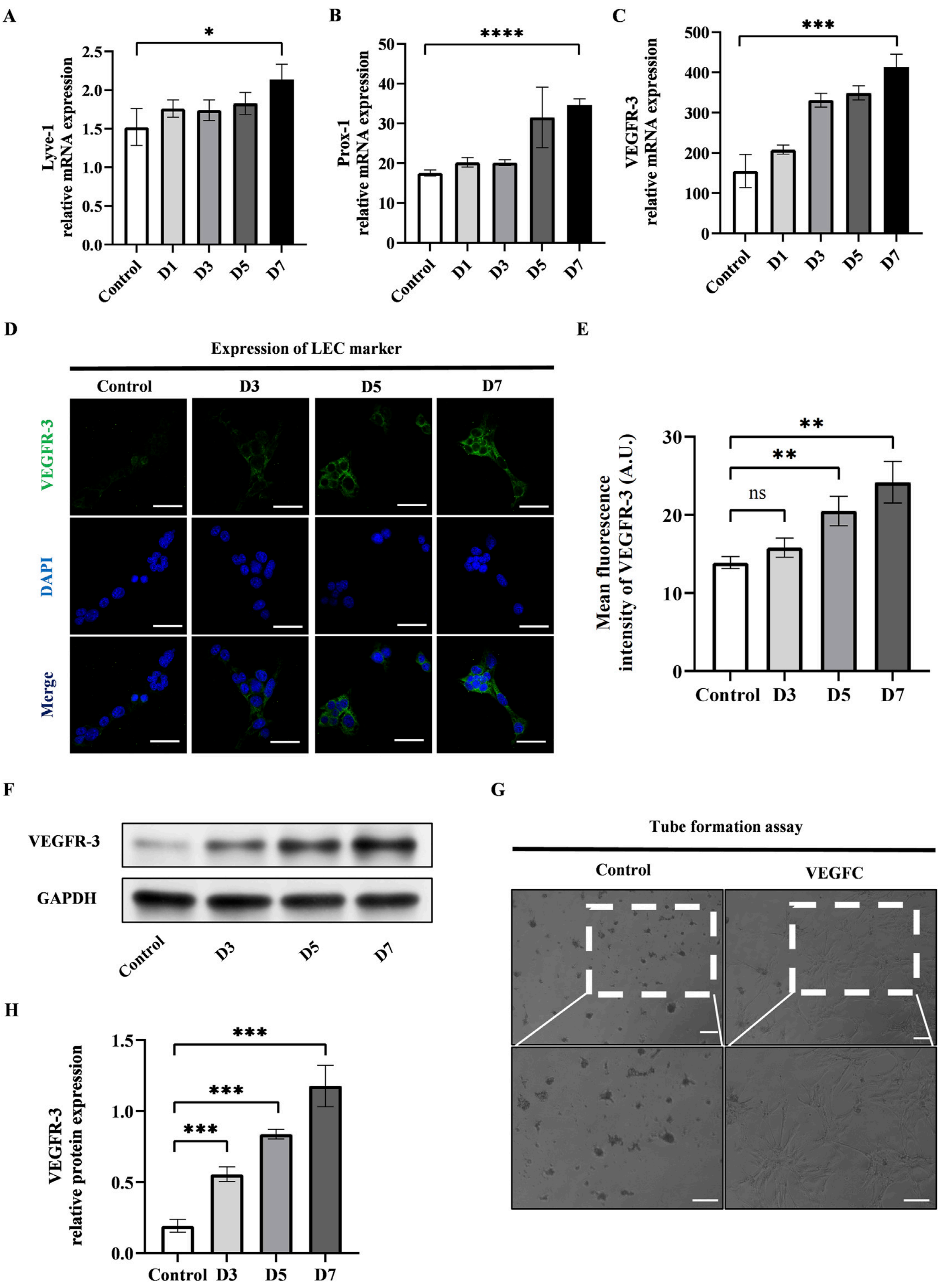

FIGURE 2
VEGFC successfully induced lymphatic endothelial transdifferentiation of ADSCs. **(A–C)** PCR tests showed the upregulation of VEGFR-3, Prox-1, Lyve-1 during the lymphatic endothelial transdifferentiation of ADSCs. **(D)** VEGFR-3 as a typical LEC marker was detected by immunofluorescence staining after VEGFC-induction at the indicated times. Scale bar = 50 μm. **(E)** Immunofluorescence intensity analysis of VEGFR-3. **(F, H)** Western blot showed the increased VEGFR-3 expression during the lymphatic endothelial transdifferentiation of ADSCs. **(G)** ADSCs were seeded on Matrigel after 7-day induction, and tube formation was evaluated at 12 h postseeding. VEGFC group generated tube-like structure while control group did not exhibit tubes. Scale bar = 100 μm. Bars: means ± standard deviation. n = 3 in each group, ns: no significant, $**P < 0.01$, $***P < 0.001$.

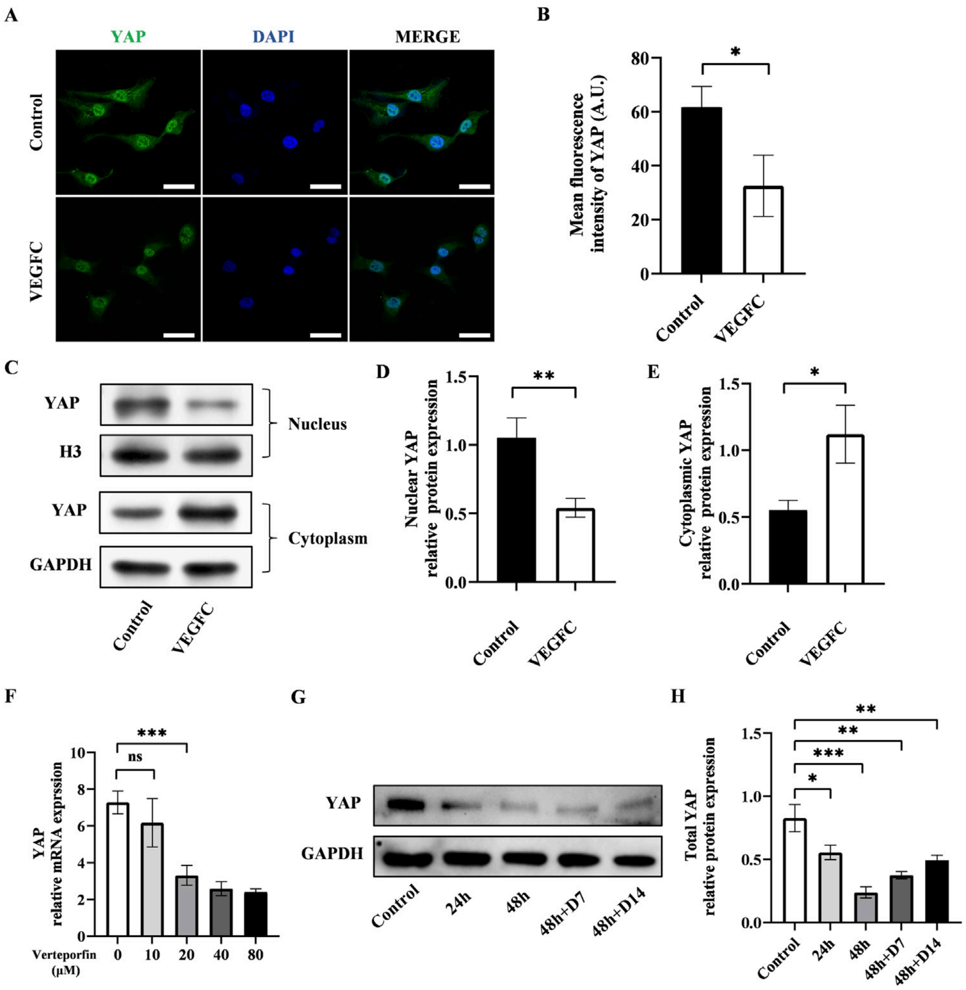

FIGURE 3
Effect of lymphatic endothelial transdifferentiation and verteporfin on the expression of YAP. **(A)** Immunostaining of YAP in the control group and VEGFC group. Scale bar = 50 μm. **(B)** Immunofluorescence intensity analysis of YAP. **(C–E)** Western blot showed the decreased nuclear YAP expression and increased cytosolic YAP expression in ADSCs after lymphatic endothelial transdifferentiation. **(F)** PCR test showed that verteporfin suppressed the expression of YAP in ADSCs at the concentration of 20 μM. **(G, H)** Western blot showed the continuously inhibitory effect of verteporfin on YAP expression in ADSCs. Bars: means ± standard deviation. n = 3 in each group; ns, no significant, **P* < 0.05, ***P* < 0.01, ****P* < 0.001.

YAP-downregulation ADSCs promoted lymphangiogenesis during lymphedema development

In order to assess the formation of lymphatic vessels, we performed immunofluorescence staining for VEGFR-3 on the mouse tails at 2 and 4 weeks after surgery (Figure 6A). By calculating the area and number of lymphatic vessels, we can quantitatively analyze the lymphangiogenesis in each group (Figures 6B, C). The results showed that the control group had significantly smaller lymphatic area and number compared to at 2 and 4 weeks after surgery compared to the ADSC group and ADSC-verteporfin group. It demonstrated that the local transplantation of ADSCs could promote lymphangiogenesis. And the ADSC-verteporfin group exhibited significantly bigger lymphatic area and number at 2 and 4 weeks after surgery compared to the ADSC group which indicated a more pronounced benefit of YAP-downregulation ADSCs in lymphangiogenesis.

Discussion

Stem cells based lymphedema therapies have attracted attention in recent years for its great regeneration ability in reducing edema which has been proved by clinical and basal studies [32]. The pathology of lymphedema is the destruction of lymphatic vessels and excessive fibrosis. Stem cells can promote the growth of lymphatic vessels to reconstruct local lymphatic system at the same time. They have therapeutic

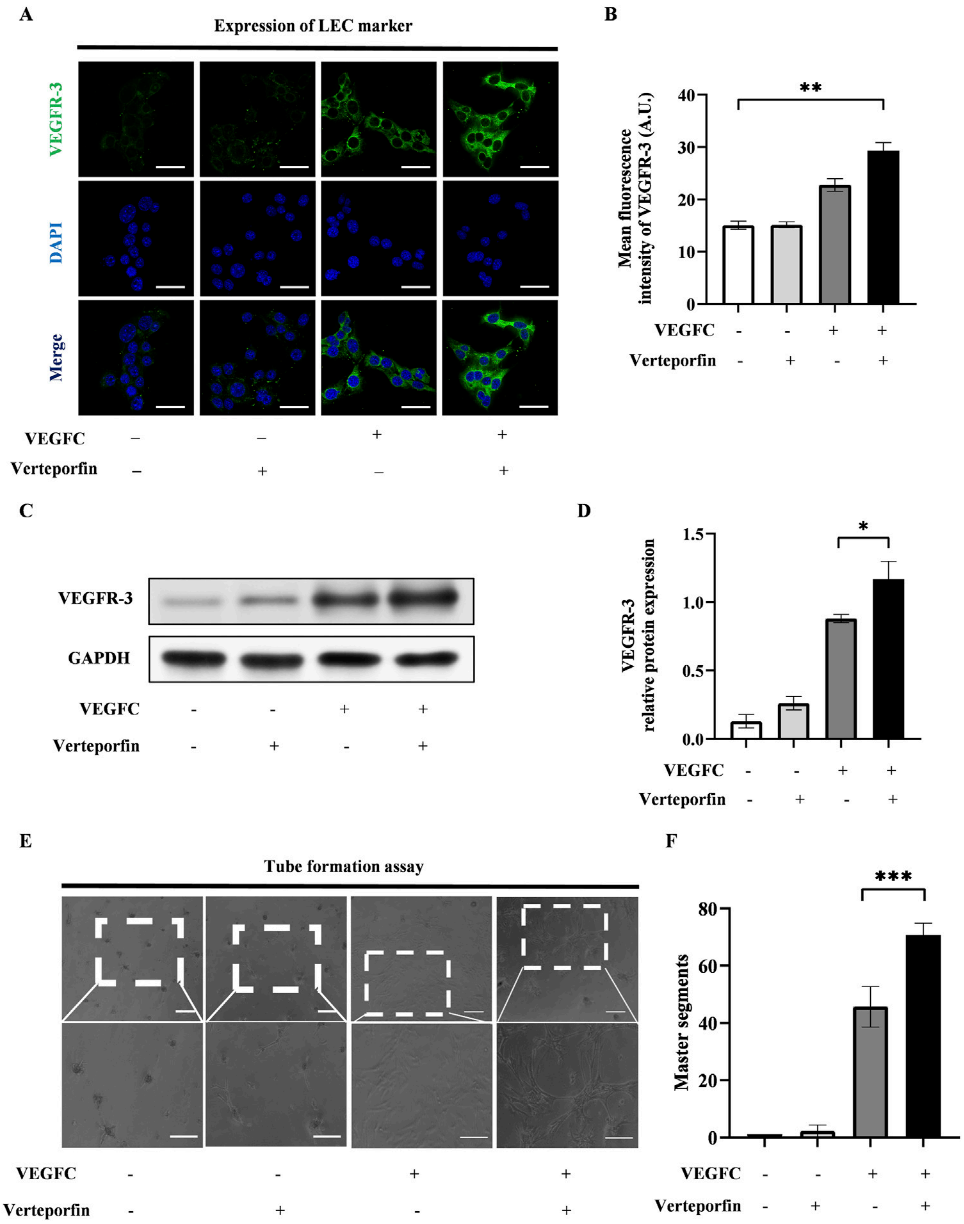

FIGURE 4
The downregulation of YAP enhanced the lymphatic endothelial transdifferentiation of ADSCs *in vitro*. 20 μM verteporfin preconditioning for 48 h downregulated the expression of YAP in ADSCs. Under this inhibitory effect, higher expression levels of VEGFR-3 can be detected after differentiation of ADSCs, and larger density of tube formation can be observed. **(A)** Lymphatic endothelial transdifferentiation of ADSCs was conducted after 20 μM-verteporfin preconditioning for 48 h, and immunofluorescence staining indicated higher level of VEGFR-3. Scale bar = 50 μm. **(B)** Immunofluorescence intensity analysis of VEGFR-3. **(C, D)** Higher expression level of VEGFR-3 was confirmed by western blot. **(E, F)** The tube formation assay showed that VEGFC (+) verteporfin (+) group generated more tube-like structure than VEGFC (+) verteporfin (–) group. And quantification of master segments was analysed. Scale bar = 200 μm. Bars: means ± standard deviation. n = 3 in each group, ns: no significant, *$P <$ 0.05, **$P <$ 0.01, ***$P <$ 0.001.

effects in anti-inflammatory and anti-fibrosis, which makes stem cells ideal for lymphedema treatment [33]. However, a major concern of stem cell therapy is that the transplanted stem cell population is of highly heterogeneous which means the therapeutic efficacy of ADSC transplantation may vary among studies.

The crosstalk between MSCs and LECs is crucial for lymphangiogenesis [34]. The key of MSCs therapy lies in secreting growth factors, and VEFGC is the most important factor among them. Activation of VEGFR-3 by VEGFC results in the phosphorylation of protein kinase B and extracellular regulatory kinase, which can enhance the migration,

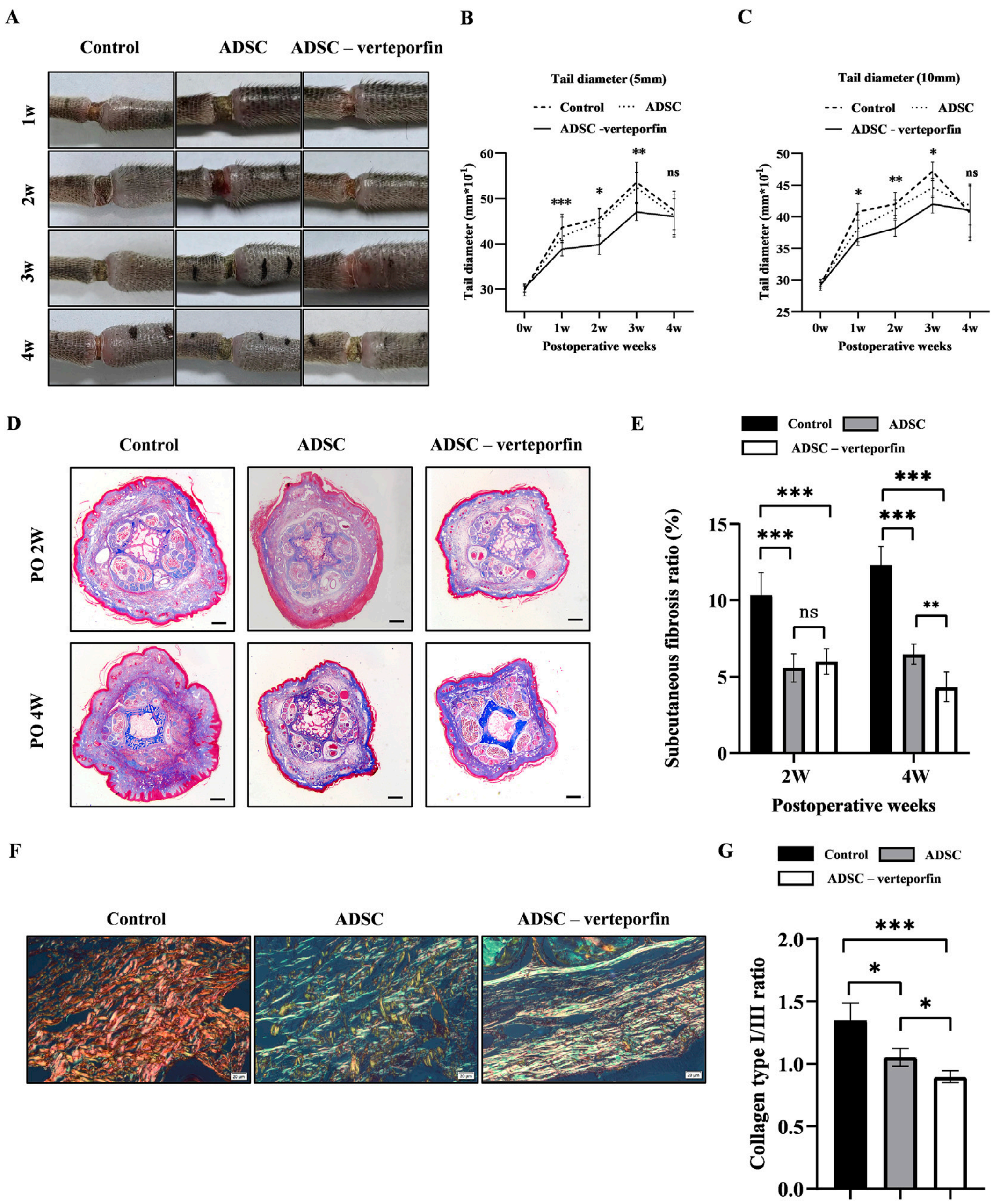

FIGURE 5
YAP-downregulation ADSCs reduced the degree of swelling and improved fibrosis mouse tail lymphedema models. **(A)** Representative images of the mouse tail at 1, 2, 3, and 4 weeks after surgery. **(B, C)** Tail diameter was measured before and after surgery at the site of 5 mm and 10 mm distal from the incision. **(D)** Masson staining of the subcutaneous tissue of mouse tail at 2 and 4 weeks after surgery. Scale bar = 500 μm. **(E)** Statistical analysis of subcutaneous fibrosis ratio. **(F)** Representative results for Picro-Sirius red staining of mouse tail at 2 and 4 weeks after surgery. Red-yellow fibers represented collagen type I and green fibers with weak birefringence represented collagen type III. Scale bar = 20 μm. **(G)** Collagen type I/III ratio showed that more Collagen type III was produced in ADSCs (VEGFC+ verteporfin) group. n = 5 in each group, ns: no significant, *$P < 0.05$, **$P < 0.01$, ***$P < 0.001$.

proliferation, and survival of LECs [35]. Several research examining the preclinical animal model of acquired lymphedema provide evidence for therapeutic lymphangiogenesis through the activation of VEGFC/VEGFR-3 signaling pathways [36–41]. For this study, we used VEGFR-3 as the main marker associated with LECs, and we found that lymphangiogenesis was positively correlated with high expression of VEGFR-3 both *in vitro* and *in vivo*. Then increased growth factors derived from MSCs

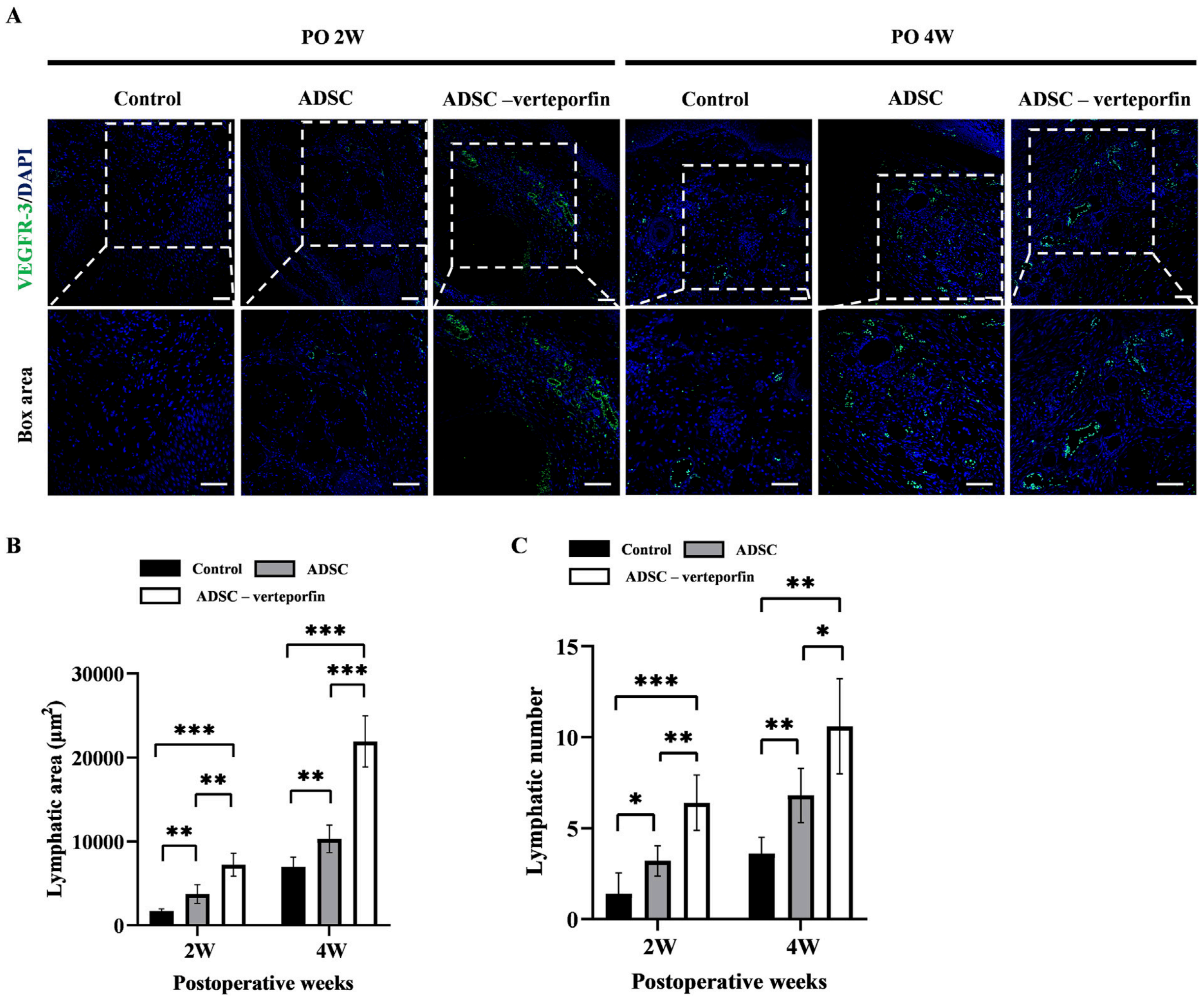

FIGURE 6
The regeneration of lymphatic vessels in the mouse tail lymphedema model. **(A)** Subcutaneous VEGFR-3⁺ lymphatic vessels were detected by immunofluorescence staining. Scale bar = 200 μm. **(B)** Statistical analysis of the area of lymphatic vessels. **(C)** Statistical analysis of the number of lymphatic vessels. n = 5 in each group, $^{*}P < 0.05$, $^{**}P < 0.01$, $^{***}P < 0.001$.

promoted sprouting of lymphatics from LECs by binding to their high affinity receptors. Therefore, engineered MSCs with enhanced secretion function are potentially be utilized towards an effective lymphedema treatment.

YAP expresses abundantly in diverse stem cell populations *in vivo* and *in vitro*, and participates in various physiological and pathological processes by driving stem cell behavior and regeneration [42]. Abnormal expression of YAP drives the development of aging and tumorigenesis associated with stem cell dysfunction which can be reversed by YAP targeted therapies [43]. At the onset of stem cell differentiation, YAP activity is depressed and YAP gene silencing caused the loss of stemness [44]. Altogether, YAP can be regarded as a regulator in balancing progenitor and differentiated cells in different physiological and pathological environment.

In this study, we found that YAP was upregulated in transplanted ADSCs and a large number of YAP positive cells in lymphedema site were seen. These results suggested that YAP played an important role in lymphedema by affecting ADSCs. Verteporfin is an authorized pharmaceutical for the treatment of macular degeneration. Currently, it is employed as a small molecule inhibitor for YAP-TEAD and has demonstrated anti-cancer properties in several forms of solid tumors [45–47]. We used verteporfin to manipulate YAP expression of ADSCs, and the upregulation of VEGFR-3 and increased tube forming capacity indicated that suppressing YAP could induce the lymphogenic phenotype of ADSCs. Furthermore, the transplantation of ADSCs preconditioned with verteporfin exhibited reducing swelling and better lymphangiogenesis in the early stages of secondary lymphedema in in vivo experiments. These results indicated that the downregulation of YAP in ADSCs played an important role in promoting lymphangiogenesis. Engineered ADSCs based on manipulating YAP expression is a practical way to reconstruct lymphatic circulation.

The development of lymphedema is commonly attributed to a feedback loop that involves local inflammation, lymphatic fibrosis, and the deposition of adipose tissue [48]. Chronic inflammation-induced fibrosis plays a key role in the pathophysiology of this disease, which decreases collecting lymphatic pumping, and impairs collateral lymphatic formation. Numerous studies clearly showed the association between fibrosis and lymphedema [49], similarly, in our study, severe fibrosis occurred in untreated lymphedema, and the verteporfin-ADSC therapy showed promise in mitigating the extent of subcutaneous fibrosis. Collagen type I and III are important fiber components in determining the tensile strength of soft tissue. Collagen type I increases stiffness, whereas collagen type III increases the flexibility of tissues [50]. The collagen type I/III ratio is regarded as an informative marker in biological processes and pathological conditions. Altered collagen type I/III ratio was reported to be associated with abnormal regeneration pattern in scar development [51]. However, collagen type I/III ratio is poorly investigated in lymphedema. In this study, we found that verteporfin-ADSC therapy decreased the collagen type I/III ratio in treating lymphangiogenesis. The regulation of collagen type I and III as well as the collagen type I/III ratio may serve as a new target for further investigation. In addition to ability of promoting lymphangiogenesis, engineered ADSCs played a positive role in suppressing fibrosis to improve the outcomes of lymphedema.

Author contributions

LH, NZ, and CZ performed the experiments, acquired, analyzed, interpreted the data, and wrote the manuscript; LH and NZ analyzed and interpreted the data; LH, NZ, and CZ drafted the manuscript; JP supervised the study and revised the manuscript. All authors contributed to the article and approved the submitted version.

Data availability

The datasets presented in this study can be found in online repositories. The names of the repository/repositories and accession number(s) can be found in the article/supplementary material.

Ethics statement

The animal study was approved by the West China Hospital of Stomatology Research Ethics Committee. The study was conducted in accordance with the local legislation and institutional requirements.

Funding

The author(s) declare that financial support was received for the research, authorship, and/or publication of this article. This study is supported by the Health Commission of Sichuan Province (21PJ062); Sichuan Science and Technology Program (2023ZYD0110); Research and Develop Program, West China Hospital of Stomatology Sichuan University (RD-03-202405); Youth Foundation of Sichuan Science and Technology Department (2023NSFSC1514).

Acknowledgments

The authors acknowledge the colleagues of West China Hospital of Stomatology, Sichuan University, Chengdu, China.

Conflict of interest

The author(s) declared no potential conflicts of interest with respect to the research, authorship, and/or publication of this article.

References

1. Brown S, Dayan JH, Kataru RP, Mehrara BJ. The vicious circle of stasis, inflammation, and fibrosis in lymphedema. *Plast Reconstr Surg* (2023) **151**: 330e–341e. doi:10.1097/prs.0000000000009866

2. Donahue PMC, MacKenzie A, Filipovic A, Koelmeyer L. Advances in the prevention and treatment of breast cancer-related lymphedema. *Breast Cancer Res Treat* (2023) **200**:1–14. doi:10.1007/s10549-023-06947-7

3. Boccardo F, Casabona F, De Cian F, Friedman D, Murelli F, Puglisi M, et al. Lymphatic microsurgical preventing healing approach (LYMPHA) for primary surgical prevention of breast cancer-related lymphedema: over 4 years follow-up. *Microsurgery* (2014) **34**:421–4. doi:10.1002/micr.22254

4. Thompson M, Korourian S, Henry-Tillman R, Adkins L, Mumford S, Westbrook KC, et al. Axillary reverse mapping (ARM): a new concept to identify and enhance lymphatic preservation. *Ann Surg Oncol* (2007) **14**:1890–5. doi:10.1245/s10434-007-9412-x

5. Liu J, Gao J, Liang Z, Gao C, Niu Q, Wu F, et al. Mesenchymal stem cells and their microenvironment. *Stem Cel Res Ther* (2022) **13**:429. doi:10.1186/s13287-022-02985-y

6. Wang Y, Fang J, Liu B, Shao C, Shi Y. Reciprocal regulation of mesenchymal stem cells and immune responses. *Cell Stem Cell* (2022) **29**:1515–30. doi:10.1016/j.stem.2022.10.001

7. Yu H, Huang Y, Yang L. Research progress in the use of mesenchymal stem cells and their derived exosomes in the treatment of osteoarthritis. *Ageing Res Rev* (2022) **80**:101684. doi:10.1016/j.arr.2022.101684

8. Hade MD, Suire CN, Suo Z. Mesenchymal stem cell-derived exosomes: applications in regenerative medicine. *Cells* (2021) **10**:1959. Epub ahead of print 1. doi:10.3390/cells10081959

9. Vasanthan J, Gurusamy N, Rajasingh S, Sigamani V, Kirankumar S, Thomas EL, et al. Role of human mesenchymal stem cells in regenerative therapy. *Cells* (2020) **10**:54. Epub ahead of print 31. doi:10.3390/cells10010054

10. Bhattacharjee M, Escobar Ivirico JL, Kan H-M, Shah S, Otsuka T, Bordett R, et al. Injectable amnion hydrogel-mediated delivery of adipose-derived stem cells for osteoarthritis treatment. *Proc Natl Acad Sci U S A* (2022) **119**:e2120968119. Epub ahead of print 25 January 2022. doi:10.1073/pnas.2120968119

11. Sanz-Ros J, Romero-García N, Mas-Bargues C, Monleón D, Gordevicius J, Brooke RT, et al. Small extracellular vesicles from young adipose-derived stem cells prevent frailty, improve health span, and decrease epigenetic age in old mice. *Sci Adv* (2022) **8**:eabq2226. doi:10.1126/sciadv.abq2226

12. Wu B, Feng J, Guo J, Wang J, Xiu G, Xu J, et al. ADSCs-derived exosomes ameliorate hepatic fibrosis by suppressing stellate cell activation and remodeling hepatocellular glutamine synthetase-mediated glutamine and ammonia homeostasis. *Stem Cel Res Ther* (2022) **13**:494. doi:10.1186/s13287-022-03049-x

13. Feng X, Du M, Zhang Y, Ding J, Wang Y, Liu P. The role of lymphangiogenesis in coronary atherosclerosis. *Lymphatic Res Biol* (2022) **20**:290–301. doi:10.1089/lrb.2021.0026

14. Ji R-C. The role of lymphangiogenesis in cardiovascular diseases and heart transplantation. *Heart Fail Rev* (2022) **27**:1837–56. doi:10.1007/s10741-021-10188-5

15. Tammela T, Alitalo K. Lymphangiogenesis: molecular mechanisms and future promise. *Cell* (2010) **140**:460–76. doi:10.1016/j.cell.2010.01.045

16. Hayashida K, Yoshida S, Yoshimoto H, Fujioka M, Saijo H, Migita K, et al. Adipose-derived stem cells and vascularized lymph node transfers successfully treat mouse hindlimb secondary lymphedema by early reconnection of the lymphatic system and lymphangiogenesis. *Plast Reconstr Surg* (2017) **139**:639–51. doi:10.1097/prs.0000000000003110

17. Yoshida S, Hamuy R, Hamada Y, Yoshimoto H, Hirano A, Akita S. Adipose-derived stem cell transplantation for therapeutic lymphangiogenesis in a mouse secondary lymphedema model. *Regen Med* (2015) **10**:549–62. doi:10.2217/rme.15.24

18. Hou C, Wu X, Jin X. Autologous bone marrow stromal cells transplantation for the treatment of secondary arm lymphedema: a prospective controlled study in patients with breast cancer related lymphedema. *Jpn J Clin Oncol* (2008) **38**:670–4. doi:10.1093/jjco/hyn090

19. Maldonado GEM, Pérez CAA, Covarrubias EEA, Cabriales SAM, Leyva LA, Pérez JCJ, et al. Autologous stem cells for the treatment of post-mastectomy lymphedema: a pilot study. *Cytotherapy* (2011) **13**:1249–55. doi:10.3109/14653249.2011.594791

20. Driskill JH, Pan D. The Hippo pathway in liver homeostasis and pathophysiology. *Annu Rev Pathol Mech Dis* (2021) **16**:299–322. doi:10.1146/annurev-pathol-030420-105050

21. Fan M, Lu W, Che J, Kwiatkowski NP, Gao Y, Seo H-S, et al. Covalent disruptor of YAP-TEAD association suppresses defective Hippo signaling. *Elife* (2022) **11**:e78810. Epub ahead of print 27 October 2022. doi:10.7554/eLife.78810

22. Ma S, Meng Z, Chen R, Guan K-L. The Hippo pathway: biology and pathophysiology. *Annu Rev Biochem* (2019) **88**:577–604. doi:10.1146/annurev-biochem-013118-111829

23. Wang L, Choi K, Su T, Li B, Wu X, Zhang R, et al. Multiphase coalescence mediates Hippo pathway activation. *Cell* (2022) **185**:4376–93.e18. doi:10.1016/j.cell.2022.09.036

24. Gregorieff A, Liu Y, Inanlou MR, Khomchuk Y, Wrana JL. Yap-dependent reprogramming of Lgr5(+) stem cells drives intestinal regeneration and cancer. *Nature* (2015) **526**:715–8. doi:10.1038/nature15382

25. Rognoni E, Walko G. The roles of YAP/TAZ and the Hippo pathway in healthy and diseased skin. *Cells* (2019) **8**:411. Epub ahead of print 3 May 2019. doi:10.3390/cells8050411

26. Wu Q, Guo J, Liu Y, Zheng Q, Li X, Wu C, et al. YAP drives fate conversion and chemoresistance of small cell lung cancer. *Sci Adv* (2021) **7**:eabg1850. doi:10.1126/sciadv.abg1850

27. Liang M, Yu M, Xia R, Song K, Wang J, Luo J, et al. Yap/taz deletion in Gli(+) cell-derived myofibroblasts attenuates fibrosis. *J Am Soc Nephrol* (2017) **28**:3278–90. doi:10.1681/asn.2015121354

28. Liu C-Y, Zha Z-Y, Zhou X, Zhang H, Huang W, Zhao D, et al. The Hippo tumor pathway promotes TAZ degradation by phosphorylating a phosphodegron and recruiting the SCFβ-TrCP E3 Ligase. *J Biol Chem* (2010) **285**:37159–69. doi:10.1074/jbc.m110.152942

29. Shimizu Y, Shibata R, Shintani S, Ishii M, Murohara T. Therapeutic lymphangiogenesis with implantation of adipose-derived regenerative cells. *J Am Heart Assoc* (2012) **1**:e000877. doi:10.1161/jaha.112.000877

30. Dai T, Jiang Z, Cui C, Sun Y, Lu B, Li H, et al. The roles of podoplanin-positive/podoplanin-negative cells from adipose-derived stem cells in lymphatic regeneration. *Plast Reconstr Surg* (2020) **145**:420–31. doi:10.1097/prs.0000000000006474

31. Kawai Y, Shiomi H, Abe H, Naka S, Kurumi Y, Tani T. Cell transplantation therapy for a rat model of secondary lymphedema. *J Surg Res* (2014) **189**:184–91. doi:10.1016/j.jss.2013.11.1116

32. Lafuente H, Jaunarena I, Ansuategui E, Lekuona A, Izeta A. Cell therapy as a treatment of secondary lymphedema: a systematic review and meta-analysis. *Stem Cel Res Ther* (2021) **12**:578. doi:10.1186/s13287-021-02632-y

33. Chen K, Sinelnikov MY, Reshetov IV, Timashev P, Gu Y, Mu L, et al. Therapeutic potential of mesenchymal stem cells for postmastectomy lymphedema: a literature review. *Clin Translational Sci* (2021) **14**:54–61. doi:10.1111/cts.12864

34. Robering JW, Weigand A, Pfuhlmann R, Horch RE, Beier JP, Boos AM. Mesenchymal stem cells promote lymphangiogenic properties of lymphatic endothelial cells. *J Cell Mol Med* (2018) **22**:3740–50. doi:10.1111/jcmm.13590

35. Meçe O, Houbaert D, Sassano M-L, Durré T, Maes H, Schaaf M, et al. Lipid droplet degradation by autophagy connects mitochondria metabolism to Prox1-driven expression of lymphatic genes and lymphangiogenesis. *Nat Commun* (2022) **13**:2760. doi:10.1038/s41467-022-30490-6

36. Baker A, Kim H, Semple JL, Dumont D, Shoichet M, Tobbia D, et al. Experimental assessment of pro-lymphangiogenic growth factors in the treatment of post-surgical lymphedema following lymphadenectomy. *Breast Cancer Res* (2010) **12**:R70. doi:10.1186/bcr2638

37. Eppler SM, Combs DL, Henry TD, Lopez JJ, Ellis SG, Yi J-H, et al. A target-mediated model to describe the pharmacokinetics and hemodynamic effects of recombinant human vascular endothelial growth factor in humans. *Clin Pharmacol Ther* (2002) **72**:20–32. doi:10.1067/mcp.2002.126179

38. Fritz-Six KL, Dunworth WP, Li M, Caron KM. Adrenomedullin signaling is necessary for murine lymphatic vascular development. *J Clin Invest* (2008) **118**:40–50. doi:10.1172/jci33302

39. Jin DP, An A, Liu J, Nakamura K, Rockson SG. Therapeutic responses to exogenous VEGF-C administration in experimental lymphedema: immunohistochemical and molecular characterization. *Lymphatic Res Biol* (2009) **7**:47–57. doi:10.1089/lrb.2009.0002

40. Marino D, Angehrn Y, Klein S, Riccardi S, Baenziger-Tobler N, Otto VI, et al. Activation of the epidermal growth factor receptor promotes lymphangiogenesis in the skin. *J Dermatol Sci* (2013) **71**:184–94. doi:10.1016/j.jdermsci.2013.04.024

41. Szuba A, Skobe M, Karkkainen MJ, Shin WS, Beynet DP, Rockson NB, et al. Therapeutic lymphangiogenesis with human recombinant VEGF-C. *FASEB J* (2002) **16**:1985–7. doi:10.1096/fj.02-0401fje

42. Moya IM, Halder G. The Hippo pathway in cellular reprogramming and regeneration of different organs. *Curr Opin Cel Biol* (2016) **43**:62–8. doi:10.1016/j.ceb.2016.08.004

43. Driskill JH, Pan D. Control of stem cell renewal and fate by YAP and TAZ. *Nat Rev Mol Cel Biol* (2023) **24**:895–911. doi:10.1038/s41580-023-00644-5

44. Heng BC, Zhang X, Aubel D, Bai Y, Li X, Wei Y, et al. Role of YAP/TAZ in cell lineage fate determination and related signaling pathways. *Front Cel Dev Biol* (2020) **8**:735. doi:10.3389/fcell.2020.00735

45. Li Z, Feng J, Gou J, Jia J, Yi T, Cui T. Verteporfin, a suppressor of YAP-TEAD complex, presents promising antitumor properties on ovarian cancer. *OncoTargets Ther* (2016) **9**:5371–81. doi:10.2147/ott.s109979

46. Liu-Chittenden Y, Huang B, Shim JS, Chen Q, Lee S-J, Anders RA, et al. Genetic and pharmacological disruption of the TEAD-YAP complex suppresses the oncogenic activity of YAP. *Genes Dev* (2012) **26**:1300–5. doi:10.1101/gad.192856.112

47. Wei H, Wang F, Wang Y, Li T, Xiu P, Zhong J, et al. Verteporfin suppresses cell survival, angiogenesis and vasculogenic mimicry of pancreatic ductal adenocarcinoma via disrupting the YAP-TEAD complex. *Cancer Sci* (2017) **108**:478–87. doi:10.1111/cas.13138

48. Sierla R, Dylke ES, Kilbreath S. A systematic review of the outcomes used to assess upper body lymphedema. *Cancer Invest* (2018) **36**:458–73. doi:10.1080/07357907.2018.1517362

49. Byron JK, Graves TK, Becker MD, Cosman JF, Long EM. Evaluation of the ratio of collagen type III to collagen type I in periurethral tissues of sexually intact and neutered female dogs. *Am J Vet Res* (2010) **71**:697–700. doi:10.2460/ajvr.71.6.697

50. Singh D, Rai V, Agrawal DK. Regulation of collagen I and collagen III in tissue injury and regeneration. *Cardiol Cardiovasc Med* (2023) **7**:5–16. doi:10.26502/fccm.92920302

51. Kim H-Y, Im H-Y, Chang H-K, Jeong H, Park J-H, Kim H-I, et al. Correlation between collagen type I/III ratio and scar formation in patients undergoing immediate reconstruction with the round block technique after breast-conserving surgery. *Biomedicines* (2023) **11**:1089. Epub ahead of print 4 April 2023. doi:10.3390/biomedicines11041089

EBM Experimental Biology and Medicine

TYPE Original Research
PUBLISHED 23 September 2024
DOI 10.3389/ebm.2024.10155

*CORRESPONDENCE
Xi Li,
✉ xili19731973@sxmu.edu.cn

RECEIVED 02 March 2024
ACCEPTED 27 August 2024
PUBLISHED 23 September 2024

CITATION
Li X, Cui J, Wang L, Cao C and Liu H (2024) Integrated multi-omics profiling reveals the ZZZ3/CD70 axis is a super-enhancer-driven regulator of diffuse large B-cell lymphoma cell-natural killer cell interactions.
Exp. Biol. Med. 249:10155.
doi: 10.3389/ebm.2024.10155

Integrated multi-omics profiling reveals the ZZZ3/CD70 axis is a super-enhancer-driven regulator of diffuse large B-cell lymphoma cell-natural killer cell interactions

Xi Li *, Juya Cui, Liao Wang, Caihong Cao and Hu Liu

Cancer Center, Shanxi Bethune Hospital, Shanxi Academy of Medical Sciences, Tongji Shanxi Hospital, Third Hospital of Shanxi Medical University, Taiyuan, Shanxi, China

Abstract

Tumor immune microenvironment is crucial for diffuse large B-cell lymphoma (DLBCL) development. However, the mechanisms by which super-enhancers (SEs) regulate the interactions between DLBCL cells and tumor-infiltrating immune cells remains largely unknown. This study aimed to investigate the role of SE-controlled genes in regulating the interactions between DLBCL cells and tumor-infiltrating immune cells. Single-cell RNA-seq, bulk RNA-seq and H3K27ac ChIP-seq data were downloaded from the Heidelberg Open Research Data database and Gene Expression Omnibus database. HOMER algorithm and Seurat package in R were used for bioinformatics analysis. Cell proliferation and lactate dehydrogenase (LDH) release was detected by MTS and LDH release assays, respectively. Interaction between B cell cluster and $CD8^+$ T cell and NK cell cluster was most obviously enhanced in DLBCL, with CD70-CD27, MIF-CD74/CXCR2 complex, MIF-CD74/CD44 complex and CCL3-CCR5 interactions were significantly increased. NK cell sub-cluster showed the strongest interaction with B cell cluster. ZZZ3 upregulated the transcription of *CD70* by binding to its SE. Silencing CD70 in DOHH2 cells significantly promoted the proliferation of co-cultured NK92 cells and LDH release from DOHH2 cells, which was counteracted by ZZZ3 overexpression in DOHH2 cells. CD70 silencing combined with PD-L1 blockade promoted LDH release from DOHH2 cells co-cultured with NK92 cells. In conclusion, DLBCL cells inhibited the proliferation and killing of infiltrating NK cells by regulating ZZZ3/CD70 axis. Targeting ZZZ3/CD70 axis combined with PD-L1 blockade is expected to be a promising strategy for DLBCL treatment.

KEYWORDS

diffuse large B-cell lymphoma, cell interaction, super-enhancer, natural killer cell, CD70

Impact statement

In this study, we found that CD70 was a super-enhancer-controlled gene that was driven by ZZZ3 for transcription in diffuse large B-cell lymphoma cells. The ZZZ3/CD70 axis in diffuse large B-cell lymphoma cells inhibited infiltrating natural killer cell killing and proliferation, thereby promoting immune evasion of diffuse large B-cell lymphoma cells. The ZZZ3/CD70 axis has the potential to be a novel immunotherapy target for diffuse large B-cell lymphoma. Targeting ZZZ3/CD70 axis combined with PD-L1 blockade is expected to be a promising immunotherapeutic strategy for the treatment of diffuse large B-cell lymphoma.

Introduction

Diffuse large B-cell lymphoma (DLBCL) is the most common B-cell non-Hodgkin lymphoma with highly heterogeneous and aggressiveness [1, 2]. Although therapeutic strategies such as chemotherapy, radiotherapy and immunotherapy have improved the survival of DLBCL patients, the prognosis remains generally dismal for patients developing relapsed or refractory DLBCL [3, 4]. Identification of novel therapeutic targets is essential to improve the outcomes of patients with DLBCL. Understanding the pathogenesis of DLBCL could facilitate the development of novel molecular therapeutic targets.

Interactions between tumor cells and tumor-infiltrating immune cells in the tumor microenvironment (TME) could either induce tumor suppression or promote tumor development [5–7]. For example, ligands on the surface of tumor cells, such as programmed death-ligand 1 (PD-L1), major histocompatibility complex class II (MHC-II), fibrinogen-like protein 1 (FGL1) and galectin-9 (Gal-9), interact with the inhibitory receptors of immune effector cells, such as programmed cell death protein 1 (PD-1), lymphocyte-activation gene 3 (LAG-3) and T cell immunoglobulin and mucin domain 3 (TIM3), to inhibit cytotoxicity of immune cells and promote tumor immune evasion [8–10]. The complex interactions between tumor cells and various tumor-infiltrating immune cells are involved in regulating the immunosuppressive microenvironment of DLBCL [11–13]. Compared with solid tumors, DLBCL has a higher abundance of infiltrating immune cells in the TME [6, 7]. However, interactions between DLBCL cells and tumor-infiltrating immune cells are still not well characterized.

Recently, single-cell RNA sequencing (scRNA-seq) technology has become an important tool for studying the lymphoma microenvironment, revealing the high heterogeneity of tumor cells and their interactions with immune cells. For instance, Roider et al. used scRNA-seq to study DLBCL and shed light on the heterogeneity of nodal B-cell lymphomas, emphasizing its relevance to personalized cancer therapy [14]. Additionally, Steen et al. elucidated the DLBCL microenvironment at a systems-level resolution and identified potential therapeutic targets by integrating multiple scRNA-seq datasets [15]. Despite these systematic insights into lymphoma microenvironment heterogeneity, the epigenetic regulatory mechanisms governing communication between tumor cells and microenvironment cells remain elusive.

Aberrant epigenetic alterations regulate the phenotype of tumor cells, and participate in the remodeling of tumor immune microenvironment by affecting the interactions between tumor cells and infiltrating immune cells [16–18]. Super-enhancer (SEs) are large spatially clustered transcriptionally active enhancers, typically spanning several kilobases, that can be predicted by strong occupancy signals of specific histone modifications such as H3K27 acetylation (H3K27ac) [19–21]. Enhancer components in SEs are functionally non-redundant which act in a synergistic or additive manner, enabling SEs to drive target genes transcription more robustly than typical enhancers [22–24]. SEs combine with transcription factors to powerfully drive the transcription of genes that control and define cell identity [21]. SEs and master transcription factors that regulate target gene expression are essential for DLBCL progression [25, 26]. However, the precise mechanisms by which SEs regulate the interactions between DBLCL cells and tumor-infiltrating immune cells remain elusive.

This study aimed to investigate the key regulators controlled by SEs in DLBCL cells that regulate the interactions between DLBCL cells and tumor-infiltrating immune cells. We analyzed immune cell clusters with significantly enhanced interactions with B cell cluster in DLBCL. Ligand-receptor interactions of B cell cluster and infiltrating immune cell clusters were identified. Subsequently, we identified SE-controlled ligand-encoding gene and its transcription factor. Finally, we explored the effects of the SE-controlled ligand-encoding gene and its transcription factor in DLBCL cells escape from natural killer (NK) cell killing *in vitro*. This study is expected to provide new therapeutic targets for the treatment of DLBCL.

Materials and methods

Single-cell RNA sequencing (scRNA-seq) data analysis

The scRNA-seq gene expression matrix of DLBCL and reactive non-malignant lymph node (rLN) samples were downloaded from the Heidelberg Open Research Data database (heiDATA,[1]) under accession code VRJUNV [14], and the Gene Expression Omnibus database (GEO,[2]) under

---

[1] https://heidata.uni-heidelberg.de/

[2] http://www.ncbi.nlm.nih.gov/geo/

accession code GSE182434 [15]. Uniform manifold approximation and projection (UMAP) dimensionality reduction analysis of scRNA-seq data was conducted using the "RunUMAP" in R package "Seurat" to generate 2D plots to visualize cell clusters and sub-clusters [27]. Cell clusters and sub-clusters were annotated according to the well-recognized cell-specific markers using CellMarker 2.0 web tool[3] [28]. The number and strength of interactions among cell clusters or sub-clusters were evaluated using the CellChat v1.6.1.

Chromatin immunoprecipitation followed by sequencing (ChIP-seq) data analysis

H3K27ac ChIP-seq data of 28 DLBCL cell lines were downloaded from the GSE182214 dataset [25]. Enhancers were defined as the H3K27ac-enriched regions using the "findPeaks" tool in HOMER algorithm. Enhancer constituents clustered within 12.5 kb were stitched together. The "super enhancer" tool in HOMER algorithm was used to rank enhancers according to the H3K27ac signals. Threshold for SE screening was the tangent slope >1 for the rank ordered set. To define the SE-controlled gene, the "annotatePeaks" tool in HOMER algorithm was used to assign enhancers to the nearest genes on the genome. H3K27ac signals at the *CD70* locus were visualized using the UCSC Genome Browser database[4].

Survival and immune score analysis

Bulk transcriptomic data and clinical information of 928 DLBCL patients were downloaded from the GSE117556 dataset [29]. Overall survival (OS) and progression-free survival (PFS) of DLBCL patients was assessed by Kaplan-Meier analysis and log-rank test using the X-tile software. Log-rank test $P < 0.05$ indicated a significant difference. The immune score within the bulk transcriptomic data was calculated using both the CIBERSORT and xCell algorithms. Subsequently, Pearson's analysis was employed to assess the correlation between MIF, CCL3 and CD70 expression levels and the immune scores.

Prediction of transcription factor binding sites

Transcription factor binding sites for *CD70* were predicted using the Cistrome Data Browser database[5] [30, 31].

Cell culture

The human DLBCL cell line, DOHH2, was purchased from MeisenCTCC (Zhejiang, China) and cultured in RPMI 1640 medium (Gibco, MA, United States) with 10% fetal bovine serum (FBS; Sigma-Aldrich, MO, United States) and 1% penicillin/streptomycin (Invitrogen, CA, United States) at 37°C with 5% CO_2.

The human NK cell line, NK92, was acquired from American Type Culture Collection (ATCC; VA, United States). NK92 cells were cultured in complete RPMI 1640 medium at 37°C with 5% CO_2, and activated with 200 U/mL interleukin-2 (IL-2; Sigma-Aldrich, MO, United States).

JQ1 treatment

DOHH2 cells were seeded into 96-well plates at density of 2×10^3 cells per well and cultured at 37°C for 48 h. The bromodomain and extra-terminal domain (BET) inhibitor JQ1 (Solarbio, Beijing, China) was added into each well to the indicated concentrations (0 or 1 μM) and incubated for 24 h.

Cell transfection

Small interfering RNAs (siRNAs) targeting CD70 (siCD70) and ZZZ3 (siZZZ3), and negative control siRNA (siNC) were obtained from GenePharma (Shanghai, China). The eukaryotic plasmid pcDNA3.1 for ZZZ3 overexpression (OE-ZZZ3) and the empty pcDNA3.1 plasmid (OE-NC) were synthesized by GenePharma (Shanghai, China). DOHH2 cells were seeded into 6-well plates and cultured until the cell confluency reached approximately 80%. Cell transfection was conducted using Lipofectamine 3000 (Invitrogen, CA, United States) according to the manufacturer's instructions.

RNA isolation and quantitative real-time PCR (qRT-PCR)

Total RNA of DOHH2 cells was isolated using TRIzol reagent (Invitrogen, CA, United States) according to the manufacturer's instructions. cDNA was generated with 500 ng RNA per reaction using the PrimeScript™ RT Master Mix (Takara, Tokyo, Japan). Quantitative PCR (qPCR) was performed with SYBR Green Master Mix (Takara, Tokyo, Japan). Relative expression levels of CD70 and ZZZ3 were calculated by the $2^{-\Delta\Delta CT}$ formula with GAPDH as the internal reference. Primers to amplify genes are listed as follows:

CD70, forward: 5′-GACCCCAGGCTATACTGGCA-3′; reverse: 5′-CAGGCTGATGCTACGGGAG-3'.

ZZZ3, forward: 5′-AAACGAGCTTGTCGATGTCTT-3′; reverse: 5′-GACAGCCAAATAGCCTGTGAT-3′.

---

[3] http://bio-bigdata.hrbmu.edu.cn/CellMarker/index.html

[4] http://genome.ucsc.edu/

[5] http://dbtoolkit.cistrome.org

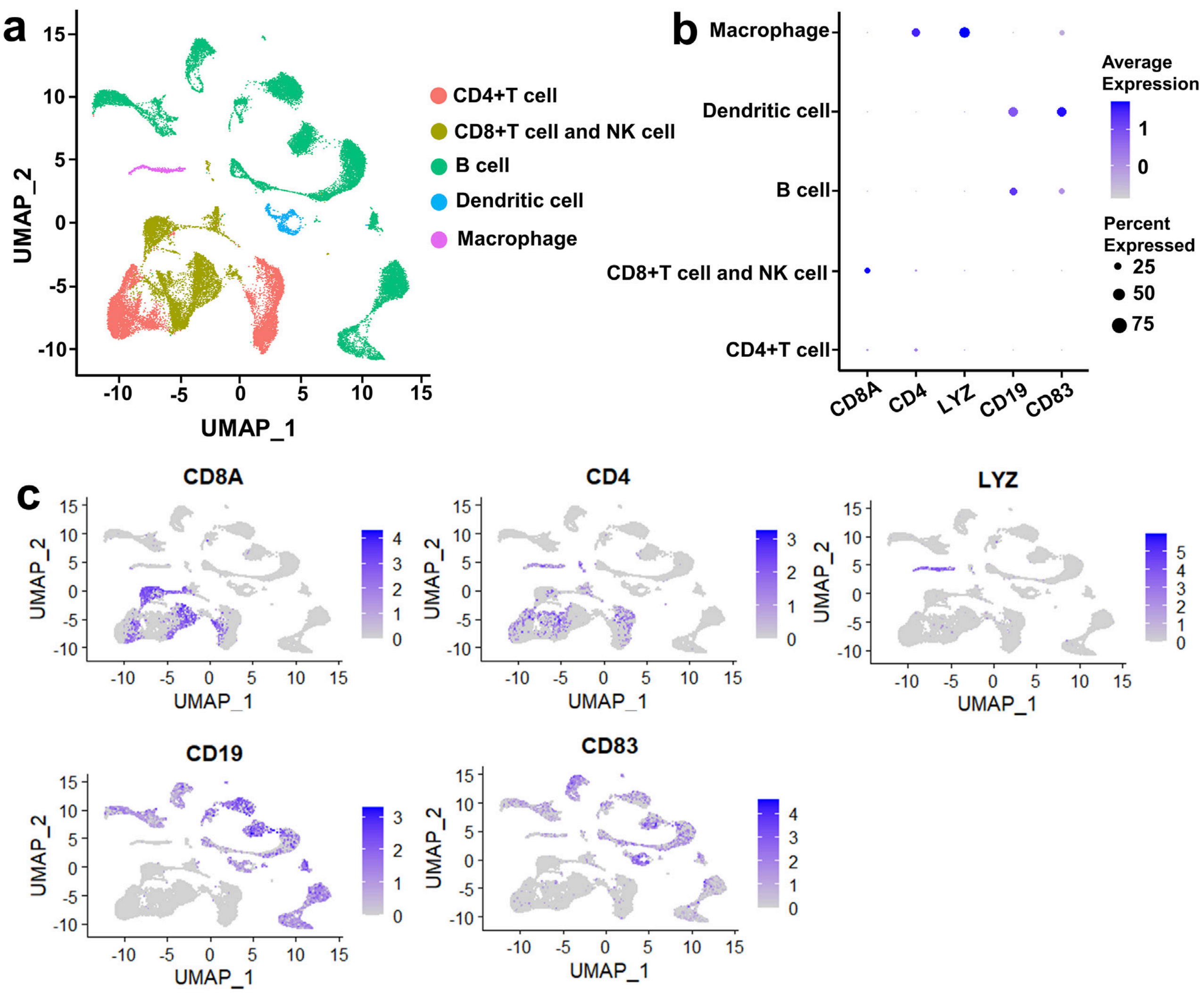

FIGURE 1
Five cell clusters were identified in DLBCL and rLN based on the VRJUNV and GSE182434 datasets. **(A)** dimensionality reduction was performed by UMAP. **(B)** Dot plots depicting the expression levels of cell-specific markers in each cell cluster, as well as the expression percentage of the markers. **(C)** Feature plots showed the expression of cell-specific markers in global cell clusters.

GAPDH, forward: 5′-GGAGCGAGATCCCTCCAAAAT-3′; reverse: 5′-GGCTGTTGTCATACTTCTCATGG-3′.

ChIP-qPCR

DOHH2 cells were fixed with 1% formaldehyde for 10 min at 25°C and quenched with 0.125 M glycine for 5 min. Cells were lysed with SDS lysis buffer for 10 min at 4°C, and then sonicated using a M220 Focused-ultrasonicator (Covaris, MA, United States) for 10 min in 0.5 min pulse intervals. The ultrasound products were incubated with anti-H3K27ac (ab4729, abcam, United States) or IgG (ab172730, abcam, United States) at 4°C overnight. The immunoprecipitated DNA was purified using the DNA Purification Kit (Beyotime, Shanghai, China), and then subjected to qPCR reactions. Primers used for ChIP-qPCR are listed as follows:

CD70-SE1, forward: 5′-CTGCCAGTGGAAGTGTTTGC-3′; reverse: 5′-ACGTCAGAAGTGCAGCCTTT-3′.

CD70-SE2, forward: 5′-CACGGACGTAAGCAGAGAGG-3′; reverse: 5′-TTTGCAGCGTAGAGAGTCCG-3′.

CD70-SE3, forward: 5′-TTCACTGAAGTGCCTCCGAC-3′; reverse: 5′-TGACAGTTTGAGATGCCCCC-3′.

Cell proliferation assay for DLBCL cells

Cell proliferation of DOHH2 cells was determined using an MTS Assay Kit (abcam, United States). DOHH2 cells were

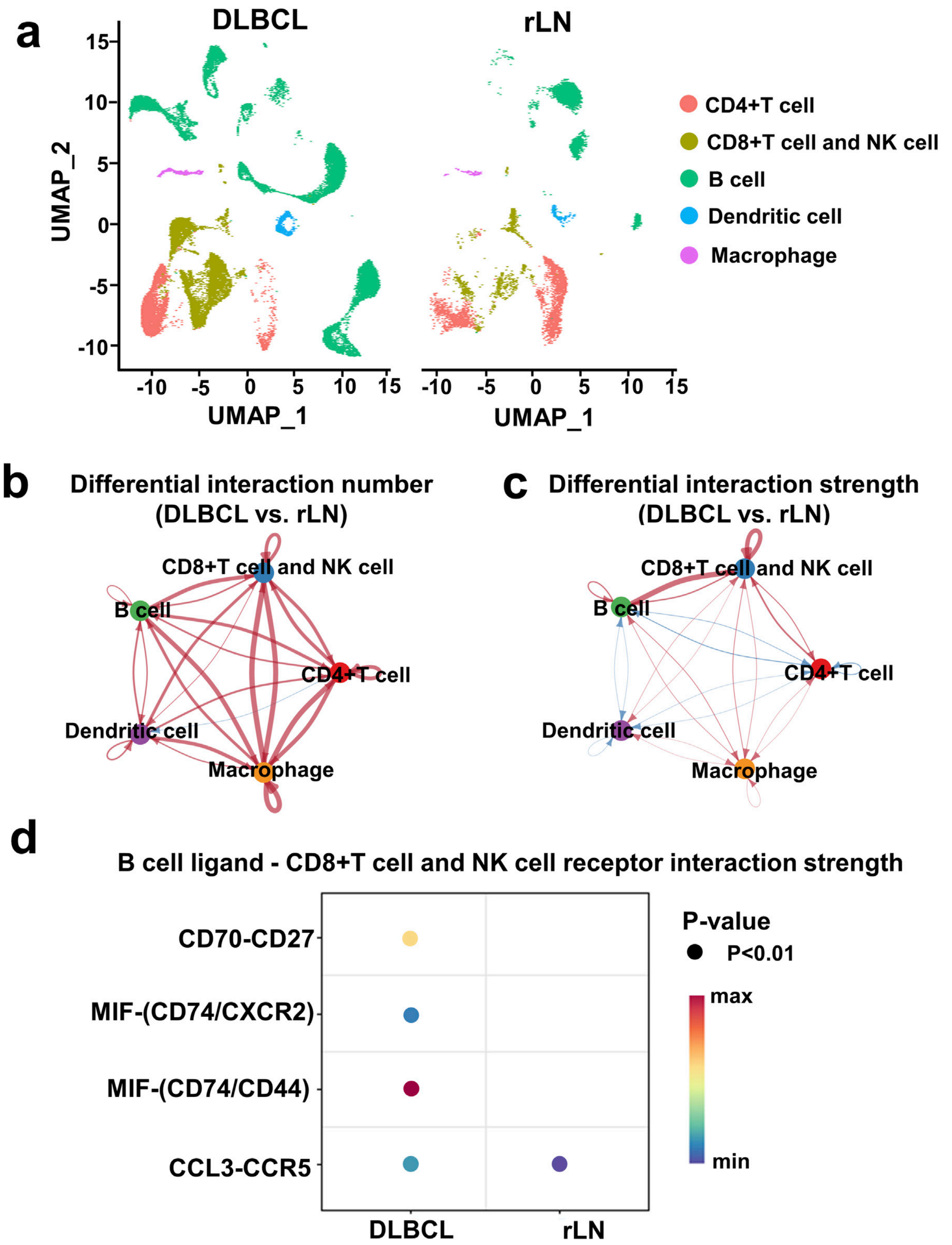

FIGURE 2
Interaction analysis of five cell clusters in DLBCL compared with rLN based on the VRJUNV and GSE182434 datasets. **(A)** UMAP plots of five cell clusters in DLBCL and rLN were analyzed respectively. **(B, C)** Networks of differential interaction numbers **(B)** and strengths **(C)** in DLBCL compared with rLN. Red lines represented upregulation of interaction number or strength in DLBCL compared with rLN, while blue lines represented downregulation. The thicker the line, the greater difference in the interaction number or strength. **(D)** Dot plots of B cell ligands and CD8$^+$ T cell and NK cell receptors interactions that were significantly different between DLBCL and rLN.

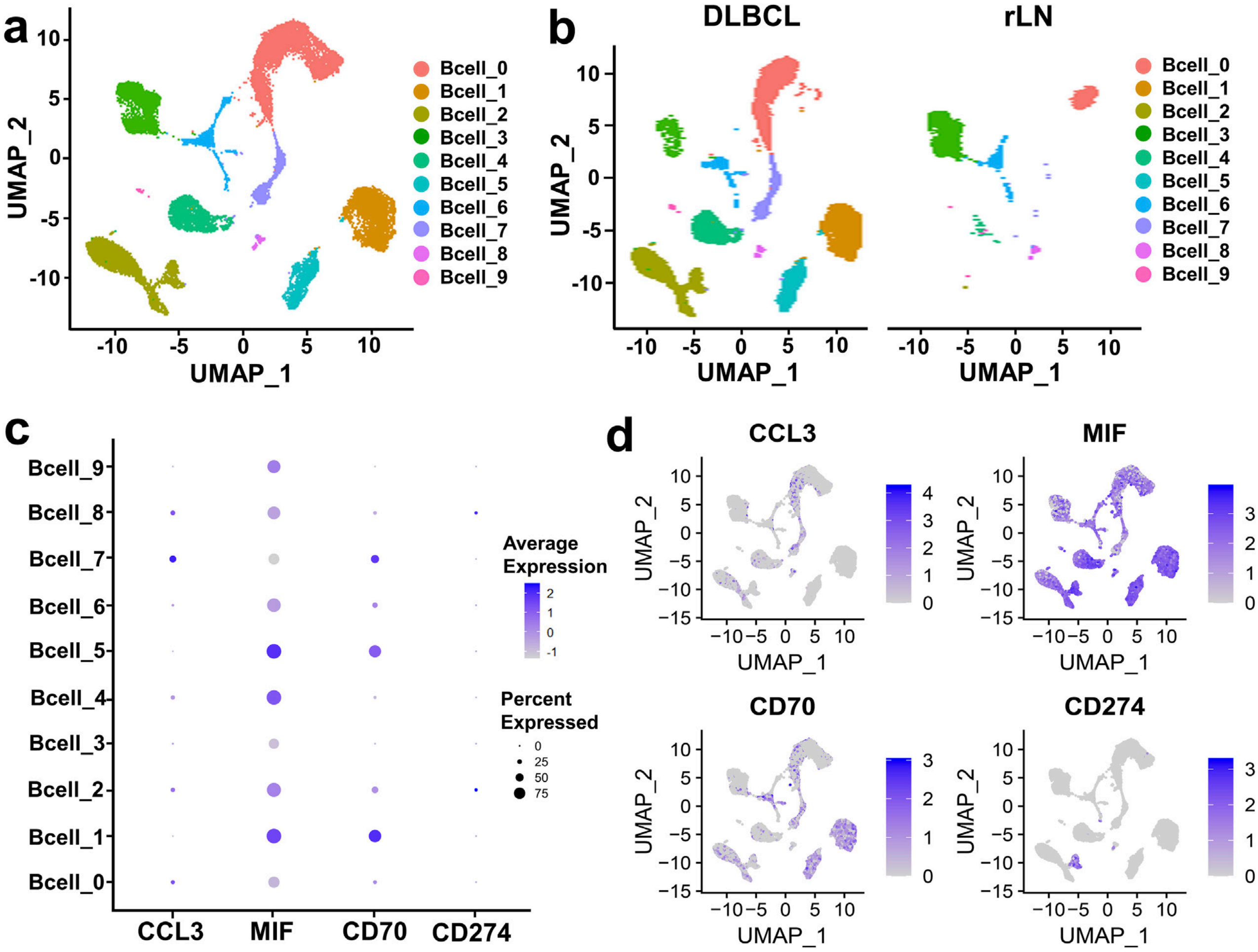

FIGURE 3
Expression and distribution analysis of CCL3, MIF, CD70, and CD274 in the ten B cell sub-clusters based on the VRJUNV and GSE182434 datasets. **(A)** UMAP plots of the ten sub-clusters of B cell cluster in DLBCL and rLN. **(B)** UMAP dimensionality reduction plots for DLBCL and rLN, respectively. **(C)** Dot plots of the expression levels and percentages of CCL3, MIF, CD70, and CD274 in the ten B cell sub-clusters. **(D)** Feature plots of the distribution of CCL3, MIF, CD70, and CD274 expression in B cell cluster.

seeded into 96-well plates with 1 × 10^4 cells per well, and cultured for 0, 1, 2, and 3 days. 10 μL MTS reagent was added into each well at each time point and incubated for 4 h at 37°C. Absorbance at 490 nm (A_{490}) was detected using a microplate reader (Bio-Rad, CA, United States).

Cell proliferation assay for NK cells

NK92 cells were precultured with 200 U/mL IL-2 for activation. DOHH2 cells were treated with 25 μg/mL mitomycin C for 1 h at 37°C to prevent cell proliferation. Mitomycin C pretreated DOHH2 cells were co-cultured with activated NK92 cells at a ratio of 1:1, 2:1 and 5:1 in RPMI 1640 medium for 48 h. Proliferation of NK92 cells was determined using an MTS Assay Kit (abcam, United States) according to the manufacturer's instructions. A_{490} was detected using a microplate reader (Bio-Rad, CA, United States).

Lactate dehydrogenase (LDH) release assay

DOHH2 cells were co-cultured with IL-2 activated NK92 cells as indicated ratios for 48 h. The co-culture systems were treated with or without anti-PD-L1 (ab205921, abcam, United States) or IgG (ab172730, abcam, United States). LDH release were measured using the Cytotoxicity LDH Assay Kit-WST (Dojindo, Kyushu, Japan) according to the manufacturer's instructions. Absorbance at 490 nm was detected using a microplate reader (Bio-Rad, CA, United States).

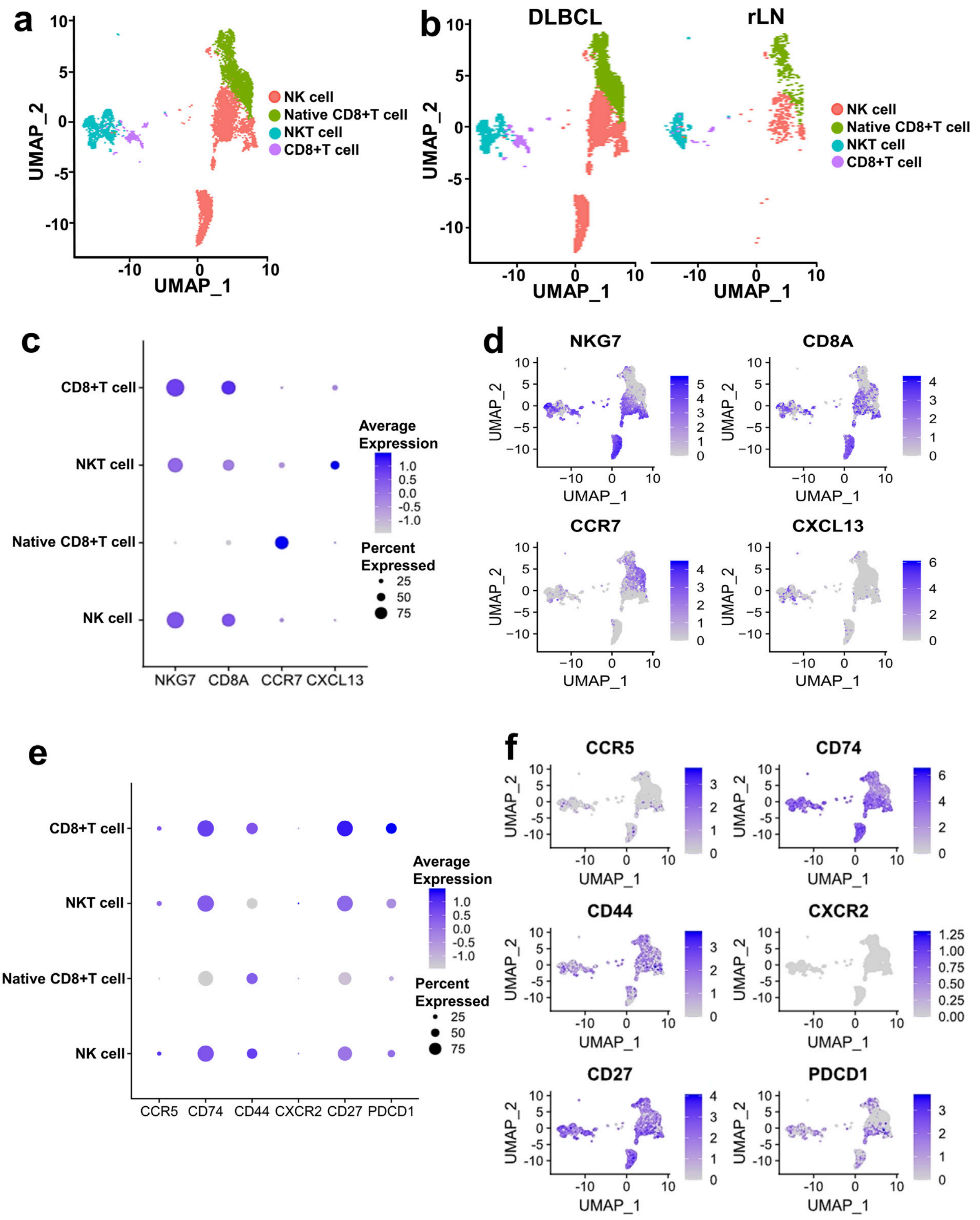

FIGURE 4
Expression and distribution analysis of CCR5, CD74, CD44, CXCR2, CD27, and PDCD1 in the four sub-clusters of CD8$^+$ T cell and NK cell cluster based on the VRJUNV and GSE182434 datasets. **(A)** UMAP plots of the distribution of the four sub-clusters of CD8$^+$ T cell and NK cell cluster (NK cell sub-cluster, native CD8$^+$ T cell sub-cluster, NKT cell sub-cluster, and CD8$^+$ T cell sub-cluster) in DLBCL and rLN. **(B)** UMAP plots of NK cell, native CD8$^+$ T cell, NKT cell, and CD8$^+$ T cell sub-clusters distribution in DLBCL and rLN, respectively. **(C)** Dot plots of specific marker genes expression in the four sub-clusters of CD8$^+$ T cell and NK cell cluster together with the expression percentage of the marker genes. **(D)** Feature plots of specific

(Continued)

FIGURE 4 (Continued)
marker genes expression in the four sub-clusters of CD8$^+$ T cell and NK cell cluster. **(E)** Expression levels and percentages of CCR5, CD74, CD44, CXCR2, CD27, and PDCD1 in the four sub-clusters. **(F)** Distribution of CCR5, CD74, CD44, CXCR2, CD27, and PDCD1 expression in the CD8$^+$ T cell and NK cell cluster.

Statistical analysis

Statistical data were analyzed using R software (version 4.1.2) and GraphPad Prism (version 9.0), and presented as mean ± standard deviation (SD). Differences among multiple groups were analyzed by one-way analysis of variance (ANOVA) followed by Tukey's *post hoc* test. Differences between two groups were analyzed by Student's *t*-test. $P < 0.05$ indicated a statistical significance.

Results

Five cell clusters were identified in DLBCL and rLN

Immune microenvironment plays a crucial role in the tumorigenesis of DLBCL. To describe the heterogeneity of the immune microenvironment in DLBCL, we performed UMAP dimensionality reduction on DLBCL and rLN samples according to the VRJUNV and GSE182434 datasets. Dimensionality reduction by UMAP resulted in five cell clusters, including CD4-expressing (CD4$^+$) T cell cluster, CD8-expressing (CD8$^+$) T cell and NK cell cluster, B cell cluster, dendritic cell cluster, and macrophage cluster (Figure 1A). The five cell clusters were identified by unique cell-specific marker genes expression as follow: CD8A for CD8$^+$ T cells and NK cells, CD4 for CD4$^+$ T cells, LYZ for macrophages, CD19 for B cells, and CD83 for dendritic cells (Figure 1B). Subsequently, these clusters were reclassified into global cellular compartments based on the expression of cell-specific markers (Figure 1C). Taken together, five cell clusters, including CD4$^+$ T cell cluster, CD8$^+$ T cell and NK cell cluster, B cell cluster, dendritic cell cluster, and macrophage cluster, were identified in DLBCL and rLN.

The enhanced interaction of B cell cluster to CD8$^+$ T cell and NK cell cluster was most prominent in DLBCL compared with rLN

To investigate DLBCL-specific immune cell interactions, we described immune cell clusters in DLBCL and rLN respectively (Figure 2A). Subsequently, we analyzed the differences in the number and strength of cell cluster interactions between DLBCL and rLN. The interaction numbers of B cell cluster to the other four cell clusters (CD4$^+$ T cell cluster, CD8$^+$ T cell and NK cell cluster, dendritic cell cluster, and macrophage cluster) were increased in DLBCL compared with rLN (Figure 2B). The interaction strengths of B cell cluster to CD4$^+$ T cell cluster and dendritic cell cluster were attenuated in DLBCL compared with rLN (Figure 2C). However, the interaction strengths of B cell cluster to macrophage cluster and CD8$^+$ T cell and NK cell cluster were enhanced in DLBCL compared with rLN (Figure 2C). Especially, the interaction strength of B cell cluster to CD8$^+$ T cell and NK cell cluster was most dramatically enhanced in DLBCL compared with rLN (Figure 2C). Furthermore, we analyzed the differential interactions between B cell ligands and CD8$^+$ T cell and NK cell receptors in DLBCL and rLN. A total of four pairs of ligand-receptor interactions (including CD70-CD27, MIF-CD74/CXCR2 complex, MIF-CD74/CD44 complex, and CCL3-CCR5) were significantly upregulated in DLBCL compared with rLN (Figure 2D). Collectively, these findings suggested that the enhanced interaction of B cell cluster to CD8$^+$ T cell and NK cell cluster was most prominent in DLBCL compared with rLN.

Strong interaction was found between B cell cluster and NK cell sub-cluster in DLBCL

To further investigate the interaction of B cell cluster with CD8$^+$ T cell and NK cell cluster, we classified B cell cluster into ten sub-clusters based on the VRJUNV and GSE182434 datasets (Figure 3A). Dimensionality reduction was performed on B cell sub-clusters of DLBCL and rLN, respectively (Figure 3B). Then, we analyzed the expression of ligand-encoding genes in the upregulated ligand-receptor interaction pairs. CD70 was mainly expressed in Bcell_1, Bcell_2, Bcell_5, Bcell_6 and Bcell_7 sub-clusters; CCL3 was mainly expressed in Bcell_0, Bcell_2, Bcell_4, Bcell_7 and Bcell_8 sub-clusters; MIF was expressed in all of the ten sub-clusters (Figures 3C, D). Additionally, we analyzed the expression of *CD274* (PD-L1 encoding gene) in each B cell sub-cluster. The results showed that *CD274* was mainly expressed in Bcell_2 and Bcell_8 sub-clusters (Figures 3C, D).

CD8$^+$ T cell and NK cell cluster of DLBCL and rLN was classified into four sub-clusters including NK cell sub-cluster, native CD8$^+$ T cell sub-cluster, NKT cell sub-cluster, and CD8$^+$

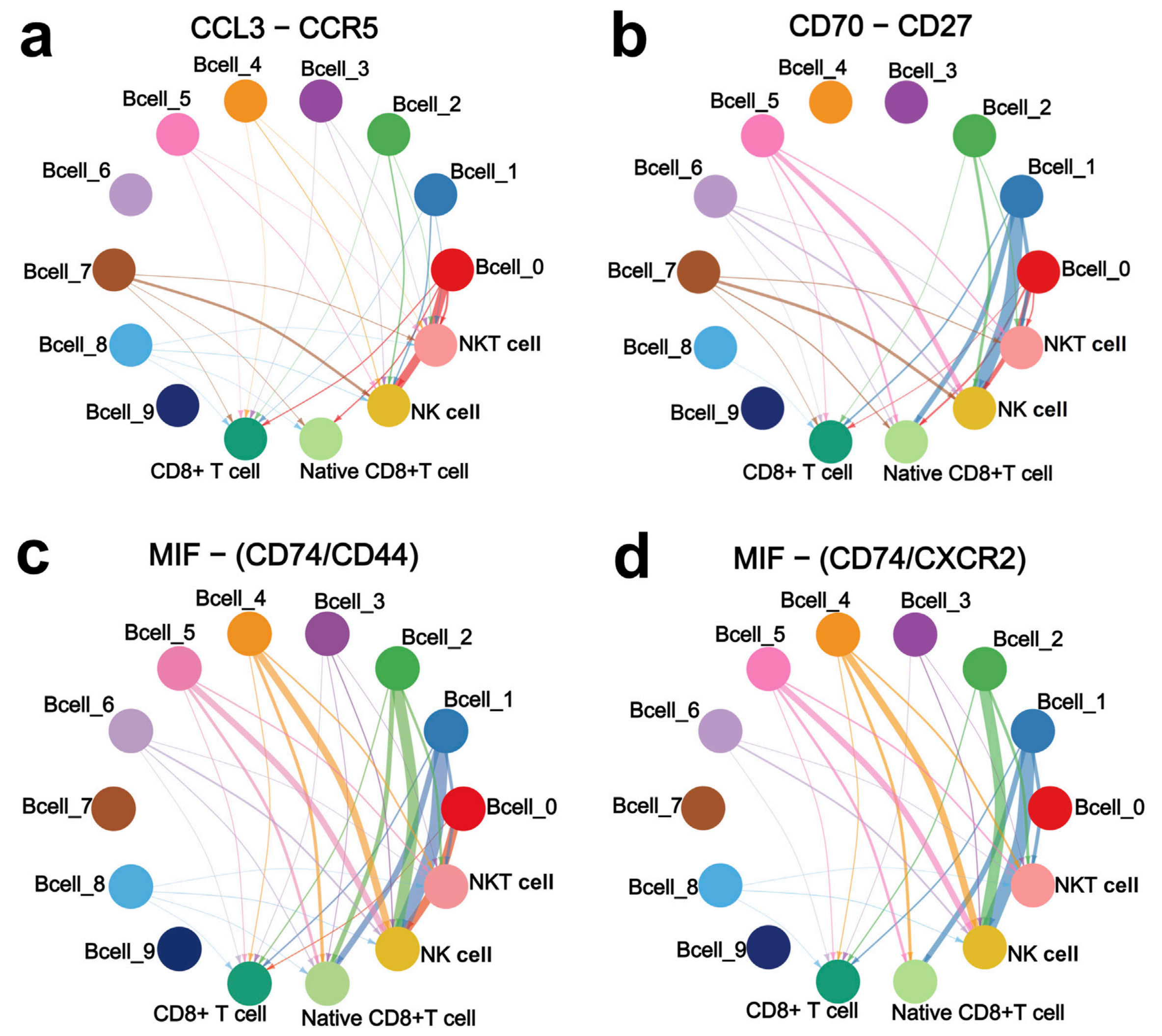

FIGURE 5
CCL3-CCR5 **(A)**, CD70-CD27 **(B)**, MIF-CD74/CD44 complex **(C)**, and MIF-CD74/CXCR2 complex **(D)** interaction networks of the ten B cell sub-clusters with NK cell, native CD8$^+$ T cell, NKT cell, and CD8$^+$ T cell sub-clusters. Interaction networks were constructed based on the VRJUNV and GSE182434 datasets. The thicker the line, the stronger the interaction.

T cell sub-cluster (Figures 4A, B). We calculated the expression distribution of specific marker genes of the four sub-clusters: NKG7 for NK cells, CD8A for CD8$^+$ T cells, CCR7 for native CD8$^+$ T cells, and CXCL13 for NKT cells (Figures 4C, D). These results indicated that we obtained reliable annotations of sub-clusters of CD8$^+$ T cell and NK cell cluster. Then, we analyzed the expression of receptor-encoding genes in the upregulated ligand-receptor interaction pairs. CD27, CD74 and CCR5 were mainly expressed in NK cell sub-cluster, NKT cell sub-cluster, and CD8$^+$ T cell sub-cluster (Figures 4E, F). CD44 was mainly expressed in NK cell sub-cluster, native CD8$^+$ T cell sub-cluster, and CD8$^+$ T cell sub-cluster (Figures 4E, F). CXCR2 was mainly expressed in NKT cell sub-cluster (Figures 4E, F). PD1-encoding gene, *PDCD1*, was mainly expressed in NK cell sub-cluster, NKT cell sub-cluster, and CD8$^+$ T cell sub-cluster (Figures 4E, F).

Furthermore, we analyzed the interactions of the four upregulated interacting ligand-receptor pairs between the ten B cell sub-clusters and the four CD8$^+$ T cell and NK cell sub-clusters. CCL3 and CCR5 showed strong interactions in Bcell_0 and Bcell_7 sub-clusters to NK cell sub-cluster (Figure 5A). CD70 and CD27 showed strong interactions in Bcell_1, Bcell_2, Bcell_5 and Bcell_7 sub-clusters to NK cell sub-cluster (Figure 5B). Interactions of MIF to CD74/CD44 receptor complex were strong in Bcell_0, Bcell_1, Bcell_2, Bcell_4 and Bcell_5 sub-clusters to NK cell sub-cluster (Figure 5C). Interactions of MIF to CD74/CXCR2 receptor complex were strong in Bcell_1, Bcell_2, Bcell_4 and Bcell_5 sub-clusters to NK cell sub-cluster (Figure 5D). Importantly, CCL3-CCR5, CD70-CD27, MIF-CD74/CD44 complex, and MIF-CD74/CXCR2 complex interacted more strongly between B cell cluster and NK cell sub-cluster than interactions between B cell cluster and native $CD8^+$ T cell sub-cluster, NKT cell sub-cluster, or $CD8^+$ T cell sub-cluster (Figure 5).

To further validate the impact of MIF, CCL3 and CD70 expression on the prognosis of DLBCL patients, we analyzed bulk transcriptomic data from the GSE117556 dataset. High MIF expression indicated lower OS, but showed no significant difference in PFS (Supplementary Figures S1A, B). Low CCL3 expression was associated with worse PFS, but OS did not show any statistical difference (Supplementary Figures S1C, D). Patients with high CD70 expression exhibited significantly worse OS and PFS compared to those with low CD70 expression (Supplementary Figures S1E, F). Additionally, immune scores were calculated based on bulk transcriptomic data using CIBERSORT and xCell algorithms. Pearson's analysis was performed to correlate the immune scores with MIF, CCL3 and CD70 expression levels. Integrating the results of the two algorithms, we found that MIF had the strongest correlation with B cell immune scores, while CCL3 correlated most strongly with $CD8^+$ T cells and macrophages (Supplementary Figure S2). CD70 showed the strongest correlation with $CD8^+$ T cells, but the correlation coefficient was relatively low ($R < 0.3$) (Supplementary Figure S2). Unfortunately, we did not find a significant correlation between MIF, CCL3 and CD70 with NK cell immune scores (Supplementary Figure S2).

Taken together, the interaction between B cell cluster and NK cell sub-cluster was the strongest in DLBCL, and this interaction may have potential clinical significance. Therefore, we focused on this interaction for further investigation.

CD70 was identified as a SE-controlled gene in DOHH2, HBL1, and NU-DHL1 cells

SEs are key factors driving oncogene expression in tumor cells [22–24]. We wondered whether the expression of CD70, MIF and CCL3 in DLBCL cells is regulated by SEs. H3K27ac signals at the *CCL3*, *CD70* and *MIF* loci in 28 DLBCL cell lines were analyzed based on ChIP-seq data from the GSE182214 dataset. The results showed that SE was present at the *CCL3*, *CD70* or *MIF* locus in 3 DLBCL cell lines, whereas it was absent in the other 25 cell lines (Figure 6A). HBL1, NU-DHL1 and DOHH2 cells were found to exhibit SE only at the *CD70* locus, but not at the *MIF* and *CCL3* loci (Figure 6B). The 3 cell lines were ranked in descending order according to the H3K27ac peak score for SE at the *CD70* locus as follows: DOHH2, HBL1, and NU-DHL1 cells (Figure 6B). We identified SE at the *CD70* locus in DOHH2, HBL1 and NU-DHL1 cells based the GSE182214 dataset. SE of *CD70* was divided into three regions (SE1, SE2, and SE3) based on the enrichment of H3K27ac signals (Figure 6C). Since DOHH2 cells had the highest H3K27ac peak score for SE of *CD70*, we validated the SE regions at the *CD70* locus in DOHH2 cells using ChIP-qPCR. H3K27ac in SE1, SE2 and SE3 regions was significantly enriched in DOHH2 cells (Figure 6D). JQ1 treatment significantly inhibited H3K27ac enrichment in the three SE regions (Figure 6D), and significantly downregulated *CD70* transcription in DOHH2 cells (Figure 6E). Collectively, CD70 was identified as a SE-controlled gene in DLBCL cells.

ZZZ3 interacted with the SE of CD70 to drive CD70 expression

SEs driving transcription of target genes must be recognized and bound by transcription factors [21]. Potential transcription factors regulating *CD70* were ranked in descending order according to the peak set overlap score, with ZZZ3 ranking first (Figure 7A). We successfully established ZZZ3-silenced cells by transfecting siZZZ3 into DOHH2 cells (Figure 7B). Silencing ZZZ3 significantly inhibited H3K27ac enrichment in SE1, SE2 and SE3 regions of the *CD70* locus in DOHH2 cells (Figure 7C). Moreover, silencing ZZZ3 significantly suppressed *CD70* transcription in DOHH2 cells (Figure 7D). DLBCL patients with high-ZZZ3 expression have significantly worse OS than patients with low-ZZZ3 expression (Figure 7E). High-ZZZ3 expression is associated with a poor PFS of DLBCL, although not significantly (descriptive Log-rank $P > 0.05$; Figure 7F). Taken together, ZZZ3 bound to SE of *CD70* to drive *CD70* transcription.

The ZZZ3/CD70 axis in DLBCL cells promoted their escape from NK cell killing

To investigate the impact of the ZZZ3/CD70 axis on DLBCL cell proliferation, we established CD70-silenced and ZZZ3-overexpressing cells by transfecting siCD70 or ZZZ3 overexpression plasmids (OE-ZZZ3) into DOHH2 cells, respectively. Transfection of siCD70 significantly inhibited CD70 expression in DOHH2 cells (Figure 8A). Compared with the DOHH2 cells transfected with the empty pcDNA3.1 plasmids (OE-NC), ZZZ3 expression was significantly upregulated in DOHH2 cells transfected with OE-ZZZ3 (Figure 8B). The effect of CD70 silencing on the proliferation of DOHH2 cells was determined by MTS assay. Silencing CD70 had no significant effect on the proliferation of DOHH2 cells (Figure 8C).

To investigate the impact of the ZZZ3/CD70 axis in DLBCL cells on their resistance to NK cell-mediated killing, we pretreated DOHH2 cells transfected with siNC, siCD70, or co-transfected with siCD70 and OE-ZZZ3 with mitomycin C to

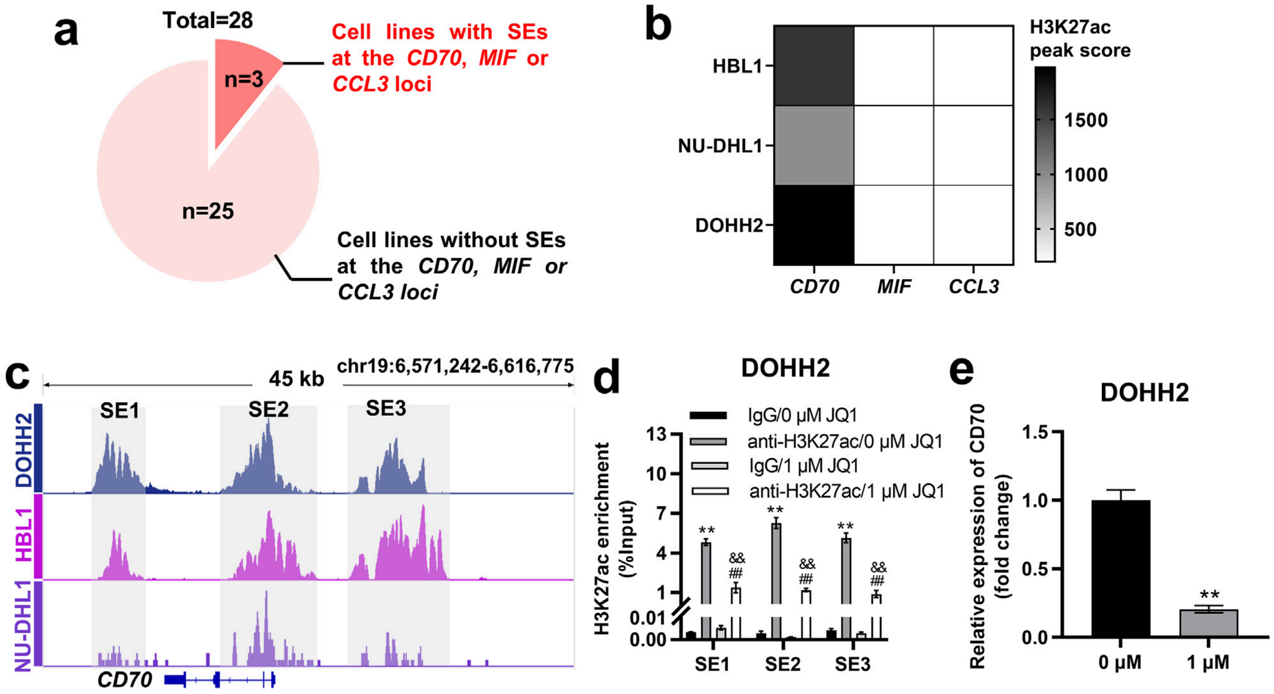

FIGURE 6
CD70 was identified as a SE-controlled gene in DOHH2, HBL1 and NU-DHL1 cells. **(A)** Screening of DLBCL cell lines with SE at the *CD70*, *MIF* or *CCL3* locus based on the GSE182214 dataset. **(B)** Heatmap of H3K27ac peak score for SE at the *CD70*, *MIF* or *CCL3* locus in HBL1, NU-DHL1, and DOHH2 cells based on the GSE182214 dataset. **(C)** Identification of three SE regions (SE1, SE2, and SE3) at the *CD70* locus in HBL1, NU-DHL1, and DOHH2 cells based on the GSE182214 dataset. **(D)** ChIP-qPCR was used to analysis the H3K27ac enrichment in three SE regions, and the effect of JQ1 treatment on H3K27ac enrichment in SE regions in DOHH2 cells. **P < 0.01, anti-H3K27ac/0 μM JQ1 group vs. IgG/0 μM JQ1 group. ##P < 0.01, anti-H3K27ac/1 μM JQ1 group vs. IgG/1 μM JQ1 group. &&P < 0.01, anti-H3K27ac/1 μM JQ1 group vs. anti-H3K27ac/0 μM JQ1 group. **(E)** qRT-PCR was used to detect the relative expression of CD70 in DOHH2 cells treated with 0 or 1 μM JQ1. **P < 0.01, 1 μM JQ1 group vs. 0 μM JQ1 group.

block cell proliferation. The mitomycin C pretreated DOHH2 cells were co-cultured with IL-2 activated NK92 cells at ratios of 1:1, 2:1 and 5:1. The proliferation of NK92 cells co-cultured with DOHH2 cells was detected by MTS assay. Co-culture of CD70-silenced DOHH2 cells with NK92 cells significantly promoted the proliferation of NK92 cells compared with NK92 cells co-cultured with DOHH2 cells transfected with siNC (Figure 8D). However, overexpression of ZZZ3 in DOHH2 cells significantly attenuated the promotion of NK92 cell proliferation by CD70 silence of DOHH2 cells in the co-culture system (Figure 8D).

Then, we evaluated the effect of ZZZ3/CD70 axis on LDH release from DOHH2 cells co-cultured with NK92 cells. DOHH2 cells (without mitomycin C pretreatment) were co-cultured with IL-2 activated NK92 cells at ratios of 1:1, 2:1 and 5:1. Silencing CD70 in DOHH2 cells significantly elevated LDH release from DOHH2 cells co-cultured with NK92 cells, which was offset by overexpression of ZZZ3 in DOHH2 cells (Figure 8E). Since interaction between PD1 and PD-L1 contributes to tumor immune evasion [11], we assessed the effect of silencing CD70 in DOHH2 cells combined with anti-PD-L1 treatment on LDH release from DOHH2 cells co-cultured with NK92 cells. DOHH2 cells (without mitomycin C pretreatment) and NK92 cells (IL-2 activated) were co-cultured at a ratio of 2:1. Anti-PD-L1 treatment or silencing CD70 in DOHH2 cells significantly promoted LDH release from DOHH2 cells co-cultured with NK92 cells (Figure 8F). Silencing CD70 in DOHH2 cells combined with anti-PD-L1 treatment significantly promoted LDH release from DOHH2 cells co-cultured with NK92 cells more strongly than anti-PD-L1 treatment alone (Figure 8F).

Taken together, the ZZZ3/CD70 axis in DLBCL cells promoted their escape from NK cell killing.

Discussion

Interactions between DLBCL cells and tumor-infiltrating immune cells are closely related to the development of DLBCL [16–18]. SEs are key regulators in promoting the malignant phenotype of tumor cells [25, 26], but the roles of SEs in modulating the interactions between tumor cells and infiltrating immune cells remain unknown. In the present study, we found that the enhanced interaction between B cell

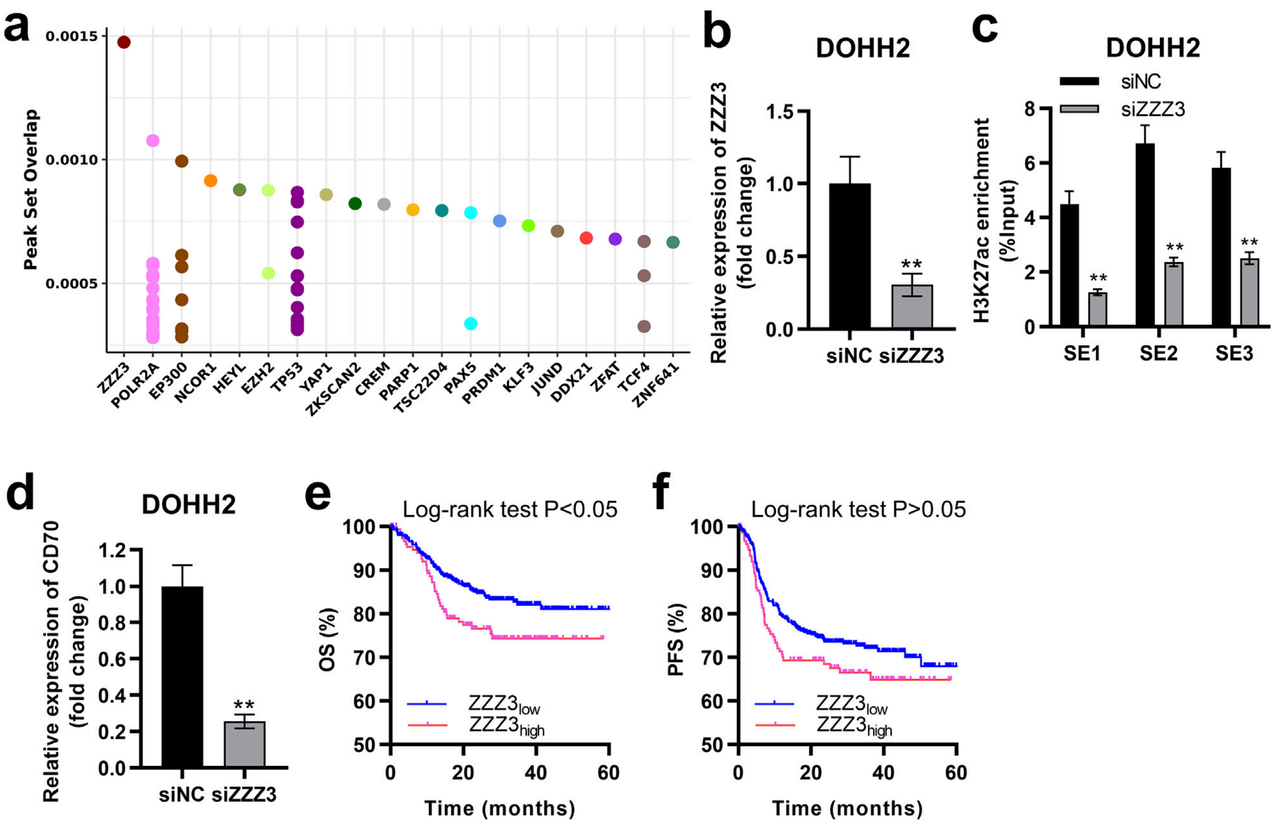

FIGURE 7

ZZZ3 interacted with the SE of *CD70* to drive CD70 expression. **(A)** Dot plots of the predicted transcription factors of *CD70*. **(B)** qRT-PCR was performed to measure the expression of ZZZ3 in DOHH2 cells transfected with siNC or siZZZ3. **P < 0.01, siZZZ3 group vs. siNC group. **(C)** ChIP-qPCR was used to detect the H3K27ac enrichment in three SE regions at the *CD70* locus in DOHH2 cells transfected with siNC or siZZZ3. **P < 0.01, siZZZ3 group vs. siNC group. **(D)** qRT-PCR was performed to measure the expression of CD70 in DOHH2 cells transfected with siNC or siZZZ3. **P < 0.01, siZZZ3 group vs. siNC group. **(E,F)** Kaplan–Meier overall survival (OS) and progression-free survival (PFS) curves of DLBCL patients with high- and low-ZZZ3 expression were plotted based on the GSE117556 dataset.

cluster and CD8$^+$ T cell and NK cell cluster in DLBCL compared to rLN. Specific interactions included the CD70-CD27, which contributes to the pathophysiology of autoimmunity [32]; the MIF-CD74/CXCR2 complex, regulating immune cell migration and inflammation [33]; the MIF-CD74/CD44 complex, mediating multiple biological processes, including cell proliferation and the inflammatory response [33, 34]; and the CCL3-CCR5, mediating immune cell recruitment [35]. Notably, a strong interaction between the B cell cluster and NK cell sub-cluster was identified. *CD70* was screened as a SE-controlled gene which was regulated by transcription factor ZZZ3 in DLBCL cells. These results highlighting the role of the CD70-CD27 interaction in DLBCL cell evasion from NK cell killing. Finally, effect of the ZZZ3/CD70 axis on the evasion of DLBCL cells from NK cell killing were examined *in vitro*.

DLBCL is a disease with complex pathogenesis, which is reflected not only in the genetic and epigenetic alterations of B lymphocytes, but also in the complicated crosstalk between tumor cells and tumor-infiltrating immune cells [36].In this study, we characterized the immune cell profile of DLBCL and identified five cell clusters (CD4$^+$ T cell cluster, CD8$^+$ T cell and NK cell cluster, B cell cluster, dendritic cell cluster, and macrophage cluster). CD4$^+$ T cells have cytotoxic or immunoregulatory functions [37, 38]. A low proportion of CD4$^+$ T cells in the TME is associated with a poor prognosis of primary central nervous system DLBCL [39]. CD8$^+$ T cells exert specific cytotoxic effects by secreting cytokines, releasing perforin and granzyme to kill tumor cells [40]. NK cells express cell surface receptors with stimulatory or inhibitory functions, or secrete cytokines and chemokines to exert cytolytic activity against target cells [41–43]. Dendritic cells exhibit strong antigen-presenting capacity, and stimulate T cells activation to trigger immune responses [44]. Macrophages are key regulators in mediating tumor immune evasion [45]. However, the interactions between DLBCL cells and tumor-infiltrating immune cells remain largely unknown.

Recent studies have successfully created single-cell transcriptome atlases for DLBCL. These atlases reveal

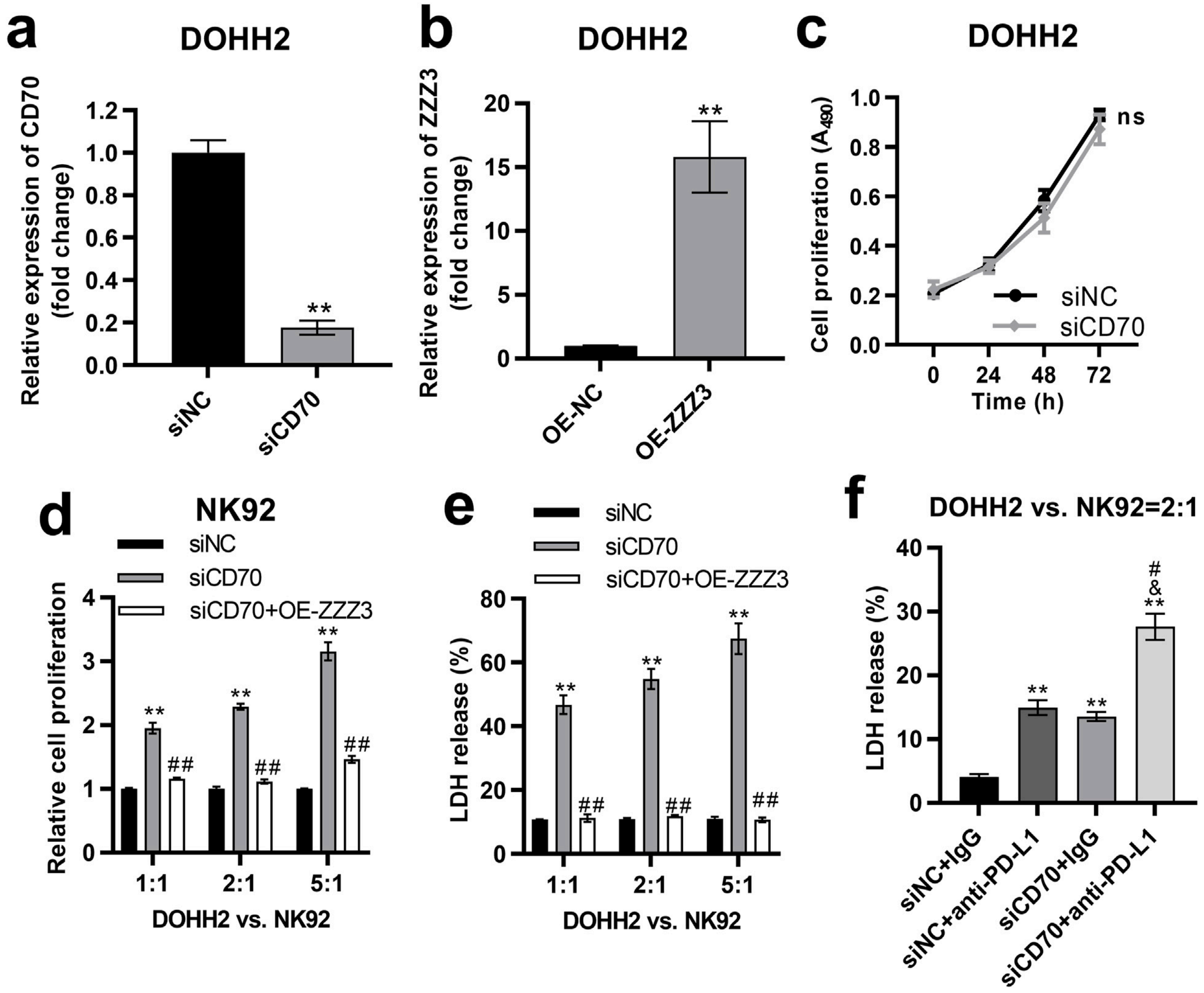

FIGURE 8
The ZZZ3/CD70 axis in DLBCL cells promoted their escape from NK cell killing. **(A)** qRT-PCR was performed to measure the expression of CD70 in DOHH2 cells transfected with siNC or siCD70. **$P < 0.01$, siCD70 group vs. siNC group. **(B)** qRT-PCR was used to measure ZZZ3 expression in DOHH2 cells transfected with OE-NC or OE-ZZZ3. **$P < 0.01$, OE-ZZZ3 group vs. OE-NC group. **(C)** MTS assay was used to determine the proliferation of DOHH2 cells transfected with siNC or siCD70. Ns. non-significantly. **(D)** MTS assay was used to detect the proliferation of NK92 cells co-cultured with mitomycin C pretreated DOHH2 cells. DOHH2 cells transfected with siNC, siCD70, or co-transfected siCD70 and OE-ZZZ3 (mitomycin C pretreated) and NK92 cells (IL-2 activated) were co-cultured at ratios of 1:1, 2:1 and 5:1 for 48 h **$P < 0.01$, siCD70 group vs siNC group. ##$P < 0.01$, siCD70 + OE-ZZZ3 group vs. siCD70 group. **(E)** LDH release from DOHH2 cells co-cultured with IL-2 activated NK92 cells. DOHH2 cells transfected with siNC, siCD70, or co-transfected with siCD70 and OE-ZZZ3 (without mitomycin C pretreatment) were co-cultured with IL-2 activated NK92 cells at ratios of 1:1, 2:1, 5:1. **$P < 0.01$, siCD70 group vs. siNC group. ##$P < 0.01$, siCD70 + OE-ZZZ3 group vs. siCD70 group. **(F)** LDH release from DOHH2 cells co-cultured with IL-2 activated NK92 cells and treated with anti-PD-L1 or IgG. DOHH2 cells transfected with siNC or siCD70 (without mitomycin C pretreatment) were co-cultured with IL-activated NK92 cells at a ratio of 2:1. **$P < 0.01$, vs. siNC + IgG group. &$P < 0.05$, vs. siNC+anti-PD-L1 group. #$P < 0.05$, vs. siCD70 + IgG group.

phenotypic diversity within DLBCL cases and interactions between tumor cells and the microenvironment. Steen et al. associate CXCR5+ CD8 T cells with the effectiveness of bortezomib when added to standard therapy [15]. Roider et al. propose that malignant B cells can receive both costimulatory and coinhibitory signals from all major T-cell subsets via CD80/CD86-CD28 and CD80/CD86-CTLA4 interactions [14]. In this study, we found that the enhanced interaction of B cell cluster to CD8$^+$ T cell and NK cell cluster was most pronounced in DLBCL compared with rLN. Furthermore, we found that NK cell sub-cluster interacted most strongly with B cell cluster. NK cells are innate lymphocytes, which are considered to be the first line of defense for host immune detection and play important roles in the progression of malignant tumors [46–48]. The number and activity of tumor-infiltrating NK cells have significant impacts on the prognosis of various cancers [48–50]. Patients with NK cell dysfunction have higher cancer incidence rates [51, 52]. Interactions between tumor cells and NK cells regulate the phenotype of NK cells, thereby affecting NK cells viability or function [51–55].

NK cells have received increasing attention for their potential in immunotherapy. However, studies on NK cells in DLBCL remain scarce. Frank Vari et al found that NK cell-mediated immune evasion is achieved by the interaction of PD1 and PD-L1 between NK cells and DLBCL cells [11]. However, the direct crosstalk and regulatory mechanisms of DLBCL cell-NK cell interaction remain largely enigmatic. Herein, we found that the interactions of CCL3-CCR5, CD70-CD27, MIF-CD74/CD44 complex, and MIF-CD74/CXCR2 complex between B cell cluster and CD8$^+$ T cells and NK cell cluster were significantly enhanced in DLBCL compared with rLN, which was mainly attributed to the strong interactions of B cell cluster with NK sub-cluster. It is well known that SEs interact with transcription factors to promote target genes transcription [21]. We wondered whether the expression of CCL3, CD70 and MIF is regulated by SEs in DLBCL cells. We found that DOHH2, HBL1 and NU-DHL1 cells had SEs only at the *CD70* locus but not at the *MIF* or *CCL3* locus. Furthermore, we demonstrated that *CD70* was a SE-controlled gene in DOHH2 cells and its expression was driven by the transcription factor ZZZ3.

CD70 is a member of the tumor necrosis factor (TNF) ligand family [56]. It has been reported that CD70 expression in non-Hodgkin lymphoma cells upregulates the proportion of Foxp3+CD4$^+$CD25- T cells and inhibits the proliferation of infiltrating CD8$^+$ T cells, thereby promoting an immunosuppressive microenvironment [57]. Co-inhibition of CD70 and PD-L1 rescued T cell depletion and effectively inhibited lymphoma growth *in vivo* [58]. However, the role of CD70 in regulating the interaction between DLBCL cells and NK cells remains unclear.

ZZZ3 (zinc finger ZZ-type containing 3), a core subunit of the ATAC complex, is required for ATAC complex-mediated maintenance of histone acetylation and gene activation [59]. However, we have not found any studies of ZZZ3 in regulating DLBCL progression. In this study, we found that high ZZZ3 expression predicts a poor OS of DLBCL patients. Importantly, we found that under co-culture of DOHH2 cells and NK92 cells, silencing CD70 in DOHH2 cells significantly promoted the proliferation of NK92 cells and LDH release from DOHH2 cells, which could be partially counteracted by ZZZ3 overexpression in DOHH2 cells. LDH is a ubiquitous intracellular enzyme that is released outside the cells when cells die [60]. LDH release is a key indicator of lytic cell death [60]. Thus, our results suggested that ZZZ3/CD70 axis in DLBCL cells promoted their escape from infiltrating NK cell cytotoxicity and inhibited the proliferation of infiltrating NK cells.

Moreover, mounting studies have provided that aberrant expression of PD-L1 of lymphoma cells is critical for mediating tumor immune evasion. Blocking the interaction between PD-L1 and PD1 could restore the anti-tumor immune response [11, 61, 62]. In this study, we found that both *CD70* and *CD274* (PD-L1 encoding gene) were expressed in Bcell_2 sub-cluster, and *PDCD1* (PD1 encoding gene) was expressed in NK cell sub-cluster, suggesting that targeting CD70 and PD-L1 simultaneously may effectively enhance the killing of DLBCL cells by NK cells. To verify this hypothesis, we demonstrated that silencing CD70 in DOHH2 cells combined with PD-L1 blockade significantly promoted killing of DLBCL cells by NK cells. These results suggested that CD70 plays a key role in the evasion of DLBCL cells from NK cell killing. Targeting CD70 in combination with anti-PD-L1 therapy could be a promising strategy for DLBCL treatment.

Conclusion

CD70 was an SE-controlled gene that was driven by ZZZ3 for transcription in DLBCL cells. The ZZZ3/CD70 axis in DLBCL cells inhibited infiltrating NK cell killing and proliferation, thereby promoting immune evasion of DLBCL cells. The ZZZ3/CD70 axis has the potential to be a novel immunotherapy target for DLBCL. Targeting ZZZ3/CD70 axis combined with PD-L1 blockade is expected to be a promising immunotherapeutic strategy for the treatment of DLBCL.

Author contributions

XL: conceived and designed the experiments; project administration; data analysis and interpretation; performed the experiments; wrote the manuscript; approved the final manuscript. JC and LW: data analysis and interpretation; performed the experiments; approved the final manuscript. CC: performed the experiments; approved the final manuscript. HL: data analysis and interpretation; approved the final manuscript. All authors contributed to the article and approved the submitted version.

Data availability statement

The raw data supporting the conclusions of this article will be made available by the authors, without undue reservation.

Funding

The author(s) declare that financial support was received for the research, authorship, and/or publication of this article. The work was supported by Natural Science Foundation of Shanxi Province of China (grant number 202103021224360).

Conflict of interest

The author(s) declared no potential conflicts of interest with respect to the research, authorship, and/or publication of this article.

Supplementary material

The Supplementary Material for this article can be found online at: https://www.ebm-journal.org/articles/10.3389/ebm.2024.10155/full#supplementary-material

References

1. Miao Y, Medeiros LJ, Li Y, Li J, Young KH. Genetic alterations and their clinical implications in DLBCL. *Nat Rev Clin Oncol* (2019) **16**(10):634–52. doi:10.1038/s41571-019-0225-1

2. Lacy SE, Barrans SL, Beer PA, Painter D, Smith AG, Roman E, et al. Targeted sequencing in DLBCL, molecular subtypes, and outcomes: a Haematological Malignancy Research Network report. *Blood* (2020) **135**(20):1759–71. doi:10.1182/blood.2019003535

3. Larouche JF, Berger F, Chassagne-Clément C, Ffrench M, Callet-Bauchu E, Sebban C, et al. Lymphoma recurrence 5 years or later following diffuse large B-cell lymphoma: clinical characteristics and outcome. *J Clin Oncol* (2010) **28**(12):2094–100. doi:10.1200/jco.2009.24.5860

4. Culjkovic-Kraljacic B, Fernando TM, Marullo R, Calvo-Vidal N, Verma A, Yang S, et al. Combinatorial targeting of nuclear export and translation of RNA inhibits aggressive B-cell lymphomas. *Blood* (2016) **127**(7):858–68. doi:10.1182/blood-2015-05-645069

5. Coupland SE. The challenge of the microenvironment in B-cell lymphomas. *Histopathology* (2011) **58**(1):69–80. doi:10.1111/j.1365-2559.2010.03706.x

6. Ansell SM, Vonderheide RH. Cellular composition of the tumor microenvironment. *Am Soc Clin Oncol Educ Book* (2013) **33**:e91–e97. doi:10.1200/edbook_am.2013.33.e91

7. Zhao Y, Xu H, Zhang M, Li L. Single-cell RNA-seq and bulk RNA-seq reveal intratumoral heterogeneity and tumor microenvironment characteristics in diffuse large B-cell lymphoma. *Front Genet* (2022) **13**:881345. doi:10.3389/fgene.2022.881345

8. Wherry EJ, Kurachi M. Molecular and cellular insights into T cell exhaustion. *Nat Rev Immunol* (2015) **15**(8):486–99. doi:10.1038/nri3862

9. Autio M, Leivonen SK, Brück O, Mustjoki S, Mészáros Jørgensen J, Karjalainen-Lindsberg ML, et al. Immune cell constitution in the tumor microenvironment predicts the outcome in diffuse large B-cell lymphoma. *Haematologica* (2021) **106**(3):718–29. doi:10.3324/haematol.2019.243626

10. Wang J, Sanmamed MF, Datar I, Su TT, Ji L, Sun J, et al. Fibrinogen-like protein 1 is a major immune inhibitory ligand of LAG-3. *Cell* (2019) **176**(1-2):334–47 e12. doi:10.1016/j.cell.2018.11.010

11. Vari F, Arpon D, Keane C, Hertzberg MS, Talaulikar D, Jain S, et al. Immune evasion via PD-1/PD-L1 on NK cells and monocyte/macrophages is more prominent in Hodgkin lymphoma than DLBCL. *Blood* (2018) **131**(16):1809–19. doi:10.1182/blood-2017-07-796342

12. Huang YH, Cai K, Xu PP, Wang L, Huang CX, Fang Y, et al. CREBBP/EP300 mutations promoted tumor progression in diffuse large B-cell lymphoma through altering tumor-associated macrophage polarization via FBXW7-NOTCH-CCL2/CSF1 axis. *Signal Transduction Targeted Ther* (2021) **6**(1):10. doi:10.1038/s41392-020-00437-8

13. Yuan CT, Chuang S, Cheng P, Chang K, Wang H, Tsai J, et al. Decreased CD11c-positive dendritic cells in the tumor microenvironment predict double-hit/triple-hit genotype and survival in diffuse large B-cell lymphoma. *The J Pathol Clin Res* (2022) **8**(5):436–47. doi:10.1002/cjp2.283

14. Roider T, Seufert J, Uvarovskii A, Frauhammer F, Bordas M, Abedpour N, et al. Dissecting intratumour heterogeneity of nodal B-cell lymphomas at the transcriptional, genetic and drug-response levels. *Nat Cell Biol* (2020) **22**(7):896–906. doi:10.1038/s41556-020-0532-x

15. Steen CB, Luca BA, Esfahani MS, Azizi A, Sworder BJ, Nabet BY, et al. The landscape of tumor cell states and ecosystems in diffuse large B cell lymphoma. *Cancer Cell* (2021) **39**(10):1422–37 e10. doi:10.1016/j.ccell.2021.08.011

16. Kawakubo K, Castillo CF, Liss AS. Epigenetic regulation of pancreatic adenocarcinoma in the era of cancer immunotherapy. *J Gastroenterol* (2022) **57**(11):819–26. doi:10.1007/s00535-022-01915-2

17. Garcia-Martinez L, Zhang Y, Nakata Y, Chan HL, Morey L. Epigenetic mechanisms in breast cancer therapy and resistance. *Nat Commun* (2021) **12**(1):1786. doi:10.1038/s41467-021-22024-3

18. Cheng B, Yu Q, Wang W. Intimate communications within the tumor microenvironment: stromal factors function as an orchestra. *J Biomed Sci* (2023) **30**(1):1. doi:10.1186/s12929-022-00894-z

19. Whyte WA, Orlando D, Hnisz D, Abraham B, Lin C, Kagey M, et al. Master transcription factors and mediator establish super-enhancers at key cell identity genes. *Cell* (2013) **153**(2):307–19. doi:10.1016/j.cell.2013.03.035

20. Jiang Y, Jiang YY, Lin DC. Super-enhancer-mediated core regulatory circuitry in human cancer. *Comput Struct Biotechnol J* (2021) **19**:2790–5. doi:10.1016/j.csbj.2021.05.006

21. Hnisz D, Abraham B, Lee T, Lau A, Saint-André V, Sigova A, et al. Super-enhancers in the control of cell identity and disease. *Cell* (2013) **155**(4):934–47. doi:10.1016/j.cell.2013.09.053

22. Jia Q, Chen S, Tan Y, Li Y, Tang F. Oncogenic super-enhancer formation in tumorigenesis and its molecular mechanisms. *Exp Mol Med* (2020) **52**(5):713–23. doi:10.1038/s12276-020-0428-7

23. Shin HY, Willi M, Yoo KH, Zeng X, Wang C, Metser G, et al. Hierarchy within the mammary STAT5-driven Wap super-enhancer. *Nat Genet* (2016) **48**(8):904–11. doi:10.1038/ng.3606

24. Hnisz D, Schuijers J, Lin C, Weintraub A, Abraham B, Lee T, et al. Convergence of developmental and oncogenic signaling pathways at transcriptional super-enhancers. *Mol Cell* (2015) **58**(2):362–70. doi:10.1016/j.molcel.2015.02.014

25. Bal E, Kumar R, Hadigol M, Holmes AB, Hilton LK, Loh JW, et al. Super-enhancer hypermutation alters oncogene expression in B cell lymphoma. *Nature* (2022) **607**(7920):808–15. doi:10.1038/s41586-022-04906-8

26. Xu H, Li Y, Jiang Y, Wang J, Sun H, Wu W, et al. A novel defined super-enhancer associated gene signature to predict prognosis in patients with diffuse large B-cell lymphoma. *Front Genet* (2022) **13**:827840. doi:10.3389/fgene.2022.827840

27. Becht E, McInnes L, Healy J, Dutertre CA, Kwok IWH, Ng LG, et al. Dimensionality reduction for visualizing single-cell data using UMAP. *Nat Biotechnol* (2018) **37**:38–44. doi:10.1038/nbt.4314

28. Hu C, Li T, Xu Y, Zhang X, Li F, Bai J, et al. CellMarker 2.0: an updated database of manually curated cell markers in human/mouse and web tools based on scRNA-seq data. *Nucleic Acids Res* (2023) **51**(D1):D870–D876. doi:10.1093/nar/gkac947

29. Sha C, Barrans S, Cucco F, Bentley MA, Care MA, Cummin T, et al. Molecular high-grade B-cell lymphoma: defining a poor-risk group that requires different approaches to therapy. *J Clin Oncol* (2019) **37**(3):202–12. doi:10.1200/jco.18.01314

30. Zheng R, Wan C, Mei S, Qin Q, Wu Q, Sun H, et al. Cistrome Data Browser: expanded datasets and new tools for gene regulatory analysis. *Nucleic Acids Res* (2019) **47**(D1):D729–D735. doi:10.1093/nar/gky1094

31. L'Yi S, Keller MS, Dandawate A, Taing L, Chen CH, Brown M, et al. Cistrome Explorer: an interactive visual analysis tool for large-scale epigenomic data. *Bioinformatics* (2023) **39**(2):btad018. doi:10.1093/bioinformatics/btad018

32. Han BK, Olsen NJ, Bottaro A. The CD27-CD70 pathway and pathogenesis of autoimmune disease. *Semin Arthritis Rheum* (2016) **45**(4):496–501. doi:10.1016/j.semarthrit.2015.08.001

33. Djudjaj S, Lue H, Rong S, Papasotiriou M, Klinkhammer BM, Zok S, et al. Macrophage migration inhibitory factor mediates proliferative GN via CD74. *J Am Soc Nephrol* (2016) **27**(6):1650–64. doi:10.1681/asn.2015020149

34. Yuan T, Zhang J, Zhao Y, Guo Y, Fan S. Single-cell RNA sequencing of intestinal crypts reveals vital events in damage repair and the double-edged sword effect of the Wnt3/β-catenin pathway in irradiated mice. *Redox Biol* (2023) **68**:102942. doi:10.1016/j.redox.2023.102942

35. Wu Y, Li YY, Matsushima K, Baba T, Mukaida N. CCL3-CCR5 axis regulates intratumoral accumulation of leukocytes and fibroblasts and promotes angiogenesis in murine lung metastasis process. *The J Immunol* (2008) **181**(9):6384–93. doi:10.4049/jimmunol.181.9.6384

36. Cioroianu AI, Stinga PI, Sticlaru L, Cioplea MD, Nichita L, Popp C, et al. Tumor microenvironment in diffuse large B-cell lymphoma: role and prognosis. *Anal Cell Pathol* (2019) **2019**:1–9. doi:10.1155/2019/8586354

37. Zhou Y, Zha J, Lin Z, Fang Z, Zeng H, Zhao J, et al. CD4+ T cell-mediated cytotoxicity is associated with MHC class II expression on malignant CD19+ B cells in diffuse large B cell lymphoma. *Exp Cell Res* (2018) **362**(2):287–92. doi:10.1016/j.yexcr.2017.11.029

38. Ding Z, Quast I, Yan F, Liao Y, Pitt C, O-Donnell K, et al. CD137L and CD4 T cells limit BCL6-expressing pre-germinal center B cell expansion and BCL6-driven B cell malignancy. *Immunol Cell Biol* (2022) **100**(9):705–17. doi:10.1111/imcb.12578

39. Parkhi M, Chatterjee D, Bal A, Vias P, Yadav BS, Prakash G, et al. Prognostic implications of the tumor immune microenvironment and immune checkpoint pathway in primary central nervous system diffuse large B-cell lymphoma in the North Indian population. *APMIS* (2022) **130**(2):82–94. doi:10.1111/apm.13195

40. Xu Y, Liu Z, Lv L, Li P, Xiu B, Qian W, et al. MiRNA-340-5p mediates the functional and infiltrative promotion of tumor-infiltrating CD8(+) T lymphocytes in human diffuse large B cell lymphoma. *J Exp Clin Cancer Res* (2020) **39**(1):238. doi:10.1186/s13046-020-01752-2

41. Abumaree MH, Bahattab E, Alsadoun A, Al Dosaimani A, Abomaray FM, Khatlani T, et al. Characterization of the interaction between human decidua parietalis mesenchymal stem/stromal cells and natural killer cells. *Stem Cell Res Ther* (2018) **9**(1):102. doi:10.1186/s13287-018-0844-y

42. Biron CA, Nguyen KB, Pien GC, Cousens LP, Salazar-Mather TP. Natural killer cells in antiviral defense: function and regulation by innate cytokines. *Annu Rev Immunol* (1999) **17**:189–220. doi:10.1146/annurev.immunol.17.1.189

43. Brandstadter JD, Yang Y. Natural killer cell responses to viral infection. *J Innate Immun* (2011) **3**(3):274–9. doi:10.1159/000324176

44. Gardner A, Ruffell B. Dendritic cells and cancer immunity. *Trends Immunol* (2016) **37**(12):855–65. doi:10.1016/j.it.2016.09.006

45. Genna A, Duran CL, Entenberg D, Condeelis JS, Cox D. Macrophages promote tumor cell extravasation across an endothelial barrier through thin membranous connections. *Cancers (Basel)* (2023) **15**(7):2092. doi:10.3390/cancers15072092

46. Muraro E, Comaro E, Talamini R, Turchet E, Miolo G, Scalone S, et al. Improved Natural Killer cell activity and retained anti-tumor CD8(+) T cell responses contribute to the induction of a pathological complete response in HER2-positive breast cancer patients undergoing neoadjuvant chemotherapy. *J Transl Med* (2015) **13**:204. doi:10.1186/s12967-015-0567-0

47. Cao Y, Wang X, Jin T, Tian Y, Dai C, Widarma C, et al. Immune checkpoint molecules in natural killer cells as potential targets for cancer immunotherapy. *Signal Transduction Targeted Ther* (2020) **5**(1):250. doi:10.1038/s41392-020-00348-8

48. Tumor-infiltrating NK cells exhibit tumor type-specific heterogeneity. *Cancer Discov*, 2023 **13**(11):OF1. doi:10.1158/2159-8290.CD-RW2023-143

49. Wang WT, Zhu HY, Wu YJ, Xia Y, Wu JZ, Wu W, et al. Elevated absolute NK cell counts in peripheral blood predict good prognosis in chronic lymphocytic leukemia. *J Cancer Res Clin Oncol* (2018) **144**(3):449–57. doi:10.1007/s00432-017-2568-2

50. Xu B, Chen L, Li J, Zheng X, Shi L, Wu C, et al. Prognostic value of tumor infiltrating NK cells and macrophages in stage II+III esophageal cancer patients. *Oncotarget* (2016) **7**(46):74904–16. doi:10.18632/oncotarget.12484

51. Russick J, Joubert PE, Gillard-Bocquet M, Torset C, Meylan M, Petitprez F, et al. Natural killer cells in the human lung tumor microenvironment display immune inhibitory functions. *J Immunother Cancer* (2020) **8**(2):e001054. doi:10.1136/jitc-2020-001054

52. Morvan MG, Lanier LL. NK cells and cancer: you can teach innate cells new tricks. *Nat Rev Cancer* (2016) **16**(1):7–19. doi:10.1038/nrc.2015.5

53. Carrega P, Morandi B, Costa R, Frumento G, Forte G, Altavilla G, et al. Natural killer cells infiltrating human nonsmall-cell lung cancer are enriched in CD56 bright CD16(-) cells and display an impaired capability to kill tumor cells. *Cancer* (2008) **112**(4):863–75. doi:10.1002/cncr.23239

54. Pasero C, Gravis G, Guerin M, Granjeaud S, Thomassin-Piana J, Rocchi P, et al. Inherent and tumor-driven immune tolerance in the prostate microenvironment impairs natural killer cell antitumor activity. *Cancer Res* (2016) **76**(8):2153–65. doi:10.1158/0008-5472.can-15-1965

55. Zhang QF, Yin WW, Xia Y, Yi YY, He QF, Wang X, et al. Liver-infiltrating CD11b(-)CD27(-) NK subsets account for NK-cell dysfunction in patients with hepatocellular carcinoma and are associated with tumor progression. *Cell Mol Immunol* (2017) **14**(10):819–29. doi:10.1038/cmi.2016.28

56. Flieswasser T, Camara-Clayette V, Danu A, Bosq J, Ribrag V, Zabrocki P, et al. Screening a broad range of solid and haematological tumour types for CD70 expression using a uniform IHC methodology as potential patient stratification method. *Cancers (Basel)* (2019) **11**(10):1611. doi:10.3390/cancers11101611

57. Yang ZZ, Novak AJ, Ziesmer SC, Witzig TE, Ansell SM. CD70+ non-Hodgkin lymphoma B cells induce Foxp3 expression and regulatory function in intratumoral CD4+CD25 T cells. *Blood* (2007) **110**(7):2537–44. doi:10.1182/blood-2007-03-082578

58. Nie M, Ren W, Ye X, Berglund M, Wang X, Fjordén K, et al. The dual role of CD70 in B-cell lymphomagenesis. *Clin Translational Med* (2022) **12**(12):e1118. doi:10.1002/ctm2.1118

59. Mi W, Zhang Y, Lyu J, Wang X, Tong Q, Peng D, et al. The ZZ-type zinc finger of ZZZ3 modulates the ATAC complex-mediated histone acetylation and gene activation. *Nat Commun* (2018) **9**(1):3759. doi:10.1038/s41467-018-06247-5

60. Jurisic V, Radenkovic S, Konjevic G. The actual role of LDH as tumor marker, biochemical and clinical aspects. *Adv Exp Med Biol* (2015) **867**:115–24. doi:10.1007/978-94-017-7215-0_8

61. Zhao L, Liu Y, Zhang J, Liu Y, Qi Q. LncRNA SNHG14/miR-5590-3p/ZEB1 positive feedback loop promoted diffuse large B cell lymphoma progression and immune evasion through regulating PD-1/PD-L1 checkpoint. *Cell Death Dis* (2019) **10**(10):731. doi:10.1038/s41419-019-1886-5

62. Zha H, Han X, Zhu Y, Yang F, Li Y, Li Q, et al. Blocking C5aR signaling promotes the anti-tumor efficacy of PD-1/PD-L1 blockade. *Oncoimmunology* (2017) **6**(10):e1349587. doi:10.1080/2162402x.2017.1349587

EBM Experimental Biology and Medicine

TYPE Original Research
PUBLISHED 20 November 2024
DOI 10.3389/ebm.2024.10193

*CORRESPONDENCE
Stephania A. Cormier,
stephaniacormier@lsu.edu
Luan D. Vu,
luan.vu@utsa.edu

†PRESENT ADDRESS
Luan D. Vu,
Department of Molecular Microbiology and Immunology, University of Texas at San Antonio, San Antonio, TX, United States

RECEIVED 08 April 2024
ACCEPTED 18 October 2024
PUBLISHED 20 November 2024

CITATION
Vu LD, Christofferson RC, O'Neal HR Jr., Hamer D, Phan ATQ, Vance KM, Turner EA, Kumar A, Yola IM, Lim N, Ogden B and Cormier SA (2024) Predicting severe COVID-19 using readily available admission indicators: SpO2/FiO2 ratio, comorbidity index, and gender.
Exp. Biol. Med. 249:10193.
doi: 10.3389/ebm.2024.10193

Predicting severe COVID-19 using readily available admission indicators: SpO2/FiO2 ratio, comorbidity index, and gender

Luan D. Vu[1]*†, Rebecca C. Christofferson[2], Hollis R. O'Neal Jr.[3], Diana Hamer[4], Anh T. Q. Phan[1], Katie M. Vance[4], E. A. Turner[2], Avinash Kumar[1], Ibrahim Musa Yola[4], Natalie Lim[1], Beverly Ogden[5] and Stephania A. Cormier[1]*

[1]Department of Biological Sciences, Louisiana State University and Pennington Biomedical Research Center, Baton Rouge, LA, United States, [2]Department of Pathobiological Sciences, School of Veterinary Medicine, Louisiana State University, Baton Rouge, LA, United States, [3]Medical Director of Research, Our Lady of the Lake Regional Medical Center, Pulmonary and Critical Care Medicine, Louisiana State University Health Sciences Center, Baton Rouge, LA, United States, [4]Office of Research Administration, Our Lady of the Lake Regional Medical Center, Baton Rouge, LA, United States, [5]Department of Research, Woman's Hospital, Baton Rouge, LA, United States

Abstract

The focus of this study was to identify risk factors for severe and critical COVID-19, evaluate local respiratory immune responses to SARS-CoV-2 infection, and develop a prognostic tool for COVID-19 severity using accessible early indicators. Using nasopharyngeal swab samples from hospitalized patients with COVID-19 of varying severity during the first wave of the pandemic from March to May 2020 in Louisiana, we evaluated the association between COVID-19 severity and viral load, respiratory immune mediators, and demographic/clinical factors. We found that the SpO_2/FiO_2 ratio at triage, total comorbidity burden (represented by Charlson Comorbidity Index), and gender were significantly associated with COVID-19 severity. Using these early significant indicators, we developed a prognostic tool for COVID-19 severity that is simple and convenient. Additionally, our study demonstrated that elevated levels of respiratory immune mediators, including IL-10, IL-6, MCP-1, and MCP-3, were significantly associated with COVID-19 severity. We also found that viral load at the time of admission was associated with disease severity. Our findings highlight the feasibility and importance of evaluating the humoral component of local mucosal immune responses and viral load at the infected site using convenient nasopharyngeal swab samples, which could be an effective method to understand the relationship between viral infection and immune responses at the early stages of infection. Our proposed prognostic tool has the potential to be useful for COVID-19 management in clinical settings, as it utilizes accessible and easy-to-collect variables at the time of admission.

KEYWORDS

COVID-19, SARS-CoV-2, prognostic, Charlson Comorbidity Index, severity

Impact statement

Early identification of COVID-19 severity indicators is vital for managing severe cases, allowing timely interventions to minimize complications and fatalities. Our study devised a practical prognostic tool for clinical settings, utilizing easily accessible admission variables like oxygen saturation, Charlson Comorbidity Index, and gender. Furthermore, we highlighted the feasibility of evaluating the humoral component of local mucosal immune responses and viral load using routine nasopharyngeal swab samples. This approach offers valuable insights into infection onset and informs targeted interventions, ultimately reducing COVID-19 related complications and mortality.

Introduction

The virus that causes the COVID-19 disease, SARS-CoV-2, has caused significant morbidity and mortality worldwide, with over 776 million cases and 7 million deaths attributed to the virus globally as of September 2024 [1]. The initial outbreak in Louisiana, which began in March 2020, caused a tremendous strain on the healthcare system [2, 3], leading to efforts to identify early indicators of COVID-19 severity to manage critical cases effectively. Rapid deterioration of respiratory function, dysregulated host response, and subsequent multiple organ failures are hallmarks of severe COVID-19 and are associated with a high mortality rate [4]. The treatment of severe COVID-19 continues to be challenging and arduous. Timely intervention based on early indicators of COVID-19 severity is essential to reduce mortality and COVID-19-related complications [5, 6].

During the first pandemic wave (from 24th February to 31st July, 2020), certain co-morbidities were indicated as primary risk factors for hospitalization and severe disease outcomes, including diabetes, obesity, COPD/smoking, and chronic kidney disease [7, 8], with additional demographic risk factors based on age and race [7, 9].

Since the emergence of the COVID-19 pandemic, understanding the relationship between viral load and disease severity has also been a critical research topic. Several studies have investigated this association, and the results have been mixed. It was suggested that viral load, often proxied by the qRT-PCR cycle threshold (CT or CQ value), is correlated with disease severity and/or presentation across several studies [10–19]. For example, one study found that higher viral load in patients was correlated with a loss of smell/taste, though there was no significant difference in the presentation of other symptoms [20]. Other studies demonstrated a higher load in severe vs. mild patients [14, 21, 22], or with the risk of death [23–27].

However, the association between viral load and disease severity or symptoms was not observed in other studies of COVID-19, as several studies reported no difference in viral load between asymptomatic patients and symptomatic patients [28–32], or between severity of disease, gender, race identity, or age groups [33–35]. One study found higher viral loads in non-hospitalized patients [36]. Thus, no clear or consistent association between viral load and disease state has emerged.

In addition to co-morbidities and viral loads, lymphopenia elevated inflammatory markers in peripheral blood have been consistently identified as biomarkers for COVID-19 severity. Studies have shown that greater levels of NLRP3 inflammasome activation in peripheral blood corresponded with more severe COVID-19 [37], that low expression of the IFNAR2 gene (an IFN 1 receptor subunit) was associated with critical illness in COVID-19 patients [38], that loss-of-function mutations in an another IFN I receptor subunit (IFNAR1) was associated with severe COVID-19 cases [39], and that auto-antibodies to IFN I were identified as a potential factor for severe COVID-19 [40]. It is evident that increased circulating IL-10, IL-6, IFN-gamma-inducible protein 10 (IP-10), and monocyte chemoattractant protein-1 and -3 (MCP-1 and MCP-3) are significantly associated with COVID-19 severity [41–47]. However, these circulating biomarkers are often observed during the late acute phase of the disease and usually result from the disease severity [44–47]. The evaluation of the immune responses in the peripheral blood compartment during the later phase of the disease may not accurately reflect the early responses of local mucosal immunity – the upper respiratory tract, which is essential for the first-line defense against SARS-CoV-2 and shaping adaptive immune responses. There is a need to better characterize the local innate immune responses to SARS-CoV-2 during the early stage of the disease. At the beginning of this first wave in March 2020, we pivoted our academic research lab into a CLIA-approved testing facility and partnered with local and state-wide facilities to provide enhanced testing capabilities [2]. During this time, we received nasopharyngeal swab samples from hospitalized patients with a full spectrum of COVID-19 severity (from mild, moderate to severe, and critical), spanning the first wave

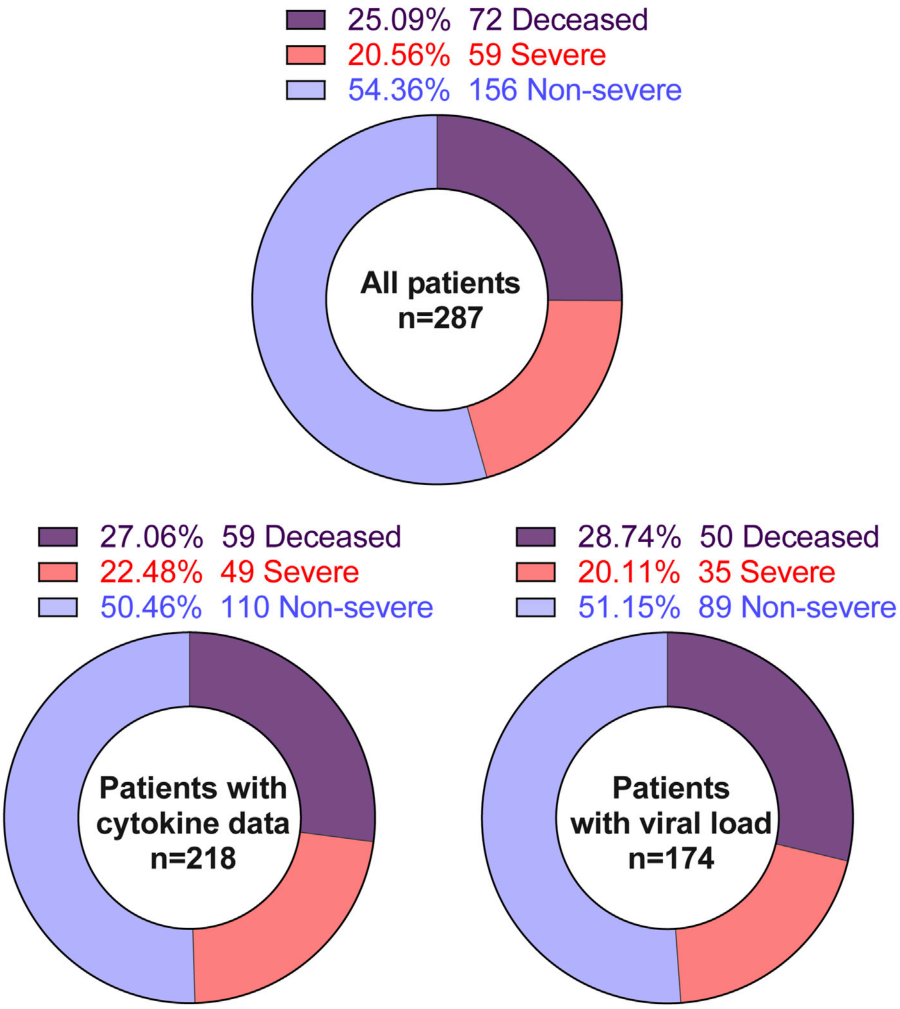

FIGURE 1
Summary of the studied population.

of the pandemic. Such cohorts allowed us to investigate the tripartite problem of how individual risk factors and co-morbidities, early local immune responses to SARS-CoV-2 infection, and relative viral load are associated with disease presentation and outcomes during the first wave of hospitalized patients as this represents the emergence phenomenon.

Materials and methods

Study approval

Our retrospective study was conducted at River Road Testing Lab [2], Louisiana State University (LSU), Pennington Biomedical Research Center, and Our Lady of the Lake Regional Medical Center. The study protocol was reviewed and approved by LSU Health Sciences Center [IRB#20-979 and exempt under 45CFR46.104 (d), category 4] on May 14, 2020. The protocol was conducted in accordance with relevant guidelines and institution policies. Because remnant nasopharyngeal swab samples received during routine care from SARS-CoV-2 infected patients were utilized in our study, informed consent was waived. All study sites worked under their approved biosafety protocols for handling SARS-CoV-2 specimens. Additionally, the authors vouch for the accuracy of the data reported.

Study participants

Because age is a significant predictor for COVID-19 severity, a random stratified sampling scheme was applied whereby patients were classified according to age using the following categories: 18–59, 60–79, 80+. However, the youngest patient was 22 years of age. The SARS-CoV-2 infection was laboratory-confirmed by quantitative reverse transcription PCR (qRT-PCR) using FDA-approved CDC SARS-CoV-2 panel two [45]. Patients were randomly selected from within each group for a target of 95–97 per group. This resulted in 287 unique individuals during the period of March – May 2020. While demographic and clinical information were successfully collected from all 287 patient samples, leftover nasopharyngeal swab samples were available from 218 patients. The leftover nasopharyngeal swab samples for these 218 patients were used to evaluate immune and metabolic mediators at the site of infection–the nasal mucosa. Viral loads were determined in the samples from 174 patients.

Multiplex cytokine, adipokines assays, and qRT-PCR for viral loads

Nasopharyngeal swab samples were not available from all patients in our cohorts. Our available data are detailed in Figure 1. Cell-free supernatants from nasopharyngeal swab samples were incubated at 56°C for 20 min to deactivate SARS-CoV-2 virions [48]. Then, heat-treated supernatants were subjected to electrochemiluminescence-based multiplex assays according to the manufacturer's protocol (MSD). The following analytes were measured: C-peptide, GLP-1, Glucagon, Insulin, IP-10, Leptin, PYY, G-CSF, GM-CSF, IFN-α2a, IFN-γ, IFN-β, IL-10, IL-12p70, IL-13, IL-15, IL-17A, IL-18, IL-1β, IL-1α, IL-22, IL-23, IL-29, IL-33, TSLP, IL-4, IL-5, IL-6, MCP-1, MCP-2, MCP-3, MCP-4, MDC, MIP-1α, MIP-1β, MIP-3α, MIP-3β, and MIP-5. Samples with analytes concentrations below the limit of detection (LOD) of the assay are replaced by a value equal to the LOD divided by the square root of 2 [49]. The data summaries are shown in Supplementary Table S1.

Quantitative reverse transcriptase PCR for viral loads

Viral RNA nasopharyngeal swab samples were extracted, transcribed, and amplified as previously described [50]. The results were interpolated from an internal standard curve, produced by identical processing of serial dilution of a known copies-number of SARS-CoV-2 RNA stock (EDX, #COV019), hereafter referred to as the viral load.

Data collection and coding

To investigate risk factors, anonymized clinical, paraclinical, and demographic data from patients admitted to Our Lady of the Lake (OLOL), were extracted into a REDCap database. To anonymize information from patients, the remnant nasopharyngeal swab samples from OLOL were relabeled with lab sample's ID before being sent to our lab. The lab's sample ID was used to communicate between OLOL and our lab.

Patient disposition was defined as "severe" if the patient was admitted to the intensive care unit (ICU) or "deceased" if the patient died due to COVID-19 during the hospitalization and within 30 days of discharge. All other patients were coded as "less severe." Obesity was determined by body mass index calculated from weight and height in the medical record, based on the CDC adult definition of "obese" [51]. Biological sex, age, and race were obtained from the medical record. Race was collected as African American (AA), Caucasian, Asian, and Other.

Patient cardiac, renal, pulmonary, hepatic, vascular, cancer, diabetes, and connective tissue comorbidities, as well as age at infection were also collected. To evaluate the combined impact of these comorbidities on COVID-19 severity, we used weighted Charlson Comorbidity Index (CCI) [52], a sum of weighted scores for each comorbidity.

Statistics

The data are described using standard descriptive statistics. The relationship of demographic, clinical, virological, and immunological variables with the outcome of disease severity (non-severe, severe, and deceased) was examined using ordered logistic regression. The effect of variables on the development of severe and deceased COVID-19 was represented as an unadjusted odds ratio (ORs) with 95% confidence interval (CI). Severity was tested for association with age, viral load, immune mediators, demographical variables, and obesity status with ordinal logistic regression while multinomial and bivariate logistic regression were employed to test for association between viral load and race and sex, respectively. Correlation matrixes for analytes was conducted using non-parametric Spearman correlation with two-tailed p-values and 95% confidence interval (95% CI).

We use an exploratory approach to ensure a final model for predicting COVID-19 severity. The initial multivariable ordered logistic regression model included only variables with $P \leq 0.05$ from the bivariate analyses. Because continuous variables were collected in different metrics, we used standard deviation units to standardize all variables [53]. Details regarding the selected variables are provided in Supplementary Table S1. A final ordered logistic regression model retained only variables with $P \leq 0.05$.

Then, we used the final ordered logistic regression model to calculate the coefficients of a formula to predict a logit transformation of the probability of severe and critical COVID-19, respectively. Thus, the logarithm of the odds is $\log\ [P(Y \leq j)/P(Y > j)] = \text{logit}\ [P(Y \leq j)] = \alpha_j - \sum \beta_i X_i$ [54]. With Y is an ordinal outcome with J the degree of disease severity ($j = 1$ for non-severe, $j = 2$ for severe, and $j = 3$ for deceased), $P(Y \leq j)$ is the cumulative probability of Y less than or equal to a

TABLE 1 Demographic and clinical characteristics of enrolled COVID-19 patients.

Characteristics	Deceased (n = 72)	Severe (n = 59)	Non_severe (n = 156)	P-value
Age (Median [IQR])	70.00 [58.75, 82.50]	64.00 [54.50, 74.00]	61.00 [48.00, 73.25]	0.002
LOS (Median [IQR])	8.00 [4.00, 12.25]	7.00 [4.00, 13.50]	3.00 [1.00, 5.00]	<0.001
ICU LOS (Median [IQR])	2.00 [0.00, 6.00]	3.00 [2.00, 7.50]	0.00 [0.00, 0.00]	<0.001
BMI (Median [IQR])	28.82 [25.91, 37.42]	32.22 [27.86, 39.70]	31.06 [25.03, 37.19]	0.346
Temperature at triage (Median [IQR])	99.25 [98.30, 100.38]	99.95 [99.03, 101.22]	99.00 [98.35, 100.30]	0.004
Heart rate at triage (Median [IQR])	99.00 [89.00, 110.00]	98.00 [86.00, 111.25]	93.00 [80.00, 106.00]	0.112
Respiration rate at triage (Median [IQR])	22.00 [18.00, 28.00]	20.00 [18.00, 23.25]	19.50 [18.00, 21.25]	0.004
SBP at triage (Median [IQR])	125.00 [106.00, 135.50]	122.50 [110.00, 140.25]	127.50 [115.00, 141.00]	0.15
DBP at triage (Median [IQR])	71.00 [63.00, 83.00]	72.00 [63.00, 83.50]	75.00 [66.00, 83.25]	0.381
SpO2 at triage (Median [IQR])	95.00 [91.00, 97.00]	96.00 [93.00, 98.00]	97.00 [94.00, 99.00]	0.003
Sex (%)				<0.001
Female	25 (34.7)	36 (61.0)	106 (67.9)	
Male	47 (65.3)	23 (39.0)	50 (32.1)	
Race (%)				0.386
African American	51 (70.8)	45 (76.3)	100 (64.1)	
Caucasian	17 (23.6)	13 (22.0)	49 (31.4)	
Others	4 (5.6)	1 (1.7)	7 (4.5)	
Ethnicity (%)				0.581
Hispanic	0 (0.0)1	(1.7)2	(1.3)	
Non_hispanic	72 (100)	58 (98.3)	154 (98.7)	
Obesity (%)* (missing 10 data points)				<0.001
Healthy	14 (19.7)	6 (10.2)	48 (32.7)	
Obesity	33 (46.5)	33 (55.9)	67 (45.6)	
Overweight	24 (33.8)	17 (28.8)	29 (19.7)	
Underweight	0 (0.0)	3 (5.1)	3 (2.0)	
Significant comorbidities present				
Chronic pulmonary disease (%)	9 (12.5)	4/55 (6.8/93.2)	2/154 (1.3/98.7)	0.049
Mild liver disease (%)	2/70 (2.8/97.2)	0/59 (0.0/100.0)	0/156 (0.0/100.0)	0.049
Peripheral vascular disease (%)	3/69 (4.2/95.8)	1/58 (1.7/98.3)	0/156 (0.0/100.0)	0.043
Acute kidney injury = Checked/Unchecked (%)	22/50 (30.6/69.4)	11/48 (18.6/81.4)	25/131 (16.0/84.0)	0.038
Congestive Heart Failure = No/Yes (%)	50/16 (75.8/24.2)	47/5 (90.4/9.6)	126/18 (87.5/12.5)	0.042
COPD = No/Yes (%)	55/11 (83.3/16.7)	47/5 (90.4/9.6)	137/7 (95.1/4.9)	0.019
Liver Disease (%)				0.008
Mild	2 (3.0)	1 (0.7)	3 (5.8)	
Moderate to Severe	3 (4.5)	0 (0.0)	0 (0.0)	
None	61 (92.4)	143 (99.3)	49 (94.2)	
Diabetes Mellitus (%)				0.003
End-organ damage	19 (28.8)	13 (25.0)	25 (17.4)	
None or diet-controlled	27 (40.9)	25 (48.1)	98 (68.1)	
Uncomplicated	20 (30.3)	14 (26.9)	21 (14.6)	

Definition of abbreviation: IQR, interquartile range; LOS, length of stay; ICU, intensive care unit; BMI, body mass index; SBP and DBP, systolic and diastolic blood pressure; SPO2, oxygen saturation; COPD, chronic obstructive pulmonary disease.

specific degree of disease severity. X is the value of the particular predictors included in the final model. There are i = 3 predictors in our parsimonious model (i = 1, 2, and 3). α_j is the intercept for specific (j) degree of disease severity; β_i is the vector of regression coefficient or the effect of the individual (i) predictors on the specific outcome Y – degree of disease severity.

Statistical significance was assessed at the $\boldsymbol{\alpha} = 0.05$ level. The associations were evaluated using odds ratios (OR) with 95%

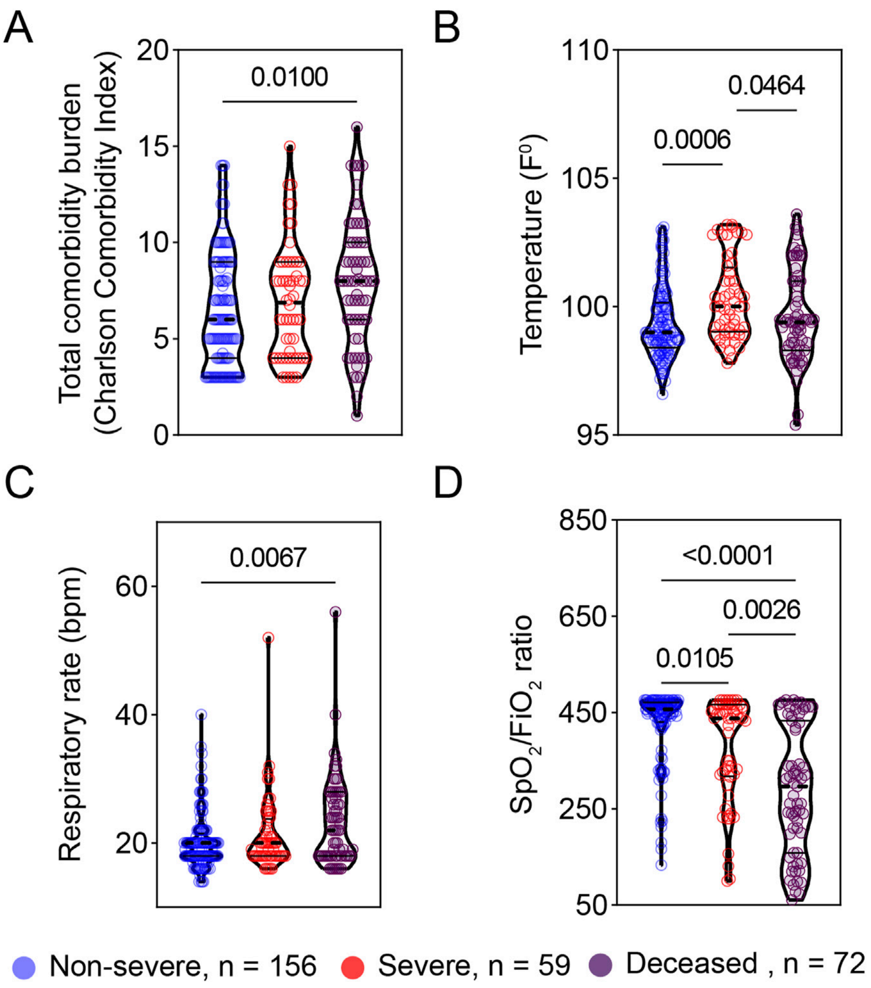

FIGURE 2
Vital signs at triage are associated with COVID-19 severity. The early vital signs at triage were compared between COVID-19 patients with non-severe (n = 156) and severe symptoms (n = 59) and deceased patients (n = 72) and are represented as violin plots. **(A)** Total comorbidity burden; **(B)** Temperature; **(C)** Respiratory rate; and **(D)** SpO_2/FiO_2 rate. The median is represented by the middle line. Significance was determined using Kruskal-Wallis non-parametric with post-hoc Dunn's multiple comparison test. P ≤ 0.05 is considered as significant. ns: non-significant.

confidence interval (95% CI) and *p ≤ 0.05, **p ≤ 0.01, ***p ≤ 0.01, and ****p ≤ 0.0001 as statistically significant. All statistics were performed in R (version 4.0.4) in R Studio (1.4.17) and SPSS (IBM).

Results

Characterization of the study cohort

We included 287 COVID-19 patient samples in our study. These patients were admitted to local hospitals in Baton Rouge from March 2020 to May 2020 with a range of COVID-19 severity, including 72 deceased, 59 severe, and 156 non-severe patients (Table 1). Patients with severe COVID-19 were hospitalized for significantly more days compared to patients with less severe COVID-19 (Table 1). While race and ethnicity are not significantly different between the three groups, age and gender were not uniformly distributed across the three groups (Table 1). Although body mass index (BMI) as a continuous variable is not associated with COVID-19 severity, the BMI-based obesity classification is significantly different among the three groups (Table 1). We also evaluated the relationship of more than 20 significant comorbidities with COVID-19 severity (Supplementary Table S1). Among these comorbidities, the preexisting conditions related to hepatic, renal, cardiac, and pulmonary diseases were significantly associated with COVID-19 severity (Table 1). To evaluate the total burden of these comorbidities on COVID-19 severity, we used the Charlson Comorbidity Index (CCI)

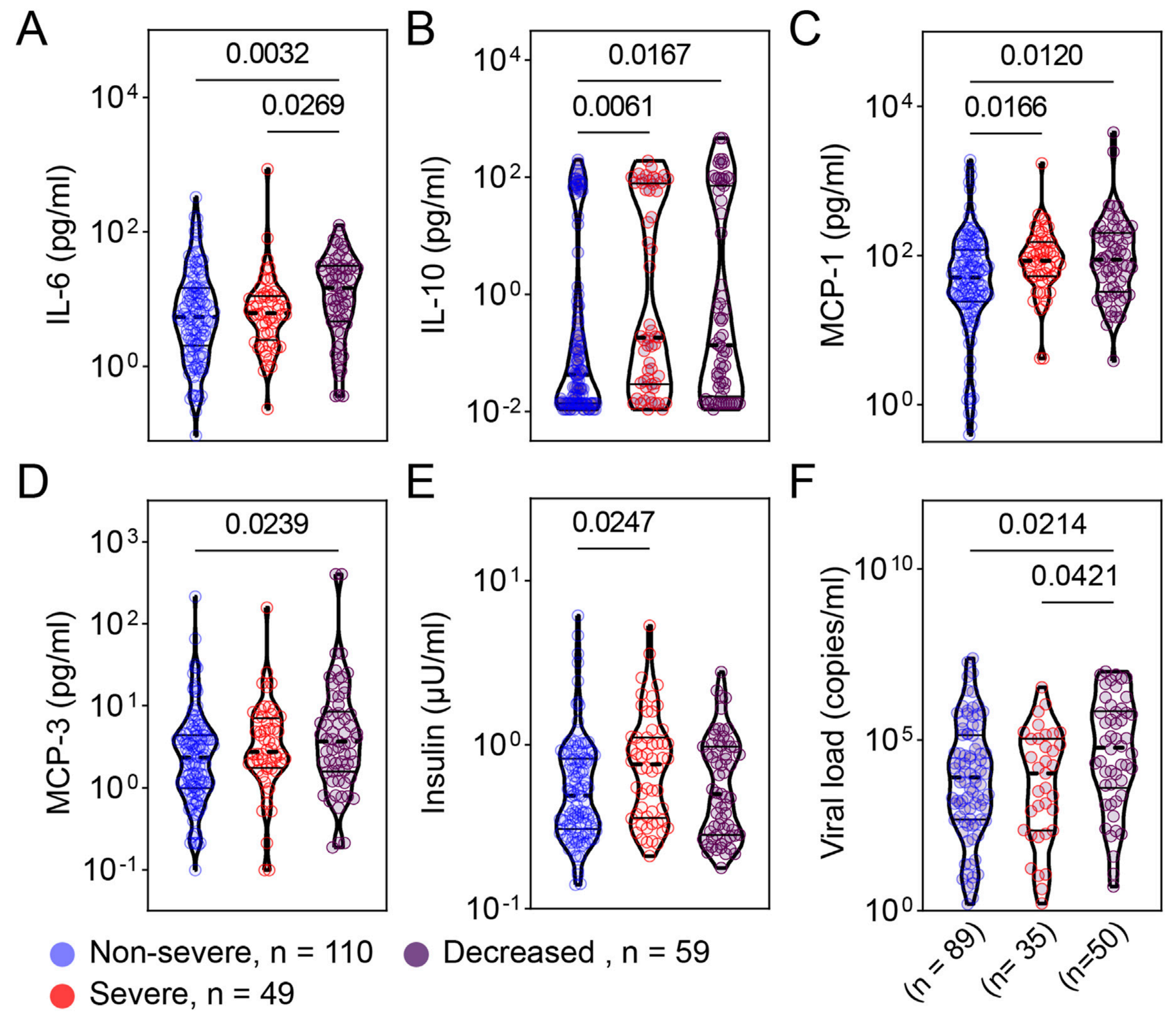

FIGURE 3
Patients with more severe COVID-19 exhibited greater levels of respiratory cytokines, adipokines, and viral load. Cytokines [IL-6 **(A)**, IL-10 **(B)**], chemokines [MCP-1 **(C)**, MCP-3 **(D)**], adipokines [insulin **(E)**], and viral load **(F)** from samples collected at admission were compared between patients with non-severe (n = 110), severe (n = 49), and deceased (n = 59) COVID-19. **(A)** Total comorbidity burden; **(B)** Temperature; **(C)** Respiratory rate; and **(D)** SpO_2/FiO_2 rate. Viral load data were available from 89, 35, and 50 patients from the non-severe, severe, and critical COVID-19 groups, respectively. The comparison are illustrated as violin plots. The median is represented by the middle dashed line. Significance was determined using Kruskal-Wallis non-parametric with post-hoc Dunn's multiple comparison test. P≤0.05 is considered as significant. ns: non-significant.

(53). Accordingly, the clinical severity significantly worsened as CCI increased (Figure 2B).

The early vital signs at triage are associated with COVID-19 severity

To explore early predictors of disease progression, we next examined the relationship of vital signs at triage with disease severity. At triage, patients with severe COVID-19 or deceased COVID-19 patients exhibited significantly higher body temperature and respiratory rate as compared to patients with non-severe COVID-19 (Figures 2B, C). Also, oxygen saturation to fraction of inspired oxygen ratios (SpO_2/FiO_2) at triage were significantly greater in non-severe COVID-19 patients compared to their severe or deceased peers (Figure 2D). There was no significant difference in either systolic (SBP) or diastolic blood pressure (DBP) among the three groups studied (Table 1).

Local mucosal inflammatory responses and respiratory viral load associated with COVID-19 severity

To evaluate the local mucosal inflammatory responses, we subjected remnant nasopharyngeal swab samples to

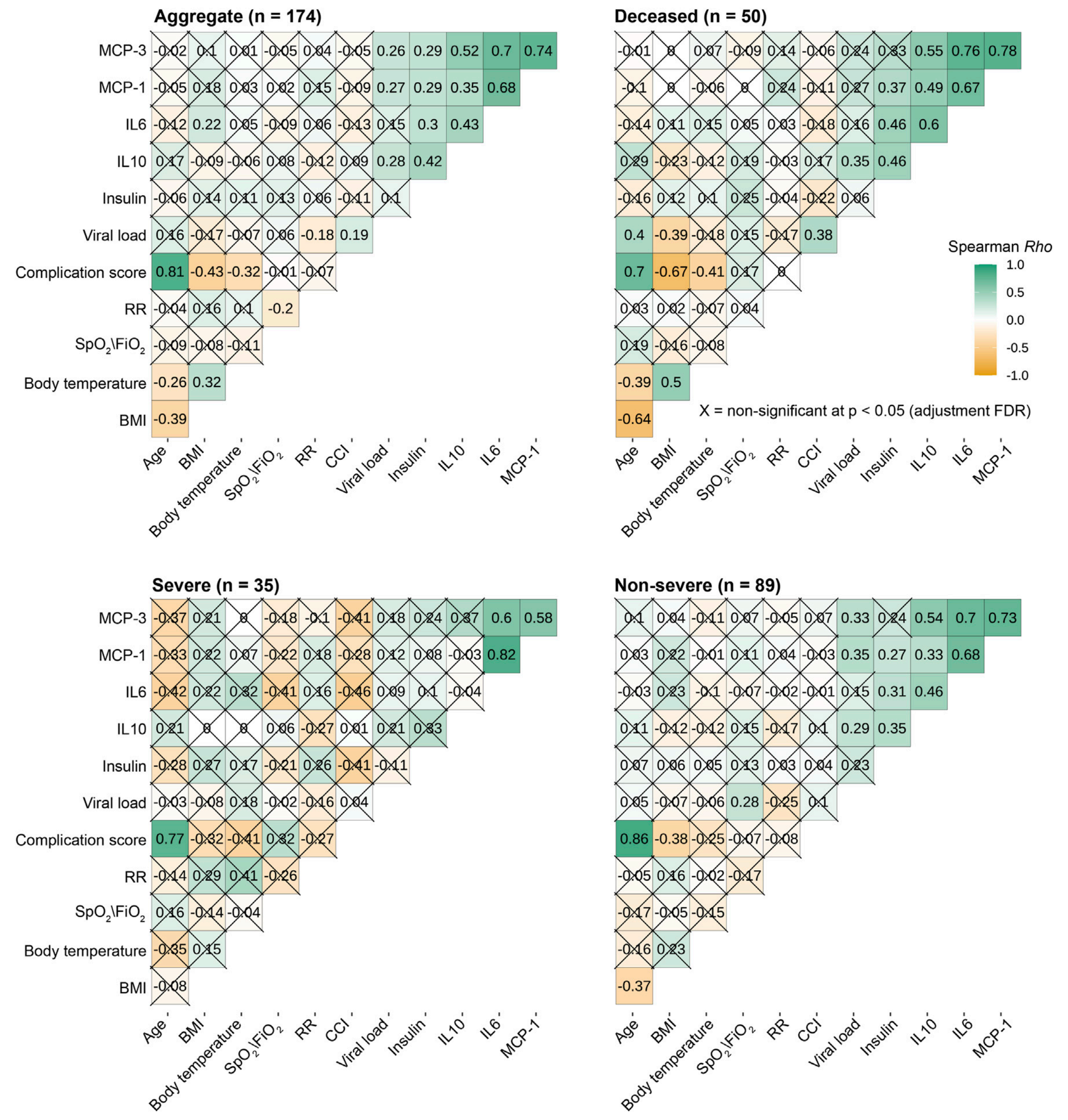

FIGURE 4
SARS-CoV-2 load significantly correlates with respiratory IL10, MCP-1 and MCP-3. The heat maps illustrate the Spearman rank correlation coefficient (Rho), varying from positive to negative correlation; green-white-dark yellow). The multiple comparison problems were controlled by adjusted False-discovery rate-adjusted P values with significant: P ≤ 0.05 (uncrossed squares) and non-significant P> 0.05 (crossed squares). BMI: body mass index; RR: respiratory rate; CCI: CCI: Total comorbidity burden – Charlson Comorbidity Index.

electrochemiluminescence -based multiplex assays examining 7 adipokines and 38 cytokines and chemokines. These analytes cover a wide range of inflammatory and metabolic pathways. We found increased levels of respiratory IL-6 and IL-10 in patients with more severe COVID-19 compared to less severe patients (Figures 3A, B). Similarly, patients with severe and critical COVID-19 exhibited significantly higher levels of monocyte chemoattractant protein −1 and −3 (MCP-1 and MCP-3) (Figures 3C, D). Although respiratory levels of insulin were significantly higher in severe compared to non-severe patients, there was no difference between severe and deceased patients regarding insulin levels (Figure 3E). We found that the distributions of viral load were significantly different between non-severe vs. deceased and severe vs. deceased (Figure 3F).

SARS-CoV-2 load significantly correlates with respiratory IL-10, MCP-1, and MCP-3

We next examined the relationship between viral load, local mucosal immune mediators, and early clinical indicators. To avoid the multiple comparisons problem, we only included variables significantly different between disease severity groups (Figure 4). We found that viral load was differentially correlated with immune response markers depending on whether data were aggregated over all patients or stratified based on disease severity (Figure 4). The pattern of correlation was not homogenous. In general, viral load was significantly and positively correlated with MCP-1, MCP-3, and IL-10. When we stratified for the degree of disease severity, several analytes were associated with viral load in one but not the other groupings. For example, IL-10 was positively and significantly correlated with viral load in deceased or non-severe patients but not in severe patients. Of note, there is no significant correlation between viral load and all other variables (Figure 4). Indeed, when we binned individuals into categories, ordered logistic regression revealed no association between increasing age group and viral load [OR: 0.86, 95% CI: (.73, 1.01)] (Supplementary Figure S1).

Next, we investigated whether viral load in this population was associated with being African American (“AA”) vs. not African American “(non-AA”). Logistic regression showed no association between viral load and identification as AA vs. not AA (Supplementary Figure S1). Similarly, we tested for an effect of biological sex (male vs. female) and found none (Supplementary Figure S1). On the other hand, viral load was significantly and positively correlated with age and CCI in deceased patients (Figure 4).

We observed a significant positive correlation among MCP-1, MCP-3, and IL-6 regardless of the degree of disease severity (Figure 4), suggesting common immune responses to SARS-CoV-2 infection. Although IL-10 and IL-6 were not correlated within the group of patients with severe COVID-19, they were directly proportional in deceased and non-severe groups.

Among early clinical and demographic indicators, we consistently observed a strong positive correlation between age at infection and CCI in all studied groups. In contrast, respiratory rate and SpO_2/FiO_2 ratio were not correlated with other variables regardless of disease severity. Intriguingly, in general, body temperature at triage was significantly correlated with BMI (Figure 4).

Male individuals with reduced SpO2/FiO2 ratio and increased CCI are at greater risk of developing severe and critical COVID-19

Having demonstrated the association between clinical and immunological factors with COVID-19 severity, we next sought to evaluate their potential predictability for disease severity. First, the relationship of individual factors with the severity of disease was assessed using ordered logistic regression (Figure 5A). To establish parsimonious models, we only tested the relationship of the severity of disease with factors that are not uniformly distributed among studied groups (non-severe, severe and deceased groups). We found that female (OR, 0.35; 95% CI, 0.19–0.64) individuals with high SpO_2/FiO_2 ratio at triage (OR, 0.37; 95% CI, 0.27–0.51) are at 2.86- and 2.7 fold lower risk of developing severe/critical COVID-19, respectively (Figure 5A). In contrast, higher CCI, age at infection, viral load, respiratory IL-10, and respiratory rate at triage were the drivers of worse clinical outcome. There was no significant association of other variables with COVID-19 severity by ordered logistic regression (Figure 5A). However, it is noteworthy that BMI-based obesity was significantly different among the three groups of patients (Non-severed vs. Severe vs. Deceased) with greater numbers of overweight and obese individuals classified as severe (33 obese, 17 overweight, 6 healthy weight) or deceased (33 obese, 24 overweight, 14 healthy weight) as compared to healthy weight and this is reflected in Table 1.

Among these 7 variables (gender, SpO_2/FiO_2 ratio at triage, CCI, respiratory IL-10, viral load, respiratory rate at triage, and age at infection), only CCI, SpO_2/FiO_2 ratio at triage, gender, and respiratory rate at triage were retained as potential risk factors in the final ordered logistic regression (Figure 5B). Because respiratory rate and SpO_2/FiO_2 ratio are clinically similar variables, only SpO_2/FiO_2 ratio, CCI, and gender were included in developing the parsimonious model. The combined influence of gender, SpO_2/FiO_2 ratio at triage, and CCI in the final ordered logistic regression model is illustrated in Figure 6. With the same levels of three risk factors, the probability of patients with non-severe COVID-19 developing severe disease (non-severe that escalates to severe) is higher than the probability of patients with severe COVID-19 progressing to more critical COVID-19 (severe that escalates to death). The effect of CCI and SpO_2/FiO_2 ratio at triage on the development of severe and deceased COVID-19 was greater in patients identifying as male. For example, a female patient with SPO_2/FiO_2 ratio of 224 at triage and CCI of 10 has a 14.9% probability of developing severe COVID-19 (if admitted without severe symptoms) and a 4.6% probability of progressing to critical/deceased COVID-19 (if admitted with severe symptoms). These probabilities will be significantly higher for male patients. For a male patient with the same SpO_2/FiO_2 ratio of 224 at triage and CCI of 10, the probabilities increase to 30.2% (non-severe progressing to severe) and 10.7% (severe progressing to critical/deceased). Therefore, males with reduced SpO_2/FiO_2 ratio and increased CCIs are at greater risk of developing severe and critical/deceased COVID-19.

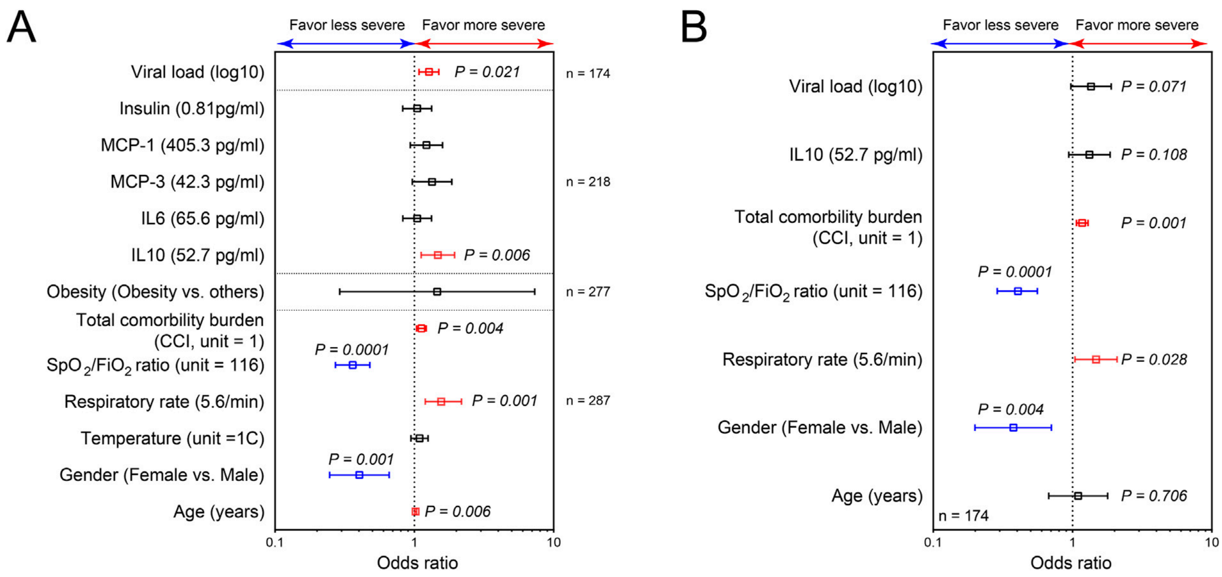

FIGURE 5

SARS-CoV-2 load, respiratory IL10, SPO_2/FiO_2 ratio, respiratory rate, gender and CCI at admission are significant risk factors for more severe COVID-19. Plots of risk factors for the development of more severe and critical COVID-19, using ordered logistic regression of individual factors **(A)**; and the combining effects for these potential risk factors **(B)**. The vertical line represents an odds ratio of 1. Odds ratios were represented as median with 95% confidence interval. $P \leq 0.05$ is considered as significant.

Discussion

Our current study demonstrated that SpO_2/FiO_2 ratio at triage, CCI, and gender are significant risk factors for developing severe and critical COVID-19 (Figure 5B). By leveraging these early indicators, the study established a practical prognostic tool for COVID-19 severity (Figure 6). As the variables included in our model are readily available and easily collected upon admission, this tool could prove valuable for COVID-19 management in the clinical setting and possibly other acute respiratory distress syndrome (ARDS) scenarios.

Using the residual nasopharyngeal swab samples, our study demonstrates the significant association between respiratory immune mediators (including IL-10, IL-6, MCP-1, and MCP-3) and COVID-19 severity (Figures 3A–D). In addition, our data reveal that viral load at the time of admission is associated with disease severity or mortality among hospitalized patients during the first wave of SARS-CoV-2 in Louisiana, USA (Figure 3F). This contributes to the growing evidence that viral load is a potential indicator of COVID-19 severity and a prognostic marker [10–19].

Numerous studies have proposed prediction models for COVID-19 severity [55–59]. In these previous studies, immune mediators in peripheral blood were used to predict the outcome of COVID-19. Although these immune mediators are strongly associated with COVID-19 severity and were shown as independent indicators for the progression of COVID-19, they were detected during the late acute phase of the disease (day 5–20 post-symptoms onset) and more likely resulted from developing severe disease [55–59]. Moreover, these immune mediators are not always easily accessible in clinical settings or available in a timely manner. These limitations hinder the predictability of immune-related variables in forecasting COVID-19 severity. In contrast, our study employs early and common clinical indicators, including SpO_2/FiO_2 ratio at triage, CCI, and gender, to create straightforward and convenient prognostic model for COVID-19 severity (Figure 6).

Considering the complexity and dynamic nature of COVID-19 progression, which rapidly changes throughout the disease course, we designed our model to calculate the probability of non-severe patients developing severe COVID-19 and the probability of severe patients developing more critical/deceased symptoms separately. As a result, our model offers a supplementary tool for assessing the risk of developing severe and critical/deceased COVID-19 in clinical settings at the time of admission without the need for additional paraclinical parameters. Additionally, we provide a method for designing parsimonious prognostic models for other viral respiratory infection diseases (Figure 5). However, due to the moderate sample size (n = 174), it is necessary to validate the predictive capacity of our proposed model in larger, independent cohorts.

Our current study also examined immunological mediators and viral load from remnant nasopharyngeal swab samples. It is evident that the exacerbated pro-inflammatory responses to

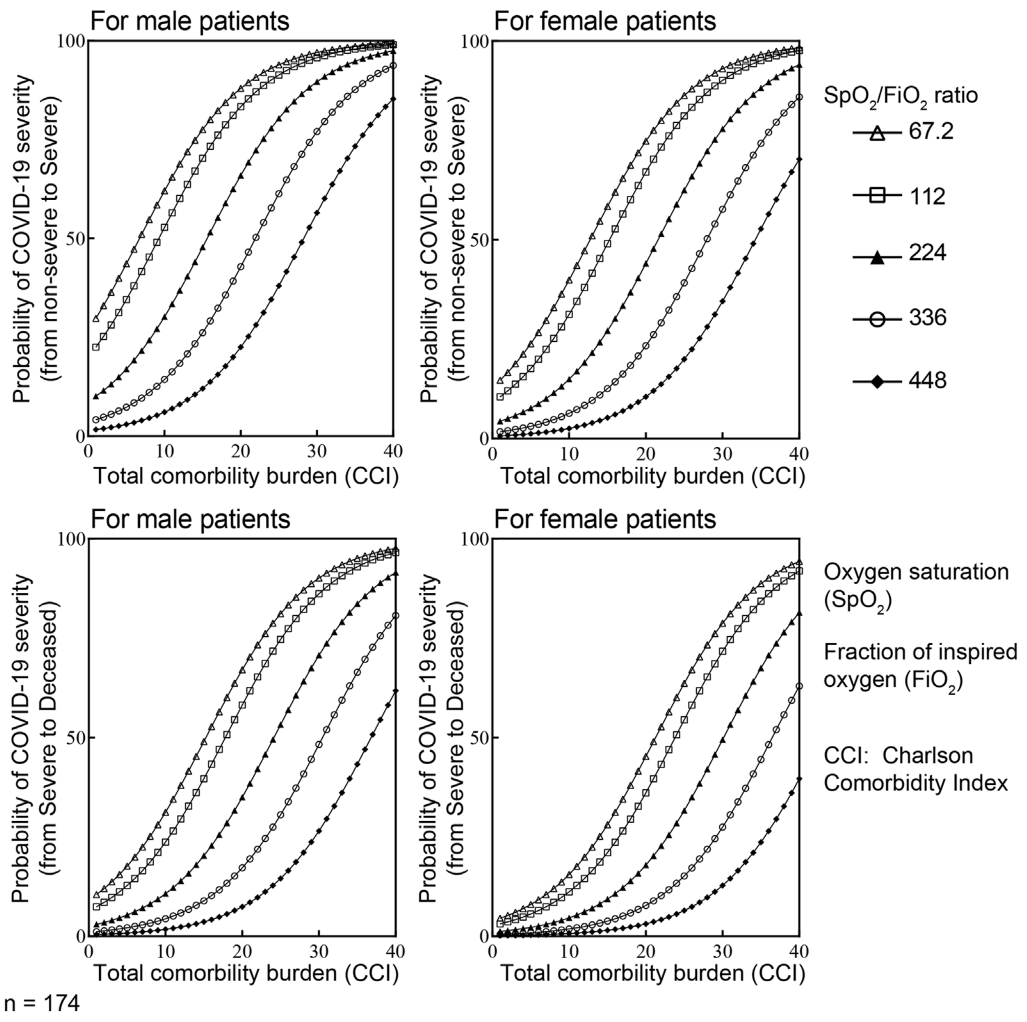

FIGURE 6
The combined influence of CCI, SpO_2/FiO_2 ratio at triage and gender on the development of more severe COVID-19 using ordered logistic regression. Considering Y is an ordinal outcome with J the degree of disease severity (j = 1 for non-severe, j = 2 for severe and j = 3 for deceased), P $(Y \leq j)$ is the cumulative probability of Y less than or equal to specific degree of disease severity. Therefore, the odds of being less than or equal to specific degree of disease severity is $P(Y \leq j)/P(Y > j)$. Accordingly, the logarithm of the odds is $\log [P(Y \leq j)/P(Y > j)] = \text{logit } [P(Y \leq j)]$. With X is value of the particular predictors included in the final model. There are i = 3 predictors in our parsimonious model (i = 1, 2,3). α_j is the intercepts for specific (j) degree of disease severity; β_i is the vector of regression coefficient or the effect of individual (i) predictors on the specific outcome Y−degree of disease severity. In this context, $\text{logit } [P(Y \leq j)] = \alpha_j - \sum \beta_i X_i$. In the final ordered logistic regression model: α (non-severe vs. severe) = 1.34; α (severe vs. deceased) = 2.62; $\beta_{(male)} = 0.901$; $\beta_{(CCI)} = 0.15$; $\beta_{(SPO2/FiO2)} = -0.95$.

SARS-CoV-2 are significantly associated with more severe COVID-19 immunopathology [41–47]. While studies have provided insights from immune mediator levels in peripheral blood following SARS-CoV-2 infection, the immune responses in the peripheral blood compartment may not accurately reflect the local immune responses at a more relevant infected site. Herein, we demonstrated the significant association between elevated levels of respiratory immune mediators (including IL-10, IL-6, MCP-1, and MCP-3) and COVID-19 severity. MCP-1 and MCP-3, produced mainly by cells such as airway epithelial cells, endothelial cells, and myeloid cells, were found to be monocyte chemotactic proteins for myeloid and lymphoid cells [60]. The increased MCP-1 and MCP-3 in more severe COVID-19 reinforce the pathogenic role of the exacerbated pro-inflammatory responses in COVID-19.

Using remnant nasopharyngeal swab samples, which are more accessible and less invasive than peripheral blood collection, we not only reinforce the previous findings on the association of increased circulating immune mediators and more severe COVID-19 [41–47, 61, 62] but more importantly demonstrate the feasibility of evaluating the humoral component of local mucosal immune responses and viral load at the infection site. This method allows us to evaluate the viral load and mucosal immune responses at the site of SARS-CoV-2 infection at the same time point, helping understand the relationship between viral infection and mucosal immune responses at the early of infection. Increased MCP-1 has been shown to be significantly and negatively correlated with the inhibition of interferon regulatory factor 3 (IRF3) pathway in patients with severe COVID-19 [63]. It is evident that the SARS-CoV-2 spike and Nsp12/6 proteins attenuate the host's innate immune responses by suppressing IRF3-induced type 1 IFN production [64–66], suggesting the mechanism of immune evasion to facilitate the viral replication and COVID-19 severity. Together these data suggest that increased MCP-1 levels are significantly and negatively correlated with attenuated type 1 IFN production and, therefore, positively correlated with elevated viral load. Indeed, we found that increased viral load is associated with more severe COVID-19 and significantly, positively correlated with IL-10, MCP-1, and MCP-3 (Figures 3F, 4). Our data confirm the previous studies on the positive association of excessive cytokines and increased viral load with COVID-19 severity.

However, unlike data on peripheral cytokine responses, findings on viral load in association with COVID-19 severity are highly inconsistent among studies [18, 22] due to several factors. First, the disparities in the timing of sample collection contribute to inconsistency, as viral replication kinetics rapidly change over the course of the disease due to host immune responses. Controlling for varying degrees of different stages of the disease is essential for interpreting viral load data. However, these confounding effects were often not examined in numerous studies [10–27]. When available, the peak of viral load in longitudinal samples can be used to standardize the findings across studies. Second, viral load data were determined in different specimens, including respiratory [21] and plasma samples [67]. It has been shown that viremia is associated with severe and critical COVID-19 and is often under the limit of detection in asymptomatic and less severe patients [68]. The viremia in severe and critical COVID-19 patients is not comparable with viral load in respiratory samples, which is available in patients with a full spectrum of the disease severity (from asymptomatic to critical).

Our current study has certain limitations. During the first wave of COVID-19 (from March to May 2020), there was an extremely urgent need to identify the SARS-CoV-2 infected patients among patients with respiratory-related illnesses using nasopharyngeal swabs. Early in the pandemic, most COVID-19 patients at our institution were in isolation, making it difficult to collect longitudinal specimens and all relevant patient information, such as the day of symptom onset. We are aware that the single-time point respiratory sample collection in our study only represents a snapshot of changes in local immune responses. Because viral replication and immune responses to viral infection change throughout the disease, it is clear that the temporal profiles of infection need to be considered to get a clear picture of the relationship between viral load and immune responses. Nevertheless, our data demonstrate that even using remnant nasopharyngeal swab samples collected at admission and stored frozen for several months, we are able to observe early local mucosal responses to SARS-CoV-2 at the infected site. Once again, our study emphasizes the importance of considering the relationship between viral load and immune responses as investigating the mechanism of COVID-19 pathology. It also shows the value of early detection of risk factors and potential prognostic markers for clinical management. Nonetheless, the study also notes the need for validation in larger cohorts.

Author contributions

LV, DH, KV, ET, AP, AK, NL, RC, HO'N, IY, BO, and SC, collected data, performed experiments, analyzed data, provided intellectual input, and contributed to manuscript preparation; LV and SC conceptualized the study; LV, RC, and SC drafted the manuscript. SC and HO'N directed the study. All authors contributed to the article and approved the submitted version.

Data availability

The original contributions presented in the study are included in the article/Supplementary Material, further inquiries can be directed to the corresponding authors.

Ethics statement

The studies involving humans were approved by the study protocol was reviewed and approved by LSU Health Sciences Center (IRB#20-979 and exempt under 45CFR46.104 (d), category 4) on 14 May 2020. The studies were conducted in accordance with the local legislation and institutional requirements. The human samples used in this study were acquired from remnant nasopharyngeal swab samples collected during routine care from SARS-CoV-2 infected patients. Written informed consent for participation was not required from the participants or the participants' legal guardians/next of kin in accordance with the national legislation and institutional requirements.

Funding

The author(s) declare that financial support was received for the research, authorship, and/or publication of this article.

The study was partially funded by Merck Sharp and Dohme Corp (MISP Project #60320). The content is solely the responsibility of the authors and does not necessarily reflect the official views of Merck.

Acknowledgments

We would like to thank Our Lady of the Lake Regional Medical Center staff for their tremendous support.

Conflict of interest

The author(s) declared no potential conflicts of interest with respect to the research, authorship, and/or publication of this article.

Supplementary material

The Supplementary Material for this article can be found online at: https://www.ebm-journal.org/articles/10.3389/ebm.2024.10193/full#supplementary-material

References

1. World Health Organization. *WHO COVID-19 dashboard* (2024). Available from: https://data.who.int/dashboards/covid19/cases?n=o (Accessed September 15, 2024).

2. Christofferson RC, O'Neal HR, Jagneaux T, O'Neal C, Walsh CS, Mayton EH, et al. Reduced turnaround times through multi-sectoral community collaboration during the first surge of SARS-CoV-2 and associated effect on patient care and hospital operations. *PLoS One* (2021) **16**(10):e0257302. doi:10.1371/journal.pone.0257302

3. Daigle A. *Coronavirus cases grew faster in Louisiana than anywhere else in the world: UL study*. Advocate (2020). Available from: https://www.theadvocate.com/acadiana/news/coronavirus/coronavirus-cases-grew-faster-in-louisiana-than-anywhere-else-in-the-world-ul-study/article_94494420-6d4b-11ea-ac42-ff7dd722c084.html (Accessed February 10, 2024).

4. Nakayama R, Bunya N, Tagami T, Hayakawa M, Yamakawa K, Endo A, et al. Associated organs and system with COVID-19 death with information of organ support: a multicenter observational study. *BMC Infect Dis* (2023) **23**:814. doi:10.1186/s12879-023-08817-5

5. Gupta S, Wang W, Hayek SS, Chan L, Mathews KS, Melamed ML, et al. Association between early treatment with tocilizumab and mortality among critically ill patients with COVID-19. *JAMA Intern Med* (2021) **181**(1):41–51. doi:10.1001/jamainternmed.2020.6252

6. Zhou H, Huang H, Xie X, Gao J, Wu J, Zhu Y, et al. Development of early warning and rapid response system for patients with novel coronavirus pneumonia (COVID-19): a research protocol. *Medicine (Baltimore)* (2020) **99**(34):e21874. doi:10.1097/MD.0000000000021874

7. Ko JY, Danielson ML, Town M, Derado G, Greenlund KJ, Kirley PD, et al. Risk factors for coronavirus disease 2019 (COVID-19)–Associated hospitalization: COVID-19–Associated hospitalization surveillance network and behavioral risk factor surveillance system. *Clin Infect Dis* (2021) **72**(11):e695–e703. doi:10.1093/cid/ciaa1419

8. Cai G, Bossé Y, Xiao F, Kheradmand F, Amos CI. Tobacco smoking increases the lung gene expression of ACE2, the receptor of SARS-CoV-2. *Am J Respir Crit Care Med* (2020) **201**(12):1557–9. doi:10.1164/rccm.202003-0693LE

9. Gao YD, Ding M, Dong X, Zhang JJ, Kursat Azkur A, Azkur D, et al. Risk factors for severe and critically ill COVID-19 patients: a review. *Allergy* (2021) **76**(2):428–55. doi:10.1111/all.14657

10. Liu Y, Yan L-M, Wan L, Xiang T-X, Le A, Liu J-M, et al. Viral dynamics in mild and severe cases of COVID-19. *The Lancet Infect Dis* (2020) **20**(6):656–7. doi:10.1016/s1473-3099(20)30232-2

11. Rao SN, Manissero D, Steele VR, Pareja J. A systematic review of the clinical utility of cycle threshold values in the context of COVID-19. *Infect Dis Ther* (2020) **9**(3):573–86. doi:10.1007/s40121-020-00324-3

12. Lescure F-X, Bouadma L, Nguyen D, Parisey M, Wicky P-H, Behillil S, et al. Clinical and virological data of the first cases of COVID-19 in Europe: a case series. *The Lancet Infect Dis* (2020) **20**(6):697–706. doi:10.1016/s1473-3099(20)30200-0

13. Tan L, Kang X, Ji X, Li G, Wang Q, Li Y, et al. Validation of predictors of disease severity and outcomes in COVID-19 patients: a descriptive and retrospective study. *Med* (2020) **1**(1):128–38.e3. doi:10.1016/j.medj.2020.05.002

14. Zheng S, Fan J, Yu F, Feng B, Lou B, Zou Q, et al. Viral load dynamics and disease severity in patients infected with SARS-CoV-2 in Zhejiang province, China, January-March 2020: retrospective cohort study. *BMJ* (2020) **369**:m1443. doi:10.1136/bmj.m1443

15. To KK-W, Tsang OT-Y, Leung W-S, Tam AR, Wu T-C, Lung DC, et al. Temporal profiles of viral load in posterior oropharyngeal saliva samples and serum antibody responses during infection by SARS-CoV-2: an observational cohort study. *The Lancet Infect Dis* (2020) **20**(5):565–74. doi:10.1016/s1473-3099(20)30196-1

16. Shi F, Wu T, Zhu X, Ge Y, Zeng X, Chi Y, et al. Association of viral load with serum biomakers among COVID-19 cases. *Virology* (2020) **546**:122–6. doi:10.1016/j.virol.2020.04.011

17. Kam KQ, Thoon KC, Maiwald M, Chong CY, Soong HY, Loo LH, et al. SARS-CoV-2 viral RNA load dynamics in the nasopharynx of infected children. *Epidemiol Infect* (2021) **149**:e18–13. doi:10.1017/s095026882100008x

18. Yu F, Yan L, Wang N, Yang S, Wang L, Tang Y, et al. Quantitative detection and viral load analysis of SARS-CoV-2 in infected patients. *Clin Infect Dis* (2020) **71**(15):793–8. doi:10.1093/cid/ciaa345

19. Pan Y, Zhang D, Yang P, Poon LLM, Wang Q. Viral load of SARS-CoV-2 in clinical samples. *The Lancet Infect Dis* (2020) **20**(4):411–2. doi:10.1016/s1473-3099(20)30113-4

20. Julin CH, Robertson AH, Hungnes O, Tunheim G, Bekkevold T, Laake I, et al. Household transmission of SARS-CoV-2: a prospective longitudinal study showing higher viral load and increased transmissibility of the alpha variant compared to previous strains. *Microorganisms* (2021) **9**(11):2371. doi:10.3390/microorganisms9112371

21. Yu X, Sun S, Shi Y, Wang H, Zhao R, Sheng J. SARS-CoV-2 viral load in sputum correlates with risk of COVID-19 progression. *Crit Care* (2020) **24**(1):170. doi:10.1186/s13054-020-02893-8

22. Kociolek LK, Muller WJ, Yee R, Dien Bard J, Brown CA, Revell PA, et al. Comparison of upper respiratory viral load distributions in asymptomatic and symptomatic children diagnosed with SARS-CoV-2 infection in pediatric hospital testing programs. *J Clin Microbiol* (2020) **59**(1). doi:10.1128/JCM.02593-20

23. Fajnzylber J, Regan J, Coxen K, Corry H, Wong C, Rosenthal A, et al. SARS-CoV-2 viral load is associated with increased disease severity and mortality. *Nat Commun* (2020) **11**(1):5493. doi:10.1038/s41467-020-19057-5

24. Pujadas E, Chaudhry F, McBride R, Richter F, Zhao S, Wajnberg A, et al. SARS-CoV-2 viral load predicts COVID-19 mortality. *The Lancet Respir Med* (2020) **8**(9):e70. doi:10.1016/S2213-2600(20)30354-4

25. Westblade LF, Brar G, Pinheiro LC, Paidoussis D, Rajan M, Martin P, et al. SARS-CoV-2 viral load predicts mortality in patients with and without cancer who are hospitalized with COVID-19. *Cancer Cell* (2020) **38**(5):661–71.e2. doi:10.1016/j.ccell.2020.09.007

26. Faico-Filho KS, Passarelli VC, Bellei N. Is higher viral load in SARS-CoV-2 associated with death? *The Am J Trop Med Hyg* (2020) **103**(5):2019–21. doi:10.4269/ajtmh.20-0954

27. Bryan A, Fink SL, Gattuso MA, Pepper G, Chaudhary A, Wener MH, et al. SARS-CoV-2 viral load on admission is associated with 30-day mortality. *Open Forum Infect Dis* (2020) **7**(12):ofaa535. doi:10.1093/ofid/ofaa535

28. Walsh KA, Jordan K, Clyne B, Rohde D, Drummond L, Byrne P, et al. SARS-CoV-2 detection, viral load and infectivity over the course of an infection. *J Infect* (2020) **81**(3):357–71. doi:10.1016/j.jinf.2020.06.067

29. Le TQM, Takemura T, Moi ML, Nabeshima T, Nguyen LKH, Hoang VMP, et al. Severe acute respiratory syndrome coronavirus 2 shedding by travelers, vietnam, 2020. *Emerging Infect Dis* (2020) **26**(7):1624–6. doi:10.3201/eid2607.200591

30. Wan R, Mao Z-Q, He L-Y, Hu Y-C, Wei C. Evidence from two cases of asymptomatic infection with SARS-CoV-2: are 14 days of isolation sufficient? *Int J Infect Dis* (2020) **95**:174–5. doi:10.1016/j.ijid.2020.03.041

31. Lavezzo E, Franchin E, Ciavarella C, Cuomo-Dannenburg G, Barzon L, Del Vecchio C, et al. Suppression of a SARS-CoV-2 outbreak in the Italian municipality of Vo. *Nature* (2020) **584**(7821):425–9. doi:10.1038/s41586-020-2488-1

32. Corman VM, Rabenau HF, Adams O, Oberle D, Funk MB, Keller-Stanislawski B, et al. SARS-CoV -2 asymptomatic and symptomatic patients and risk for transfusion transmission. *Transfusion* (2020) **60**(6):1119–22. doi:10.1111/trf.15841

33. He X, Lau EHY, Wu P, Deng X, Wang J, Hao X, et al. Temporal dynamics in viral shedding and transmissibility of COVID-19. *Nat Med* (2020) **26**(5):672–5. doi:10.1038/s41591-020-0869-5

34. Jones TC, Biele G, Muhlemann B, Veith T, Schneider J, Beheim-Schwarzbach J, et al. Estimating infectiousness throughout SARS-CoV-2 infection course. *Science* (2021) **373**(6551):eabi5273. doi:10.1126/science.abi5273

35. Yehia BR, Winegar A, Fogel R, Fakih M, Ottenbacher A, Jesser C, et al. Association of race with mortality among patients hospitalized with coronavirus disease 2019 (COVID-19) at 92 US hospitals. *JAMA Netw Open* (2020) **3**(8): e2018039. doi:10.1001/jamanetworkopen.2020.18039

36. Argyropoulos KV, Serrano A, Hu J, Black M, Feng X, Shen G, et al. Association of initial viral load in severe acute respiratory syndrome coronavirus 2 (SARS-CoV-2) patients with outcome and symptoms. *The Am J Pathol* (2020) **190**(9):1881–7. doi:10.1016/j.ajpath.2020.07.001

37. Rodrigues TS, De Sá KSG, Ishimoto AY, Becerra A, Oliveira S, Almeida L, et al. Inflammasomes are activated in response to SARS-CoV-2 infection and are associated with COVID-19 severity in patients. *The J Exp Med* (2021) **218**(3): e20201707. doi:10.1084/jem.20201707

38. Pairo-Castineira E, Clohisey S, Klaric L, Bretherick AD, Rawlik K, Pasko D, et al. Genetic mechanisms of critical illness in COVID-19. *Nature* (2021) **591**(7848): 92–8. doi:10.1038/s41586-020-03065-y

39. Zhang Q, Bastard P, Liu Z, Le Pen J, Moncada-Velez M, Chen J, et al. Inborn errors of type I IFN immunity in patients with life-threatening COVID-19. *Science* (2020) **370**(6515):eabd4570. doi:10.1126/science.abd4570

40. Bastard P, Rosen LB, Zhang Q, Michailidis E, Hoffmann H-H, Zhang Y, et al. Autoantibodies against type I IFNs in patients with life-threatening COVID-19. *Science.* (2020) **370**(6515):eabd4585. doi:10.1126/science.abd4585

41. Ragab D, Salah Eldin H, Taeimah M, Khattab R, Salem R. The COVID-19 cytokine storm; what we know so far. *Front Immunol* (2020) **11**:1446. doi:10.3389/fimmu.2020.01446

42. Mehta P, McAuley DF, Brown M, Sanchez E, Tattersall RS, Manson JJ. COVID-19: consider cytokine storm syndromes and immunosuppression. *The Lancet* (2020) **395**(10229):1033–4. doi:10.1016/S0140-6736(20)30628-0

43. Huang C, Wang Y, Li X, Ren L, Zhao J, Hu Y, et al. Clinical features of patients infected with 2019 novel coronavirus in Wuhan, China. *The Lancet* (2020) **395**(10223):497–506. doi:10.1016/S0140-6736(20)30183-5

44. Zhao Y, Qin L, Zhang P, Li K, Liang L, Sun J, et al. Longitudinal COVID-19 profiling associates IL-1RA and IL-10 with disease severity and RANTES with mild disease. *JCI Insight* (2020) **5**(13):e139834. doi:10.1172/jci.insight.139834

45. Chen G, Wu D, Guo W, Cao Y, Huang D, Wang H, et al. Clinical and immunological features of severe and moderate coronavirus disease 2019. *J Clin Invest* (2020) **130**(5):2620–9. doi:10.1172/JCI137244

46. Yang L, Gou J, Gao J, Huang L, Zhu Z, Lan C, et al. Immune characteristics predict outcome of severe and critical COVID-19 patients. *Signal Transduct Target Ther* (2020). doi:10.1038/s41392-020-00296-3

47. Liu J, Li S, Liu J, Liang B, Wang X, Wang H, et al. Longitudinal characteristics of lymphocyte responses and cytokine profiles in the peripheral blood of SARS-CoV-2 infected patients. *EBioMedicine* (2020) **55**:102763. doi:10.1016/j.ebiom.2020.102763

48. Batéjat C, Grassin Q, Manuguerra JC, Leclercq I. Heat inactivation of the severe acute respiratory syndrome coronavirus 2. *J biosafety Biosecur* (2021) **3**(1): 1–3. doi:10.1016/j.jobb.2020.12.001

49. CaPPE C. Methods of dealing with values below the limit of detection using SAS. *South SAS User Gr* (2003).

50. Vu LD, Wallace S, Phan AT, Christofferson RC, Turner E, Parker S, et al. Absence of antibody responses to SARS-CoV-2 N protein in COVID-19 vaccine breakthrough cases. *Exp Biol Med (Maywood)* (2022) **247**(21):1923–36. doi:10.1177/15353702221134097

51. CDC. *Defining adult overweight and obesity*. Atlanta, GA, United States: Centers for Disease Control and Prevention. (2022). Available from: https://www.cdc.gov/obesity/basics/adult-defining.html (Accessed June 3, 2022).

52. Christensen DM, Strange JE, Gislason G, Torp-Pedersen C, Gerds T, Fosbøl E, et al. Charlson comorbidity index score and risk of severe outcome and death in Danish COVID-19 patients. *J Gen Intern Med* (2020) **35**(9):2801–3. doi:10.1007/s11606-020-05991-z

53. Vu LD, Siefker D, Jones TL, You D, Taylor R, DeVincenzo J, et al. Elevated levels of type 2 respiratory innate lymphoid cells in human infants with severe respiratory syncytial virus bronchiolitis. *Am J Respir Crit Care Med* (2019) **200**(11): 1414–23. doi:10.1164/rccm.201812-2366OC

54. Singh V, Dwivedi SN, Deo SVS. Ordinal logistic regression model describing factors associated with extent of nodal involvement in oral cancer patients and its prospective validation. *BMC Med Res Methodol* (2020) **20**:95. doi:10.1186/s12874-020-00985-1

55. Huang J, Gao J, Zhu W, Feng R, Liu Q, Chen X, et al. Indicators and prediction models for the severity of Covid-19. *Int J Clin Pract* (2021) **75**(10):e14571. doi:10.1111/ijcp.14571

56. Alrajhi AA, Alswailem OA, Wali G, Alnafee K, AlGhamdi S, Alarifi J, et al. Data-driven prediction for COVID-19 severity in hospitalized patients. *Int J Environ Res Public Health* (2022) **19**(5):2958. doi:10.3390/ijerph19052958

57. Wynants L, Van Calster B, Collins GS, Riley RD, Heinze G, Schuit E, et al. Prediction models for diagnosis and prognosis of covid-19: systematic review and critical appraisal. *BMJ* (2020) **369**:m1328. doi:10.1136/bmj.m1328

58. Krysko O, Kondakova E, Vershinina O, Galova E, Blagonravova A, Gorshkova E, et al. Artificial intelligence predicts severity of COVID-19 based on correlation of exaggerated monocyte activation, excessive organ damage and hyperinflammatory syndrome: a prospective clinical study. *Front Immunol* (2021) **12**:715072. doi:10.3389/fimmu.2021.715072

59. Bennett TD, Moffitt RA, Hajagos JG, Amor B, Anand A, Bissell MM, et al. Clinical characterization and prediction of clinical severity of SARS-CoV-2 infection among US adults using data from the US national COVID cohort collaborative. *JAMA Netw Open* (2021) **4**(7):e2116901. doi:10.1001/jamanetworkopen.2021.16901

60. Gschwandtner M, Derler R, Midwood KS. More than just attractive: how CCL2 influences myeloid cell behavior beyond chemotaxis. *Front Immunol* (2019) **10**:2759. doi:10.3389/fimmu.2019.02759

61. Yang Y, Shen C, Li J, Yuan J, Wei J, Huang F, et al. Plasma IP-10 and MCP-3 levels are highly associated with disease severity and predict the progression of COVID-19. *J Allergy Clin Immunol* (2020) **146**(1):119–27.e4. doi:10.1016/j.jaci.2020.04.027

62. Chen Y, Wang J, Liu C, Su L, Zhang D, Fan J, et al. IP-10 and MCP-1 as biomarkers associated with disease severity of COVID-19. *Mol Med* (2020) **26**(1): 97. doi:10.1186/s10020-020-00230-x

63. Xi X, Guo Y, Zhu M, Wei Y, Li G, Du B, et al. Higher expression of monocyte chemotactic protein 1 in mild COVID-19 patients might be correlated with inhibition of Type I IFN signaling. *Virol J* (2021) **18**(1):12. doi:10.1186/s12985-020-01478-9

64. Xia H, Cao Z, Xie X, Zhang X, Chen JY-C, Wang H, et al. Evasion of type I interferon by SARS-CoV-2. *Cell Rep* (2020) **33**:108234. doi:10.1016/j.celrep.2020.108234

65. Li A, Zhao K, Zhang B, Hua R, Fang Y, Jiang W, et al. SARS-CoV-2 NSP12 protein is not an interferon-β antagonist. *J Virol* (2021) **95**:e0074721. doi:10.1128/JVI.00747-21

66. Wang W, Zhou Z, Xiao X, Tian Z, Dong X, Wang C, et al. SARS-CoV-2 Nsp12 attenuates type I interferon production by inhibiting IRF3 nuclear translocation. *Cell Mol. Immunol.* (2021) **18**:945–53. doi:10.1038/s41423-020-00619-y

67. Fajnzylber J, Regan J, Coxen K, Corry H, Wong C, Rosenthal A, et al. SARS-CoV-2 viral load is associated with increased disease severity and mortality. *Nat Commun* (2020) **11**:5493. doi:10.1038/s41467-020-19057-5

68. Jacobs JL, Bain W, Naqvi A, Staines B, Castanha PMS, Yang H, et al. Severe acute respiratory syndrome coronavirus 2 viremia is associated with coronavirus disease 2019 severity and predicts clinical outcomes. *Clin Infect Dis* (2022) **74**(9): 1525–33. doi:10.1093/cid/ciab686

Scope

Experimental Biology and Medicine (EBM) is a global, peer-reviewed journal dedicated to the publication of multidisciplinary and interdisciplinary research in the biomedical sciences. The journal covers the spectrum of translational research from T0, basic research, to T4, population health. Articles in EBM represent cutting edge research at the overlapping junctions of the biological, physical and engineering sciences that impact upon the health and welfare of the world's population. EBM is particularly appropriate for publication of papers that are multidisciplinary in nature, are of potential interest to a wide audience, and represent experimental medicine in the broadest sense of the term. However, manuscripts reporting novel findings on any topic in the realm of experimental biology and medicine are most welcome.

EBM publishes Research, Reviews, Mini Reviews, and Brief Communications in the following categories.

- Anatomy/Pathology
- Artificial Intelligence/ Machine Learning Applications to Biomedical Research
- Biochemistry and Molecular Biology
- Bioimaging
- Biomedical Engineering
- Bionanoscience
- Cell and Developmental Biology
- Clinical Trials
- Endocrinology and Nutrition
- Environmental Health/Biomarkers/ Precision Medicine
- Genomics, Proteomics, and Bioinformatics
- Immunology/Microbiology/Virology
- Mechanisms of Aging
- Neuroscience
- Pharmacology and Toxicology
- Physiology and Pathophysiology
- Population Health
- Stem Cell Biology
- Structural Biology
- Synthetic Biology
- Systems Biology and Microphysiological Systems
- Translational Research

Submit your work to Experimental Biology and Medicine at
ebm-journal.org/submission

More information
ebm-journal.org/journals/experimental-biology-and-medicine

EBM Experimental Biology and Medicine

EBM is the official journal of the Society for Experimental Biology and Medicine

Led by Dr Steven Goodman, Experimental Biology and Medicine (EBM) is a global, peer-reviewed journal dedicated to the publication of multidisciplinary and interdisciplinary research in the biomedical sciences.

Discover more of our Special Issues

See more →

EBM Experimental Biology and Medicine

The official journal of the Society for Experimental Biology and Medicine

CHIEF EDITOR

Dr. Steven R Goodman

University of Tennessee Health Science Center, Memphis, TN, USA

frontiers | Publishing Partnerships

Contact

development@ebm-journal.org

See more

ebm-journal.org
publishingpartnerships.frontiersin.org/our-partners

frontiers | Publishing Partnerships